

Structure and Magnetic Correlations in Nanoengineered Systems

Diplomarbeit

eingereicht im Fachbereich Physik
der Universität Duisburg–Essen
(Campus Duisburg)

vorgelegt von

Katharina J. Ollefs

aus

Moers

November 2008

Abstract

Synchrotron radiation was utilized to study both magnetic and structural properties of two different nanoengineered systems with elementspecificity.

One of the materials is Co doped ZnO, a dilute magnetic semiconductor, which has been thought to be a promising material to combine ferromagnetic order at room temperature with semiconducting properties for spintronic applications. The issue, if longrange magnetic order in such materials is indeed established by single ion Co doping or by formation of small phase separated Co clusters, was investigated by x-ray linear dichroism (XLD) measurements. A detailed analysis shows that it is possible to obtain materials with excellent structural quality, that is with the Co dopant on substitutional Zn lattice sites and a ZnO matrix broadly undisturbed by the dopant. The onset of clustering depends on the preparation method and the growth parameters. The magnetic properties were studied with x-ray magnetic circular dichroism (XMCD) in combination with SQUID magnetometry. Purely paramagnetic behavior is found for Co:ZnO with high structural perfection. A BRILLOUIN-like paramagnetism was observed for isolated Co with a magnetic moment of $4.1 \mu_B$. A statistical model for the dopant distribution aided to explain the reduction of the total magnetization by $\sim 30\%$ with an anti-ferromagnetic coupling of Co-O-Co pairs, which are a natural consequence of the stochastical dopant distribution. Hence, no intrinsic ferromagnetic interactions could be observed for isolated or paired Co atoms in Co:ZnO. For Co:ZnO films fabricated with different growth parameters, the onset of clustering could be observed by both a decrease of the XLD signal and a change of the spectral shape of the pre-edge region in the x-ray absorption near edge structure (XANES). The evolution of clustering is accompanied by a "magnetic blocking" behavior which is characteristic for a superparamagnetic ensemble.

X-ray photoemission electron microscopy (XPEEM) and FOURIER transform holography (FTH) were adopted to image 18 nm Fe/FeO_x core/shell nanocubes. With XPEEM both the first energy- and field-dependent measurements of individual nanocubes could be performed allowing the investigation of the electronic and magnetic properties. The properties of individual particles are strongly dependent on both their size and shape and also their relative orientation with respect to each other or an applied magnetic field. Therefore the influence of

different anisotropies due to various configurations of interacting particles can be studied allowing an analysis beyond averaged integral magnetometry.

Kurzfassung

Synchrotronstrahlung wurde verwendet, um sowohl die magnetischen als auch strukturellen Eigenschaften von zwei modernen magnetischen Systemen elementarspezifisch zu untersuchen.

Eines dieser Materialien ist Co dotiertes ZnO, das als vielversprechendes Material zur Kombination von halbleitenden Eigenschaften mit ferromagnetischer Ordnung für Spintronikanwendungen galt. Die Fragestellung, ob die langreichweitige magnetische Ordnung durch das Dotieren des ZnO mit einzelnen Co Ionen oder durch das Bilden von phasenseparierten Clustern hervorgerufen wird, wurde mit Hilfe von Messungen des Röntgenlineardichroismus (XLD) untersucht. Eine detaillierte Analyse zeigt, dass es möglich ist, in Abhängigkeit von den Präparationsmethoden und -bedingungen, sehr gute strukturelle Ordnung zu erhalten, wobei die Co Dotieratome Zn Gitterplätze in einem weitgehend ungestörten ZnO Kristall besetzen. Die magnetischen Eigenschaften wurden mit Hilfe von Röntgenzirkulardichroismus (XMCD) und SQUID Magnetometrie untersucht. Ein rein paramagnetisches Verhalten wurde für Co:ZnO mit hoher struktureller Güte gefunden, wobei isolierte Co Dotieratome BRILLOUIN-artigen Paramagnetismus mit einem magnetischen Moment von ca. $4\mu_B$ aufweisen. Eine Reduktion der Gesamtmagnetisierung um $\sim 30\%$ wurde mit Hilfe eines statistischen Modells auf die antiferromagnetische Kopplung von Co-O-Co Paaren, die eine natürliche Folge der stochastischen Verteilung der Dotieratome sind, zurückgeführt. Es konnten folglich keine intrinsischen ferromagnetischen Wechselwirkungen für isolierte oder gepaarte Co Atome in ZnO beobachtet werden. Bei Co:ZnO, das mit anderen Wachstumsparametern hergestellt wurde, konnte die Entstehung von Clustern anhand eines reduzierten XLD Signals und einer Veränderung des Vorkantenbereichs in der Nahkantenfeinstruktur der Röntgenabsorption beobachtet werden. Das Auftreten von Clustern war dabei begleitet von einem magnetischen Blocking-Verhalten, das typisch für ein superparamagnetisches Ensemble ist.

Röntgen Photoemissionselektronmikroskopie (XPEEM) und FOURIER Transformationsholographie (FTH) wurden angewendet um 18 nm große Fe/FeO_x Kern/Hülle Nanowürfel abzubilden. Mit XPEEM war es möglich sowohl die elektronischen als auch die magnetischen Eigenschaften von einzelnen Partikeln zu untersuchen. Die Eigenschaften einzelner Partikel können individuell sehr unterschiedlich sein, da die Eigenschaften sowohl von der individuellen Form und

Größe der Partikel abhängen, als auch von der relativen Orientierung der Partikel zueinander und zu der Richtung eines angelegten magnetischen Feldes. Der Einfluss unterschiedlicher Anisotropien aufgrund von verschiedenen Konfigurationen von wechselwirkenden Partikeln kann somit, im Gegensatz zu konventioneller integraler Magnetometrie, weitergehend untersucht werden.

Contents

Abstract	iii
Kurzfassung	v
Introduction	ix
1 Theoretical Background	1
1.1 Remarks on Magnetism	1
1.1.1 Magnetism in Solids	1
1.1.2 Magnetism in Small Particles and Clusters	6
1.2 X-rays and Matter	8
1.2.1 X-ray Absorption Spectroscopy	8
1.2.2 Imaging	12
2 Experimental Methods	19
2.1 Spectroscopy using Synchrotron Radiation	21
2.1.1 Beamline ID-12 (ESRF)	21
2.1.2 X-ray Magnetic Circular Dichroism Setup	22
2.1.3 X-ray Linear Dichroism Setup	22
2.2 Imaging using Synchrotron Radiation	23
2.2.1 Beamline 13-3 (SSRL)	23
2.2.2 Beamline UE49-PGM-1-SPEEM (BESSY)	24
2.3 Superconducting Quantum Interference Device	26
3 Sample preparation	29
3.1 Cobalt doped Zinc Oxide	29
3.2 Iron/Iron Oxide Nanocubes	32
4 Spectroscopy on Cobalt doped Zinc Oxide	38
4.1 X-ray Linear Dichroism	39
4.1.1 Simulation with FDMNES code	41
4.1.2 Experimental Evidence for Clustering	58
4.2 Magnetic Properties of Cobalt doped Zinc Oxide	60

5	Imaging of Nanocubes	69
5.1	Magnetic Imaging of Nanocubes with XPEEM	70
5.1.1	Single Nanoparticle Spectroscopy	71
5.1.2	Magnetometry: Integral versus Single Particle	73
5.2	Imaging of Nanocubes with X-ray Speckles	78
6	Conclusion and outlook	83
A	X-Ray Data	86
A.1	Absorption Edges	86
A.2	Synchrotron Ring Parameters	87
B	Quarter Wave Plate	88
C	FDMNES-code	90
C.1	Input file	90
C.2	Convolution	92
D	Additional Data	94
	Bibliography	101
	Curriculum vitae	102
	List of Publications	103
	Acknowledgements / Dank	104

Introduction

Since their discovery in 1895 by Conrad RÖNTGEN x-rays have revolutionized the way we look at matter. As the wavelength of x-rays is of the same order of magnitude as interatomic distances in solids, diffraction limits do not pose severe constraints on the achievable spatial resolution. Not only the knowledge about interactions of x-rays with matter but also the technical possibilities have experienced an intense development.

The x-ray sources which are nowadays available differ heavily from the first x-ray tubes. Modern large-scale synchrotron facilities provide radiation of high brilliance (with a typical brightness of 10^{20} photons/(sec)(mm)²(mrad)² [1]) with tunable photon energy as well as full control over the polarization of the light. A new fourth generation of x-ray sources even promises fully coherent radiation with an unprecedented brilliance, which is about ten orders of magnitude higher than currently available. The combination of these technical developments with new experimental approaches has lead to new insight in physical phenomena related to matter and therefore has made x-rays a powerful research tool for the study, e.g. of modern magnetic materials.

Today research in magnetism is motivated by the wish to achieve a microscopic understanding of magnetic phenomena and magnetic materials but also influenced by the goal to utilize the acquired knowledge for technological advances.

Dilute magnetic semiconductors (DMS) are such modern materials, which are envisioned to combine properties known from semiconductors with magnetic order, e.g. for spintronic applications, where the spin is utilized in addition to the charge to carry information, e.g. in the spin transistor ¹ proposed by DATTA and DAS [2]. However for technological applications magnetic order up to room temperature is a necessity. A promising candidate for such a DMS material is cobalt doped zincoxide (Co:ZnO), however up to now ferromagnetism [3] and absence of the same [4] have been reported. In order to distinguish between intrinsic properties of Co:ZnO and effects caused by phase separation and Co clusters, a careful structural analysis is mandatory.

¹Note, that this device does not provide gain so that the term "transistor" is somewhat misleading; in the original work the device was termed "Electronic analogue of the electro-optical modulator".

One aim of this work was to study Co:ZnO of excellent structural quality to gain an insight into the intrinsic properties of the system. Besides standard characterization with x-ray diffraction (XRD) synchrotron radiation was utilized to probe the local structure using x-ray linear dichroism (XLD) measured with elementspecificity at the Zn and Co K-edge. In order to yield deeper insight the corresponding spectra were simulated for comparison. For magnetic characterization conventional SQUID magnetometry and x-ray magnetic circular dichroism (XMCD) were combined. A further step of investigation was to observe the onset of Co clustering in the Co:ZnO films and study the changes in the magnetic properties.

Another interesting modern magnetic material are magnetic nanoparticles. The list of possible applications ranges from hypothermia to cure cancer [5] to data storage applications [6, 7]. However due to the small size of the particles their properties are very different from the bulk leading to effects like, e.g. superparamagnetism. Vast efforts have been undertaken to study both structural and magnetic properties of nanoparticles. Currently available techniques for magnetic characterization like ferromagnetic resonance (FMR), SQUID and XMCD all yield averaged results for an entire ensemble and therefore do not allow to measure the individual properties of the nanoparticles. However up to now magnetic single nanoparticle measurements remain a big challenge.

In this thesis individual Fe/FeO_x nanocubes were studied using x-ray spectro-microscopy. X-ray photoemission electron microscopy (XPEEM) allows to measure the x-ray absorption of a single nanocube both energy and field dependent. However, since many images have to be acquired in order to yield enough signal for XPEEM studies the measurements are quasi statical. Therefore a second approach i.e. FOURIER transform holography is pursued in order to be able to extend the magnetic characterization to be time-dependent in the future.

This thesis is structured as follows:

- Chapter 1 introduces the main aspects of theory of x-rays and magnetism relevant for this thesis.
- Chapter 2 describes the experimental setup at the different beamlines and the SQUID magnetometer.
- Chapter 3 comments on the preparation and standard characterization of the Co:ZnO and the Fe/FeO_x nanocube samples.
- Chapter 4 discusses the results of the elementspecific structural and magnetic characterization of Co:ZnO.
- Chapter 5 gives the first results obtained by x-ray spectro-microscopy of the Fe/FeO_x nanocubes.
- Chapter 6 summarizes the results of this thesis and gives an outlook on possible future experiments.

Chapter 1

Theoretical Background

1.1 Remarks on Magnetism

1.1.1 Magnetism in Solids

A fundamental observable in magnetism is the magnetic moment μ . For a free atom μ consists of three principal contributions: the spin S of the electrons, the orbital motion of the electrons about the nucleus (orbital moment), and the change of orbital moment induced by an external magnetic field [8]. The last of these contributions is universal for all materials and gives rise to a phenomenon called *diamagnetism*, which results in a magnetic moment induced antiparallel to an applied external magnetic field and is temperature independent. Diamagnetism is adherent to the tendency of electrical charges to shield an external magnetic field known in classical electromagnetism from the LENZ's law stating that, when flux through an electric circuit is changed the induced current opposes the flux change.

For atoms with completely filled shells this is the only magnetic contribution. However, some materials have intrinsic magnetic moments for example ascribed to unpaired electrons, which are aligned parallel to the applied magnetic field giving rise to the so-called *paramagnetic* behavior. Usually there are three types of paramagnetism distinguished. The temperature independent Pauli paramagnetism is caused by the conduction electrons in metals. Another temperature independent contribution is the van Vleck paramagnetism, which occurs if a non-magnetic ground state and a paramagnetic excited state are mixed. This paramagnetic behavior is not restricted to metals, but its strength is inversely proportional to the band gap [9]. A temperature dependent paramagnetic contribution is the Langevin paramagnetism resulting from intrinsic magnetic moments, which are ideally ordered at $T=0$ K.

Materials, in which intrinsic magnetic moments are not randomly oriented without external magnetic field, but exhibit a long range order at finite temperatures are called *ferromagnetic* if the magnetic moments are aligned parallel,

antiferromagnetic if the magnetic moments are aligned antiparallel and compensate themselves, or *ferrimagnetic* if they only partially compensate each other.

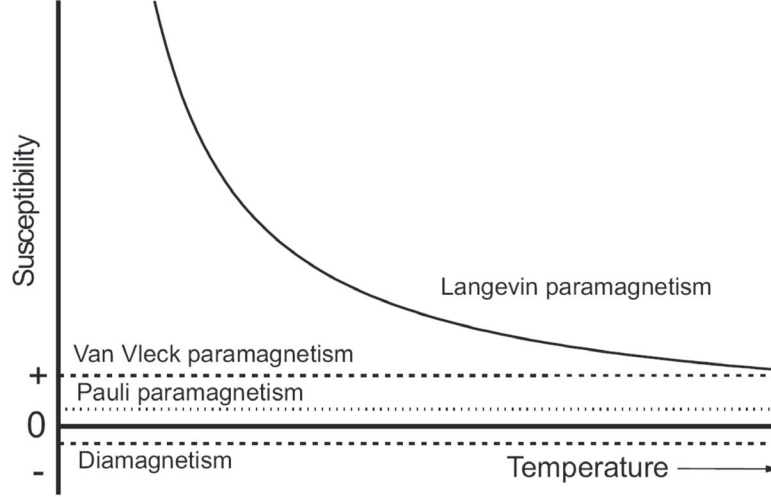


Figure 1.1: Magnetic susceptibility as a function of temperature (adapted from [8]).

The magnetic response of a material to an applied external magnetic field \vec{H} is described by the magnetic susceptibility tensor χ :

$$\vec{M} \cdot \chi = \vec{H} \quad (1.1)$$

with the magnetization \vec{M} being the average magnetic moment $\vec{\mu}$ per volume V of the system.

For a free atom or an ion in free space the magnetic moment $\vec{\mu}$ is given by:

$$\vec{\mu} = -g_J \cdot \mu_B \cdot \vec{J} \quad (1.2)$$

where \vec{J} is the total angular momentum, $\mu_B = \frac{e\hbar}{2m}$ the BOHR magneton and g_J the LANDÉ factor given by:

$$g_J = 1 + \frac{J(J+1) + S(S+1) - L(L+1)}{2J(J+1)} \quad (1.3)$$

with the spin angular momentum quantum number S and the orbital angular momentum quantum number L . In order for this formula to apply the atom needs to be in the RUSSELL-SAUNDERS ground state and hence S and L have to couple according to $J = L + S$. Once the system has a quantization axis along z , e.g. by applying a magnetic field along z direction equation 1.2 changes to:

$$\langle \mu_z \rangle = -g_J \cdot \mu_B \cdot \langle J_z \rangle \quad (1.4)$$

In a magnetic field N atoms with angular momentum quantum number J has $2J+1$ equally spaced energy levels. Using BOLTZMANN statistics one obtains for the temperature dependence of the magnetization:

$$\langle M_z \rangle = N \cdot g_J \cdot \langle J_z \rangle \cdot \mu_B \cdot B_J(x) \quad (1.5)$$

with $x = \frac{g_J \mu_B B}{k_B T}$ and where B_J is the BRILLOUIN function defined as:

$$B_J(x) = \frac{2J+1}{2J} \coth\left(\frac{(2J+1)x}{2J}\right) - \frac{1}{2J} \coth\left(\frac{x}{2J}\right) \quad (1.6)$$

For a macrospin composed of classical magnetic moments (limit $J \rightarrow \infty$) with no direction quantization one gets the LANGEVIN function:

$$B_\infty = L(x) = \coth(x) - \frac{1}{x} \quad (1.7)$$

With $|x| \ll 1$ one can approximate the BRILLOUIN function and obtain the CURIE law for the temperature dependence of the susceptibility of a paramagnet:

$$\chi(T) = \frac{C}{T} \quad (1.8)$$

where C is the CURIE constant, which is given by:

$$C = \frac{N \cdot \mu_B^2 \cdot p^2}{3 \cdot k_B} \quad (1.9)$$

with the number of atoms N , the BOLTZMANN constant k_B and the effective magneton number p :

$$p = g_J \sqrt{J(J+1)} \quad (1.10)$$

The spontaneous alignment of the permanent magnetic moments without external magnetic field below a certain temperature in ferromagnets is a quantum mechanical effect. It can be explained by the exchange interaction H_{ex} resulting from the combination of COULOMB interaction and the PAULI principle. In the HEISENBERG model the exchange interaction H_{ex} between two atoms i, j bearing the electron spins S_i and S_j is given by:

$$H_{ex} = -2J \vec{S}_i \cdot \vec{S}_j \quad (1.11)$$

where J is the exchange integral with $J < 0$ for ferromagnetic order and $J > 0$ for antiferromagnetic order.

This interaction can be phenomenologically described with help of a strong internal magnetic field called the WEISS field (also know as exchange field or molecular field). The temperature, where the magnetic order is overcome by thermal

fluctuations is called CURIE temperature T_C and at that temperature the ferromagnet becomes paramagnetic. For a ferromagnet the temperature dependence of the susceptibility χ above this temperature is given by the CURIE-WEISS law:

$$\chi(T > T_C) = \frac{C}{T - T_C} \quad (1.12)$$

For an antiferromagnet the critical temperature is called NÉEL temperature T_N and the temperature dependence is described (for $T > T_N$) by:

$$\chi(T) = \frac{C}{T + \Theta} \quad (1.13)$$

with a negative temperature Θ as can be seen in figure 1.2.

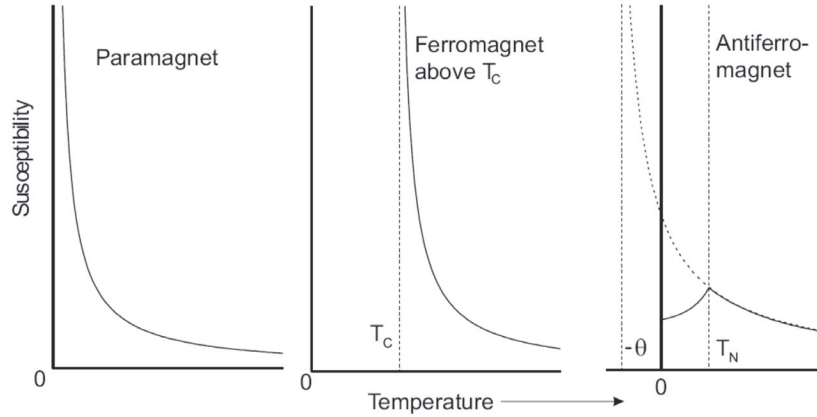


Figure 1.2: Temperature dependence of the magnetic susceptibility of a paramagnet, ferromagnet and antiferromagnet (adapted from [8]).

In this description localized moments are assumed. This assumption might be reasonable for isolators, however for the ferromagnetic $3d$ transition metals like iron (Fe), cobalt (Co) or nickel (Ni) the magnetism is mainly due to spins of the $3d$ electrons, which contribute to the conductivity and hence have a more delocalized nature (also called itinerant magnetic moments).

Electric conductivity and exchange interaction are often explained in the STONER model. It is assumed that the density of states (DOS) for both spin directions are equal, but shifted due to exchange interaction by a certain energy value, the exchange splitting Δ between spin-up and spin-down. The criterion for the occurrence of ferromagnetism, the so-called STONER criterion states, that a large density of states in the vicinity of the FERMI energy E_F and a strong exchange interaction are necessary:

$$I \cdot \tilde{D}(E_F) > 1 \quad (1.14)$$

with the density of states per atom and per spin direction \tilde{D} and the STONER parameter I characterizing the lowering of energy due to electron correlation. Since (at $T=0K$) in equilibrium the energy bands for both spin directions are filled up to the same energy, the FERMI energy E_F , more electrons occupy the energy band of the spin direction with the lower energy, which is therefore called the majority band. The corresponding higher energy band is called minority band.

Magnetic Anisotropy

Magnetic anisotropy is generally attributed to ferromagnetic materials, however anisotropic magnetic behavior also exists for paramagnetic ions in a non-spherically symmetric crystal field, e.g. for Co doped ZnO [10, 11] and is not to be mistaken with the usual magnetocrystalline anisotropy of ferromagnets.

The magnetization direction in a ferromagnetic solid without external fields is not arbitrary in general, but tends to lie along one or several axes. Along these preferred axes, also called easy axes, the groundstate energy of the system is minimal. The energy necessary to rotate the magnetization from the easy direction into the hard direction, where groundstate energy is largest, is called *magnetic anisotropy energy* (MAE). The isotropic exchange interaction is not relevant since it is only related to the relative spin orientation in the Heisenberg model and not to a crystallographic direction.

One contribution is the *magneto-crystalline anisotropy* (MCA). It is caused by spin-orbit interaction which couples the spin to the orbital motion of the electrons, which again is determined by the electric potential with the periodicity of the crystal lattice. The anisotropy energy is thus given by the anisotropy of the orbital moment $\Delta\mu_l$ and the spin-orbit coupling constant ξ [12, 13] (with a prefactor α depending on the electronic structure [14]).

$$E_{MCA} = \alpha \cdot \frac{\xi}{4\mu_B} \cdot \Delta\mu_l \quad (1.15)$$

The angular dependence of the magneto-crystalline anisotropy is described phenomenologically and can be expanded in $\alpha_i = \vec{e}_i \cdot \vec{M}/M$ ([15] and references therein).

The other contribution to the magnetic anisotropy is the *shape anisotropy*, which is caused by the demagnetizing field arising from dipolar interactions in a solid. The energy of two magnetic moments $\vec{\mu}_i$ and $\vec{\mu}_j$ due to their dipolar interaction is given by:

$$E_{dip} = \frac{\mu_0}{4\pi} \left[\frac{\vec{\mu}_i \cdot \vec{\mu}_j}{|\vec{r}_{ij}|^3} - \frac{3(\vec{r}_{ij} \cdot \vec{\mu}_i)(\vec{r}_{ij} \cdot \vec{\mu}_j)}{|\vec{r}_{ij}|^5} \right] \quad (1.16)$$

Magnetic poles emerge at the surface of a finite body due to uncompensated magnetic components resulting in a stray field outside and a demagnetizing field

inside. The energy of a homogeneously magnetized sample in its own strayfield H_{str} is given by:

$$E_{str} = -\frac{1}{2}\mu_0 \int \vec{M} \cdot \vec{H}_{str} dV \quad \text{with} \quad \vec{H}_{str} = -N \cdot \vec{M} \quad (1.17)$$

where N is the demagnetizing tensor.

This stray field is generally not isotropic for nonspherical samples and for example for a 2-dimensional thin film (with infinite x and y extension) this leads to $N_x = N_y = 0$ and $N_z = 1$ and hence to a contribution to the anisotropy density:

$$F_{str} = \frac{E_{str}}{V} = -\frac{1}{2}\mu_0 M^2 \alpha_z^3 \quad (1.18)$$

1.1.2 Magnetism in Small Particles and Clusters: Superparamagnetism

Magnetic Anisotropy

For spherical samples as well as for spherical nanoparticles the shape anisotropy vanishes ($N_x=N_y=N_z=1/3$) due to the rotational invariance of N , though in the case of non negligible dipole-dipole interactions among the nanoparticles a shape anisotropy of the whole ensemble arises. For a 2-dimensional distribution of particles this leads to an expression for the anisotropy density similar to the one for the thin film (1.18):

$$F_{str} = -\frac{1}{2}f\mu_0 M^2 \alpha_z^3 \quad (1.19)$$

where f is a filling factor taking into account the difference between individual, separated nanoparticles and a closed layer [16].

For small particles the fraction of atoms at the surface is large, leading to an additional contribution to the magnetic anisotropy, the (magnetocrystalline) *surface anisotropy* caused by a breaking of the local symmetry [12]. For atoms at the surface the coordination numbers and directions are different for the next neighbors resulting in different step and surface anisotropies for the different facets [17].

All different contributions to the magnetic anisotropy are often summarized in an *effective anisotropy energy* ΔE accounting also for imperfections of shape or non-negligible interactions of the particles (which is usually assumed to be uniaxial) and described by an *effective anisotropy constant* K_{eff} :

$$\Delta E = V \cdot K_{eff} \quad (1.20)$$

Macrospin and Blocking-Behavior

Below a certain size magnetic solids do not form domain walls and thus behave like one single domain with all magnetic moments μ aligned ([18] and references therein). Hence the collectivity of atomic spins can be treated as one macrospin. For such small particles the magnetization is reversed by rotation of the macrospin according to a theory developed by Stoner and Wohlfarth [19]. If the thermal energy $k_B T$ becomes larger than the energy barrier ΔE caused by the effective anisotropy, the direction of magnetization is not given by the easy axis anymore and the macrospin fluctuates. According to a theory developed by NÉEL and later BROWN [20] the fluctuation time τ can be described with an ARRHENIUS Law:

$$\tau = \tau_0 \cdot \exp\left[\frac{\Delta E}{k_B T}\right] = \tau_0 \cdot \exp\left[\frac{K_{eff} V}{k_B T}\right] \quad (1.21)$$

The attempt time τ_0 is in the order of 10^{-12} to 10^{-9} s [18, 20]. For a measurement with a time constant t larger than τ a sample with ferromagnetic particles behaves paramagnetically even well below the material dependent CURIE temperature. As not the individual spins fluctuate, but the macrospin with a magnetic moment of thousands of μ_B , this behavior is called *superparamagnetism*.

If the time constant t is smaller than τ , fluctuations are not detected by the measurement and hence the particles appear *ferromagnetically blocked*. The temperature, where superparamagnetism appears due to an increase in thermal energy, is called blocking temperature T_B and depends not only on the material, but also on the time constant of the measurement t , e.g. $t_{SQUID} = 10^2$ s [21]. Above the blocking temperature the magnetization of the ensemble of identical particles can be described by the LANGEVIN function (1.7) for paramagnets with $x = \frac{M_s V B}{k_B T}$, where M_s is the saturation magnetization. For small magnetic fields this yields:

$$M = M_s \frac{x}{3} \quad (1.22)$$

Below the blocking temperature the magnetization of the sample is dependent on the magnetic field history, that is whether the sample was cooled with (*field cooled*, FC) or without an applied external field (*zero-field cooled*, ZFC). For these two cases the magnetization is given by:

$$M_{FC}^{bl} = \frac{M_s^2 V}{3k_B T_B} B \text{ and } M_{ZFC}^{bl} = \frac{M_s^2}{3K_{eff}} B \quad (1.23)$$

However, in real samples the particles do not all have the same size, but a volume distribution $D(V)$ leading to a distribution in blocking temperatures. The temperature dependence of the magnetization of a real sample of particles is then given by:

$$M = \frac{M_s^2 B}{3k_B T} \frac{1}{N} \int_0^{V_L} V^2 D(V) dV + \frac{M_s^2 B}{3K_{eff}} \frac{1}{N} \int_{V_L}^{\infty} V D(V) dV \quad (1.24)$$

with the volume at the boundary between ferromagnetically blocked and superparamagnetic particles $V_L = \frac{k_B T}{K_{eff}} \ln \frac{\tau}{\tau_0}$ and the normalization constant N with $N = \int_0^\infty V D(V) dV$ [15, 21]. Both saturation magnetization M_S and effective anisotropy K_{eff} are not constant but temperature dependent, which has to be taken into account especially at temperatures close to the CURIE temperature ([22] and references therein).

The distribution of blocking temperatures for real samples leads to a broadening of the blocking peak of the magnetization. Furthermore the temperature with maximum magnetization (in the ZFC) T_{max} is not equal to the blocking temperature T_B but larger than the actual blocking temperature. The larger the volume distribution of the nanoparticle ensemble the larger is the deviation T_{max}/T_B as described in detail in [23].

1.2 X-rays and Matter

1.2.1 X-ray Absorption Spectroscopy (XAS)

X-ray Absorption Spectroscopy (XAS), measuring the absorption of x-rays as a function of photon energy $E = \hbar\omega$, was invented by Maurice de BROGLIE, who published the first observation of an absorption edge as early as 1913 [24]. It is nowadays an active field of research that comprises various types of spectroscopies using different properties of matter that influence the absorption of x-rays. When x-rays are absorbed by matter, core electrons are excited into unoccupied electronic states. Empty core states are then filled by electrons from higher energy states emitting a photon or another Auger-electron.

In the following a standard interpretation of x-ray absorption spectra will be introduced.

The attenuation of electromagnetic radiation propagating through a continuous homogeneous medium is described by LAMBERT-BEER's Law:

$$I(E, z) = I_0 \cdot e^{-\mu(E) \cdot z} \quad (1.25)$$

where I_0 is the incoming intensity, μ the attenuation coefficient and z the thickness of the absorbing material.

While elastic RAYLEIGH and inelastic COMPTON scattering can be neglected for the investigated range of x-ray wavelengths [25] the photoeffect is dominating and thus μ is approximately the photoabsorption coefficient, which is proportional to the photoabsorption cross-section defined as transition probability per unit time T_{if} normalized to the photon flux Φ_0 . The transition probability T_{if} can be described by FERMI's Golden Rule, in the one-electron approximation [26] (as

described in [1] it was originally derived by DIRAC [27] and later called 'Fermi's Golden Rule No:2' [28]).

$$T_{if} \propto \sum_f |\langle f | H_{int} | i \rangle|^2 \cdot \delta(E_f - E_i - \hbar\omega) \quad (1.26)$$

where $|i\rangle$ and $\langle f|$ are the initial and final states with energies E_i and E_f , respectively. $M_{if}^2 = |\langle f | H_{int} | i \rangle|^2$ is the transition matrix element with the interaction Hamiltonian $H_{int} \propto \vec{p} \cdot \vec{A}$ (where \vec{p} is the momentum operator and \vec{A} the vector potential of the incident wavefield). For electric dipole transitions the matrix elements can be approximated as $M_{if}^2 = |\langle f | \vec{p} \cdot \vec{\epsilon} | i \rangle|^2$ with the photon polarization vector $\vec{\epsilon}$. However electric quadrupole transitions might also lead to measurable effects, e.g. for transition metal K edges.

The dipole transition matrix element $M_{if} = |\langle f | \vec{p} \cdot \vec{\epsilon} | i \rangle|$ leads to the well-known *dipole selection rules* for transitions between states of the form $|n, l, m_l, s, m_s\rangle$ (with the x-ray angular momentum $q\hbar$) [1]:

$$\Delta l = \pm 1; \Delta m_l = q = 0, \pm 1; \Delta s = 0; \Delta m_s = 0 \quad (1.27)$$

As the initial core states are very localized they can be described quite well by states of the form $|n, l, m_l, s, m_s\rangle$. However a description of the delocalized final states is not as easy and the dipole selection rules therefore are an approximation yielding only a basic understanding, since the exact evaluation of the transition matrix elements is nontrivial.

As one can see, the absorption, i.e. the number of transitions, is maximum for an x-ray energy that is equal to the energy difference between a high density of occupied initial states and a high density of unoccupied final states. This is the case if the photon energy is large enough to excite a core electron into the continuum above the FERMI level resulting in a sharp rise of the absorption coefficient called "edge". These edges are labeled according to the SOMMERFELD notation as can be seen in figure 1.3. Since the ionization energies are different for every chemical element, the corresponding absorption edge measured at a given energy is elementspecific.

One generally distinguishes between the X-ray Absorption Near Edge Structure (XANES)(also called Near-Edge X-ray Absorption Fine Structure (NEXAFS)) and the Extended X-ray Absorption Fine Structure (EXAFS), which starts about 50 eV above the absorption edge. XANES probes the unoccupied density of states and therefore it depends on the local geometric structure. The spectral shape reflects the electronic and chemical state of the absorbing atom. A property of the electromagnetic radiation itself namely the polarization leads to the effect of dichroism, that is the dependence of photon absorption on polarization. There are four main types of dichroism: X-ray Linear Dichroism (XLD) and X-ray (Natural) Circular Dichroism (XNCD), which depend on the charge distribution; whereas X-ray Magnetic Circular Dichroism (XMCD) and X-ray Magnetic Linear Dichroism (XMLD) depend on charge and spin distribution.

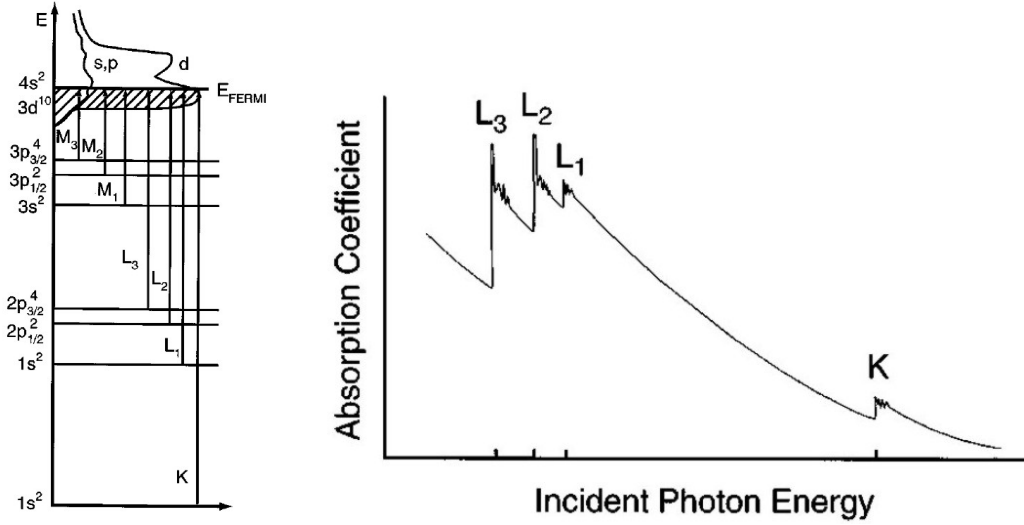


Figure 1.3: Left: Excitations of core electrons corresponding to the K, L and M x-ray absorption edges, with arrows indicating the threshold energy of each edge. Right: Scheme of the x-ray absorption coefficient as a function of incident photon energy with K and L absorption edges (adapted from [29]).

X-ray Magnetic Circular Dichroism (XMCD)

The XMCD is the difference of two XANES spectra for x-rays with a photon spin parallel and antiparallel to the magnetization direction of a sample and the effect was predicted by Erskine and Stern by extending the Magneto-Optical Kerr Effect (MOKE) to the energy range of x-rays [30] and was first experimentally observed by Schütz *et al.* [31].

The concept of the XMCD effect, e.g., at the L_3 and L_2 edges of the 3d transition metals can be explained in a *two step model*:

As a *first step* photoelectrons with a spin and/or orbital momentum are generated from localized inner shells (here the p-shell) due to conservation of angular momentum by circularly polarized x-rays as shown in figure 1.4. For a photoelectron excited from a spin-orbit split level, e.g. for the L_3 -edge, the angular momentum of the photon can be partly transferred to the spin via spin-orbit coupling resulting in a spin polarization of the excited photoelectron, which is opposite for incident x-rays with left ($+\hbar$ helicity) and right ($-\hbar$ helicity) polarization and also opposite at the two edges since the L_3 ($2p_{2/3}$) and L_2 -edge ($2p_{1/2}$) have opposite spin-orbit coupling ($l + s$ and $l - s$). Hence, the core shell can be viewed as an atom specific source of spin-polarized electrons with a quantization axis of the photoelectron spin identical to the quantization axis of the photon spin, i.e., parallel or antiparallel to the x-ray propagation direction.

In a *second step* the exchange split valence shell with unequally distributed spin-up and spin-down states acts as a detector for the spin or orbital momentum of the photoelectron. For optimal detection the quantization axis of the valence shell is aligned with the quantization axis of the photoelectron spin. The separate values of spin and orbital magnetic moment can be derived by applying the so-called XMCD sum rules for the orientation-averaged intensity.

For K-edge the situation is more complicated. The $1s$ core shell has only a spin and zero orbital angular momentum, it has hence no spin-orbit coupling, however it may exhibit a small exchange (or Zeeman) splitting into $m_s = \pm \frac{1}{2}$. As between spin and electric field there is no direct interaction, the photon spin is transferred to the photoelectron as an orbital angular momentum \hbar or $-\hbar$. Thus, it can only be detected if the valence shell has an orbital magnetic moment therewith an imbalance of unoccupied states in the valence band with quantum numbers $+m_l$ and $-m_l$. Without orbital moment of the valence shell the orbital moment of the photoelectrons can not be distinguished and hence no (circular) dichroism effect arises even if the valence shell has a spin polarization (as in the Stoner model) [32], nevertheless an indirect sensitivity to the spin magnetic moment can arise through spin-orbit interaction.

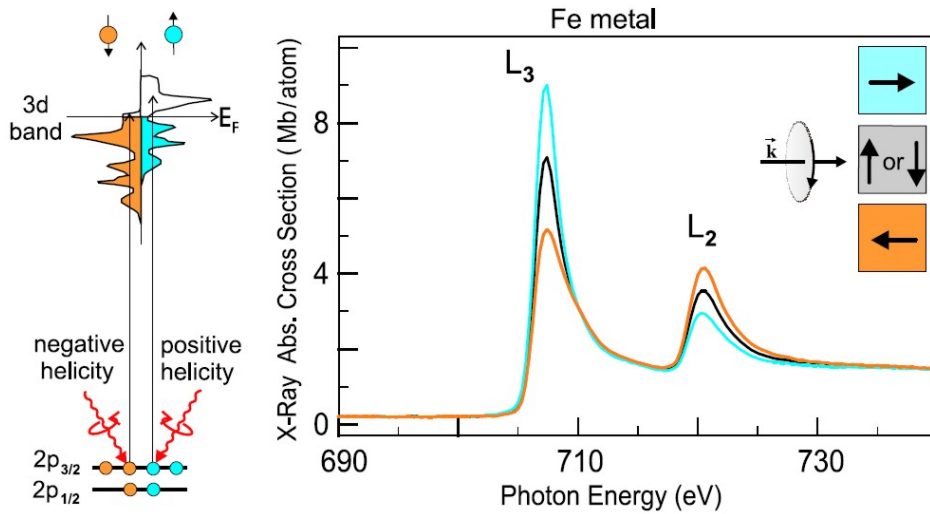


Figure 1.4: XMCD effect illustrated for Fe L-edge:

Left: Density of spin-up and spin-down states (magnetization direction chosen upwards so that the spin-down states are almost filled whereas the spin-up states are only partially filled) and the excitations from the $2p$ to the $3d$ states indicated for positive and negative helicity of the x-rays.

Right: L-edge spectrum of Fe shown for different relative orientations of the magnetization and the photon angular momentum direction (as denoted by the color coding of the spectra and the arrows on the right).

X-ray Linear Dichroism (XLD)

XLD is the difference of two XANES spectra with two orthogonal linear polarization directions. Even though a dichroism using linearly polarized x-rays may be of both magnetic and structural origin only the structural linear dichroism will be discussed in this work, which is often also termed 'natural' as it arises from an anisotropic charge distribution due to bonding only (and can therefore be present in nonmagnetic samples).

At the K-edge the situation is simple because the 1s core level is spherically symmetric and hence the dependence of the absorption coefficient on the orientation of the electric field \vec{E} -vector is only determined by the spatial distribution of empty valence states. This is often called search light effect, because the transition probability T_{if} is proportional to the number of empty valence states in the direction of \vec{E} . Therefore it detects the direction with maximum and minimum number of empty valence states [1]. For a crystal with an anisotropy of final states for different crystallographic axes, e.g. the wurtzite crystal, a typical XLD signature arises.

1.2.2 Imaging

Apart from spectroscopic applications, x-rays can also be used for imaging. The spatial resolution achieved may not exceed the spatial resolution of other techniques e.g. (HR-) Transmission Electron Microscopy (TEM), yet they offer capabilities not provided by other techniques as for example element-specificity. Using the already mentioned dichroism effects leads to x-ray magnetic microscopy and to the frequently used term called spectro-microscopy, because spectroscopic concepts are utilized as contrast mechanism.

Lens-Based Microscopy

Similar to electron microscopy also for x-ray imaging there are two general approaches either based on scanning or on imaging. For *scanning x-ray microscopy*, e.g. Scanning Transmission X-ray Microscopy (STXM) a monochromatic x-ray beam is focused to a smallest possible spot on the sample and the transmitted x-rays are then detected as function of the position of the beam on the sample. Energy resolution is given by the monochromator of the beamline and the spatial resolution is determined by the spot size of the x-ray beam on the sample. To focus x-rays they are either reflected by grazing incidence mirrors or diffracted by multilayer mirrors or zone plates where zone plates yield the smallest spot size in practice [1].

For *imaging x-ray microscopy*, e.g. Transmission Imaging X-ray Microscopy (TIXM) (figure 1.5) the x-ray beam is focussed on the sample by a condenser zone plate in combination with a pinhole with the focal spot size serving as

the field of view for the imaging process. A magnified image of the illuminated area is then generated by a microzone plate on a fluorescent screen or a CCD detecting x-rays. A spatial resolution of 15 nm has been achieved in 2005 (by a zone plate for a TIXM) and even less than 10 nm are expected for the future where the width of outermost zones of the microzone plate pattern is decisive for the spatial resolution [33].

In principle there are three possible detection methods: transmitted photons, fluorescent photons or photoelectrons. In contrast to electron based methods, e.g. X-ray Photoemission Electron Microscopy (XPEEM) (figure 1.5), where it is more challenging, x-ray transmission or fluorescence microscopies are well suited for measurements in the presence of magnetic fields. As the transmission of x-ray intensity is caused by the entire thickness of the sample, it is in that sense 'bulk' sensitive.

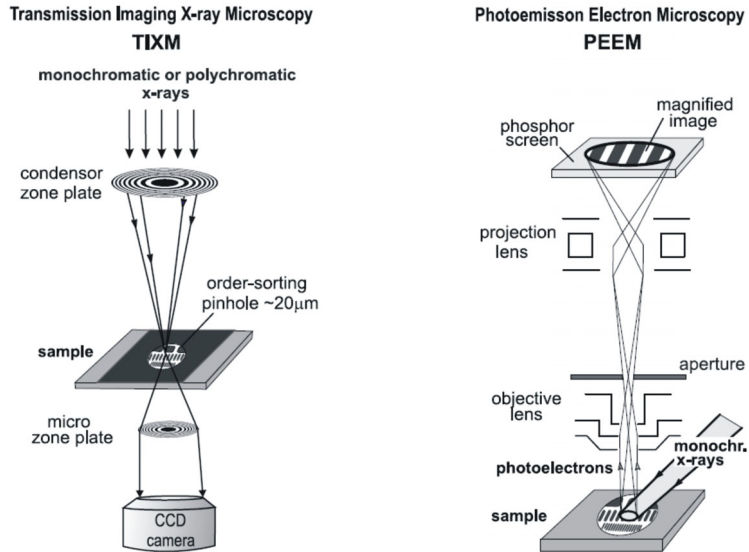


Figure 1.5: Schematic of two x-ray microscopy methods: TIXM and XPEEM [1].

For the XPEEM imaging method a moderately focused x-ray beam is incident on the sample under a grazing angle so that the spot size matches the maximum field of view of the photoelectron microscope (1-50µm). The electrons emitted from the sample are then used for a magnified image by an assembly of electrostatic or magnetic lenses. The spatial resolution is technically limited by the electron optics of the microscope, the energy resolution is determined by the monochromator of the beamline, the size of the aperture and the operation voltage. The fundamental mechanisms limiting the spatial resolution of an XPEEM are spherical aberration, chromatic aberration and diffraction. In practice, for x-ray excitation of electrons chromatic aberrations dominate [1] currently limiting the resolution to be about 20 nm.

Lensless Imaging: Fourier Transform Holography

In contrast to the above real space techniques, where the spatial resolution is limited by the focussing optics, the lensless imaging approach in reciprocal space e.g. X-ray FOURIER Transform Holography (FTH) [34] is an alternative, which has the advantage, that the spatial resolution is fundamentally limited only by the wavelength and therefore promises sub-nm resolution.

Lensless imaging is based on coherent x-ray scattering. If the sample is illuminated with a transversely coherent wavefront the scattering intensity recorded in the far field corresponds to the squared magnitude of the FOURIER transform of the electric field profile at the sample. Yet an inversion is not possible by a direct backtransformation since only the intensity of the coherent scattering pattern is detected without the necessary phase information. However various approaches exist to recover the phase and reconstruct an image, e.g. holography or phase retrieval algorithms.

Coherence Besides the high brilliance the key property of synchrotron radiation for lensless imaging is coherence or specifically the illumination from a monochromatic plane wave [35]. However perfectly coherent sources are generally not available in real experiments. Hence the samples are illuminated with partially coherent waves. Per definition, waves are coherent if they have a constant relative phase. One generally distinguishes between *longitudinal* and *transverse* coherence [36]. *Longitudinal coherence* describes the ability of interference between a wave and a delayed, but spatially not shifted version of itself and can be characterized by a longitudinal coherence length ξ_l , which is given by:

$$\xi_l = \lambda \frac{\lambda}{\Delta\lambda} = \lambda \frac{\nu}{\Delta\nu} = \lambda \frac{E}{\Delta E} \quad (1.28)$$

A monochromator selects radiation with a narrow energy bandwidth and hence can increase the longitudinal coherence. Longitudinal coherence is sometimes also called temporal coherence characterized by a coherence time $\tau_c = \xi_l/c$. *Transverse coherence* is related to the spatial extension where the wavefront is well correlated and hence describes the ability of a wave to interfere with a spatially shifted but non-delayed version of itself. It can be illustrated by an aperture acting as a spatial filter with a radius ω in a distance z from a source. The angular spread of the source is then geometrically limited to $\Delta\theta = (2\omega)/z$. The transverse coherence length is defined as:

$$\xi_t = \frac{\lambda}{\Delta\theta} = \frac{\lambda z}{2\omega} \quad (1.29)$$

The Fourier Transform The probably most important analytical tool in modern optics is the FOURIER transform. For FTH the FOURIER domain in space and spatial frequency is relevant.

The one-dimensional FOURIER transform can be defined as:

$$\mathcal{F}[g(x)] = G(X) = \int_{-\infty}^{\infty} g(x)e^{-i2\pi xX} dx \tag{1.30}$$

where $g(x)$ is a function of x in real space and the reciprocal spatial frequency coordinate X . (The FOURIER transform is denoted by the operator \mathcal{F} and the capitalization of the function $G(X)$.)

The square of the FOURIER transformation $|G|^2$ equals the detected intensity in the spatial domain. According to the convolution theorem the FOURIER transform of the detected intensity is equivalent to the auto-correlation (AC) of $g(x)$, since a multiplication in FOURIER space is equivalent to a convolution in real space, that is $\mathcal{F}[|G|^2] = AC[g(x)]$ [37].

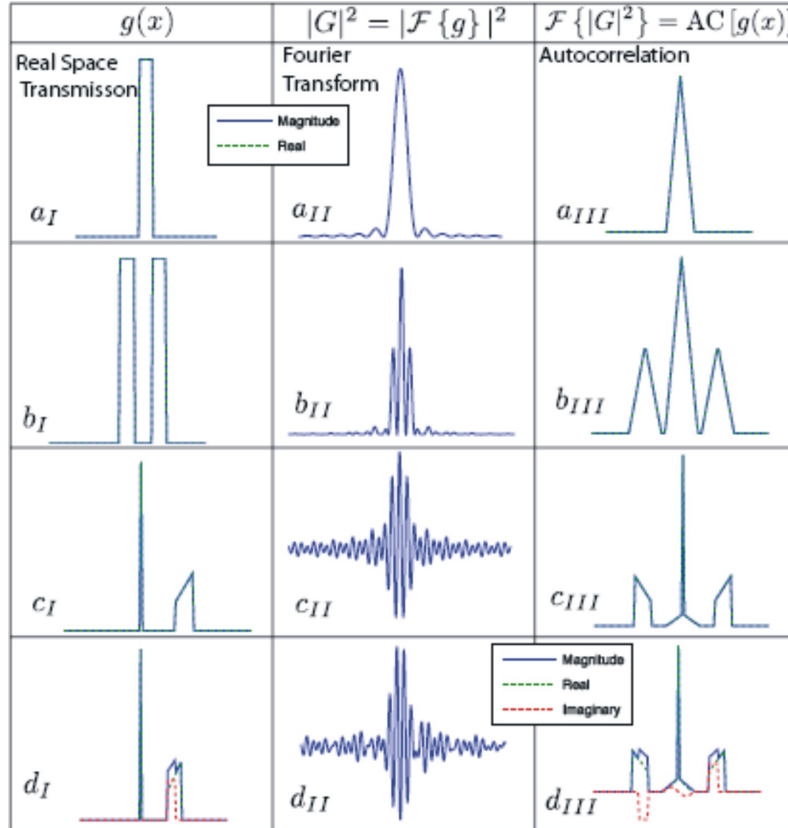


Figure 1.6: Fourier Transformation relationships in one dimension [35].

In figure 1.6 several functions $g(x)$, representing real space transmission functions are shown. In the second column the FOURIER transform of the first column

is given and in the third column the auto-correlation, i.e. the FOURIER transform of column two is given. In figure 1.6(a_I) one can see a rectangle function, which can be thought of as the transmission function of a slit or an aperture. In row (b) there are two of these rectangle functions resembling the double slit transmission. As one can see the FOURIER transform is modulated with a constant frequency and the auto-correlation consists of one central triangular function, often called self-correlation, in the middle of the triangular functions of half the amplitude. These two functions are the cross-correlation and its conjugate.

In row (c) a delta function and an arbitrarily chosen real function are displayed. Since both functions are real, the square of the FOURIER transform is symmetric. Again the self-correlation and the cross-correlation with its conjugate can be seen featuring two mirror images of the arbitrary function. These are exactly the same as images reconstructed from a FOURIER transform hologram. In the last row an imaginary part is added to the arbitrary function resulting in an asymmetric FOURIER intensity. Another difference between the imaginary and the real part can be seen in the auto-correlation, where the magnitude and real curves are even, while the complex one is odd. Fourier transform holography is an extension of these relationships to two dimensions.

Fourier Optics Fourier optics employs mathematical formalisms in the spatial domain known in the time domain for signal processing and hence provides analog and numerical approaches for image processing. FTH is closely related to diffraction, which is often derived starting with the Huygen-Fresnel principle, which describes the diffraction from an aperture filled with an infinite number of point sources collectively generating a diffractive wavefront (for example [38]).

With the Fraunhofer approximation the detectable far field diffraction pattern is equal to the squared magnitude of the two dimensional FOURIER transformation of the object since the intensity ($I = |\mathcal{E}_h|^2$) and not the electric field \mathcal{E}_h is measured.

If a second identical aperture is added in proximity to the first, one yields the typical Young's double slit (pinhole) interference with fringes with a spacial frequency of $f = \frac{2\Delta}{\lambda z}$ and distance 2Δ between the centers of the apertures. The FOURIER transform is the two dimensional version of figure 1.6 b_{II}.

In FOURIER transform holography one of the apertures is approximated by a delta function, so that the cross-correlation terms become images of the transmission of the other aperture. Therefore the well known aperture (approximated by the delta function) is the reference and the other unknown aperture containing the sample is the object.

In figure 1.7 the principal sequence connected to FTH is illustrated. The sample (o) and the reference hole (r), arranged on the transmission mask in a plane perpendicular to the optical axis, are illuminated by a coherent monochromatic

plane wave with an intensity \mathcal{E}_0 from the source leading to a spatially transmitted electric field:

$$\mathcal{E}(x, y) = \mathcal{E}_0 \cdot t_r(x, y) + \mathcal{E}_0 \cdot t_o(x, y) = r(x, y) + o(x, y) \quad (1.31)$$

The transmitted intensity is the squared magnitude. The electric field distribution in the far field can then be calculated by FOURIER transformation of $\mathcal{E}(x, y)$:

$$\mathcal{E}_h(X, Y) = \mathcal{F}[\mathcal{E}(x, y)] = \mathcal{F}[r(x, y)] + \mathcal{F}[o(x, y)] = R(X, Y) + O(X, Y) \quad (1.32)$$

where X and Y are the coordinates in the hologram. The intensity $I_h(X, Y)$ detected by an area detector is the squared magnitude of the electric field distribution in the detection plane:

$$I_h(X, Y) = |R + O|^2 = \underbrace{|R|^2 + |O|^2}_{AC} + \underbrace{OR^* + RO^*}_{XC} \quad (1.33)$$

(Complex conjugate denoted with $*$) The auto-correlation terms (AC) arise from the apertures alone (therefore often also called self-correlation) and the cross-correlation terms (XC) arise from the interference of the waves from both apertures (reference and sample) and hence give rise to the fringes with spatial frequencies inversely proportional to the distance between the centers of the object and the reference hole as for Young's double slit experiment.

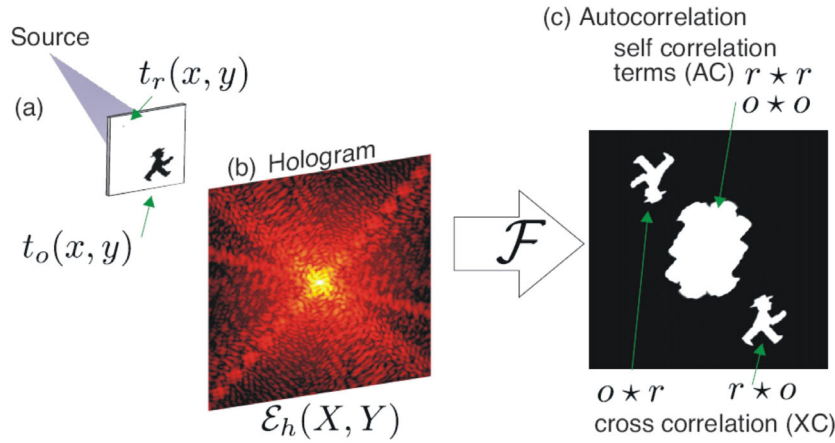


Figure 1.7: Fourier Transform Holography illustrated with a simulated sample [35].

Since the aim of the measurement is to obtain the real space image of the object it is desirable to get $o(x, y)$. As can be seen from equation 1.33 only the sum is measured, and it is impossible to gain the FOURIER inversion of a single term. However, since the cross-correlation terms and self-correlation terms do

not overlap the real space images are reconstructed by the calculation of the two-dimensional FOURIER transformation of the hologram and thereby recovering the encoded phase information:

$$\mathcal{F}[I_h(X, Y)] = \mathcal{F}[|R|^2] + \mathcal{F}[|O|^2] + \mathcal{F}[|OR^*|^2] + \mathcal{F}[|RO^*|^2] \quad (1.34)$$

leading to the real space reconstruction:

$$E_{rec}(u, v) = \underbrace{r \star r + o \star o}_{AC} + \underbrace{o \star r + r \star o}_{XC} \quad (1.35)$$

with the new real space variables u, v and \star indicating complex correlation. There the cross-correlation terms correspond to the twin images, which can be seen in figure 1.7(c). As the reference is a real function with $OR^* = OR$, the cross-correlation term $o \star r$ can be considered as a convolution of $o \cdot r$. The two images only differ by a conjugate and their orientation but contain the same information.

The real space image of the object, which appears in the reconstruction, is the convolution of the actual object with the reference. Thus, in reality the finite diameter of the reference hole blurs the reconstructed image and therefore limits the spatial resolution. However, if the diameter of the reference hole is very small the transmitted intensity is low which leads to a low contrast. Hence the size of the reference hole is always a compromise between resolution and contrast (For a detailed description see [35]).

Chapter 2

Experimental Methods

Synchrotron Radiation

For this thesis measurements have been carried out at three different synchrotron facilities. Spectroscopy using hard x-rays has been done at the European Synchrotron Radiation Facility (ESRF) in Grenoble, France. At the Berliner Elektronenspeicherring - Gesellschaft für Synchrotronstrahlung m.b.H.(BESSY II) soft x-rays were utilized for imaging with XPEEM and at the Stanford Synchrotron Radiation Laboratory (SSRL) in California, USA soft x-rays were used for lensless imaging.

The general functionality of these synchrotron radiation facilities is based on the acceleration of electrons to relativistic speed, which are then orbiting in a storage ring, where they are kept on a circular pace. According to electrodynamics this leads to the emission of electromagnetic radiation, the so-called synchrotron radiation. A mathematical description was introduced by A. LIÉ-NARD and E. WIECHERT using retarded potentials to link the electromagnetic field at the observation point with the charge and current at the time of emission (LIÉ-NARD-WIECHERT potentials)[38]. In contrast to the first generation facilities in modern (second or third generation) synchrotron facilities the generation of synchrotron radiation is fully intentional and optimized for the requirements of users. As an example for such a synchrotron facility a schematic drawing of the BESSY II synchrotron and storage ring is given in figure 2.1. The electrons, generated by thermal emission from a filament, are first pre-accelerated in the microtron and then injected into the synchrotron, where a synchronised magnetic field alternating with high frequency is coupled into cavities to accelerate the electrons further to an energy of 1.7 GeV. In order to keep the electrons on a circular path, readjusted magnetic fields are used. Afterwards the electrons are injected into the storage ring, where the electrons are kept at constant energy with only radiation losses being compensated and the synchrotron radiation is produced at the bending magnets (dipole magnets) or insertion devices (undulators and wigglers). Typical storage ring currents are about 300 mA. Insertion devices consist

of a plane like assembly of magnetic dipoles with orthogonal orientations, which are especially constructed for the generation of synchrotron radiation. The electrons passing through the resulting field distribution are forced by the LORENTZ force on a wobbly path leading to the emission of radiation with very high intensity.

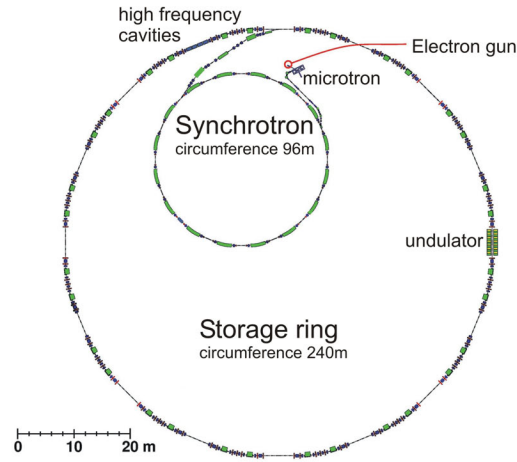


Figure 2.1: Schematic layout of the BESSY II storage ring and accelerator [39].

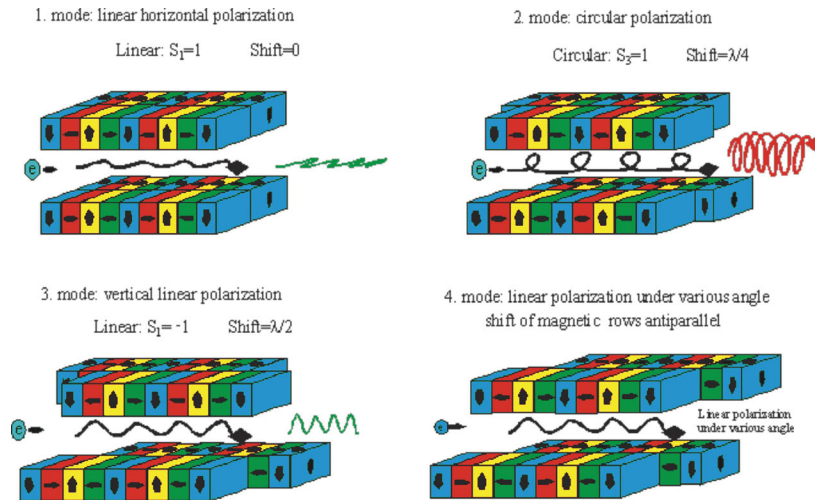


Figure 2.2: Operational modes of the undulator U49 at BESSY II [39].

The beamlines at which work was done for this thesis are all equipped with undulators for which the maximum deflection of the electrons is small enough so that the photons, emitted at different points along the path, interfere with each

other resulting in radiation with a high brilliance within a small angular range. For an illustration of the functional principle the undulator UE49 at BESSY II can be seen schematically in figure 2.2. The undulator UE49 has a magnetic field distribution with a period length $\lambda = 49$ mm. The magnets are arranged in four rows with two each in a plane, where the vertical distance (gap) between the magnets determines the energy maximum of the emitted radiation and the horizontal shift (phase) accounts for polarization. One row each in the top and in the bottom plane can be shifted horizontally by a phase ϕ . For $\phi = 0$ (or $\phi = \lambda/2$) the electrons move along a wiggly line within a horizontal (vertical) plane emitting horizontal (vertical) linear polarized radiation. For the generation of circularly polarized x-rays the shift equals $\phi = \lambda/4$.

The beamlines themselves which are located at the undulator are generally equipped with focussing optics and monochromators also. These monochromators comprise a dispersive element, which normally is a grating for soft x-rays and a crystal for hard x-rays due to the different absorption cross-sections of these two x-ray regimes.

2.1 Spectroscopy using Synchrotron Radiation

2.1.1 Beamline ID-12 (ESRF)

The layout of the synchrotron facility at Grenoble is similar to that of BESSY II. The electrons are accelerated in a linear accelerator (LINAC), then accelerated in the synchrotron to 6 GeV and injected into the storage ring (circumference of 844 m).

For generation of x-rays three helical undulators are available at beamline ID-12 at the ESRF allowing polarization control for an energy range of 2 - 20 keV [40, 41]. Either circularly or linearly polarized x-ray photons can be generated by any of the three helical undulators APPLE-II, HELIOS-II and the so-called ElectroMagnet/Permanent magnet Hybrid Undulator (EMPHU) with a magnetic period λ ranging from 38 mm to 80 mm respectively and hence being optimal for different energy ranges. The helicity of the x-rays can be changed in less than 10 seconds. The polarization of the x-rays, however, is not only dependent on the undulator, but also on the successive optical components of the beamline like the monochromator for example. The polarization rates (i.e. Poincaré-Stokes parameters) can be described by polarization transfer functions [40].

To monochromise the x-rays a fixed exit slit monochromator consisting of a Si(111) double crystal typically cooled to -140°C is used. In order to measure the incoming intensity I_0 different metal meshes are available, e.g. Ti for Co to measure the photocurrent. For the various types of measurements different endstations are used. All XANES spectra were normalized with respect to the edge.

2.1.2 X-ray Magnetic Circular Dichroism (XMCD) Setup

For XMCD measurements two different endstations were used. At one endstation the sample is positioned between the pole pieces of an electromagnet with a bipolar power supply, which can generate a magnetic field up to ± 0.6 T. The sample temperature can be decreased to $T \approx 15$ K. The advantage of this so-called flipper magnet is the short field reversal time, which allows small fieldsteps. For this configuration a photodiode is positioned under 90° with respect to the x-ray beam. Filters consisting of a thin metal foil (e.g. Fe for Co) can be put in front of the photodiode to attenuate low energy electrons and therefore reduce background signals.

At the other endstation a superconducting magnet can provide a magnetic field up to ± 6 T. Sample temperatures from $T \approx 6$ K to $T \approx 800$ K can be reached. The beam is incident on the sample through the photodiode, so that no filters can be used.

The samples are mounted under a grazing incidence of 10° or normal to the x-ray beam, with the magnetic field applied parallel to the direction of the beam.

2.1.3 X-ray Linear Dichroism (XLD) Setup

Apart from spectroscopy using circular polarized x-rays also linear polarized x-rays were utilized. In addition to the undulator a Quarter Wave Plate (QWP) was employed in order to achieve linear polarization. The Quarter Wave Plate is a 0.9 mm thin diamond (111) plate, which exploits the fact that in forward BRAGG diffraction of circularly polarized light, the polarization at the sides of the diffraction peak is linear. Therefore this instrument allows to convert the circular polarized x-rays from the undulator into linear polarized x-rays with the polarization vector rotated in any direction around the direction of the propagation direction of the incident beam [40, 41]. For the measurements the polarization is flipped from horizontal to vertical with a frequency of 1 Hz for every energy point of a spectrum by a slight rotation of the QWP. Another advantage of the QWP besides the fast switching times for the polarization direction is the stability of the beam position on the sample for the different polarization directions reducing artefacts in the experimental data.

To analyse the degree of polarization and for aligning the QWP a kapton foil as beamsplitter together with a photodiode under 90° with respect to the x-ray beam is available. (A schematic can be found in the appendix in figure B.1 and figure B.2.)

For signal detection a cube is available comprising 8 photodiodes with filters, which allow simultaneous detection and therefore to discard the signal from individual photodiodes in case of BRAGG diffraction peaks from the sample in the angular range of detection of the photodiode.

2.2 Imaging using Synchrotron Radiation

2.2.1 Beamline 13-3 (SSRL)

The measurements done at beamline 13-3 at the SPEAR3 (Stanford Positron Electron Asymmetric Ring) storage ring at Stanford Synchrotron Radiation Laboratory (SSRL) rely strongly on the coherence of the radiation. The synchrotron sources are partially coherent, however, the beamline components including monochromators, optics and apertures are also important for the degree of coherence of the radiation (as described in chapter 1.2.2). The entire beamline 13-3 components were moved in the beginning of this year (2008) from their old position at former beamline 5-2, where it was planned to be serviced by a new elliptically polarized undulator (EPU). Since the EPU was not completed due to an unforeseen occurrence, the old EPU was used. The speckle chamber endstation was originally constructed at SSRL in 2002 ([35] and references therein) but has been modified since then. The monochromator is a spherical grating mirror (SGM) in a ROWLAND circle setup and contains three gratings with rulings of 300 lines/mm for radiation in the energy range of 150-400 eV, 600 lines/mm for 350-750 eV and one grating with 1100 lines/mm for 600-1200 eV. A horizontal and a vertical spherical mirror serve as focussing optics and allow a spot size down to $24\ \mu\text{m}$ (vertical) \times $240\ \mu\text{m}$ (horizontal) on the sample.

The endstation (speckle chamber endstation) used for lensless imaging at beamline 13-3 consists of several crosses. The first one is the so-called coherence cross, which is outfitted with a manipulator and typically introduces coherence apertures or spectral filters to the beam. The beam intensity can be measured with a gold mesh, in the next cross, which is followed by the sample cross. The manipulation of the sample is accomplished with a manipulator, which is inserted from the top. A flow-cryostat allows sample temperatures from 20 to 300 K. A second manipulator allows to position the guard aperture baffle. For magnetic measurements the pole pieces of an electromagnet can be inserted, which create a magnetic field of up to 0.11 T at the sample location.

As a detector a backside illuminated PI-MTE 1340 in-vacuum CCD (Charge Coupled Device) camera manufactured by Princeton Instruments was used [42]. The CCD camera consists of an array of 1300×1340 thermo-electrically cooled pixels with an individual pixel size of $20\ \mu\text{m}$. Technical details and a description of the in-vacuum mounting can be found in [35]. The distance between the camera and the sample can be adjusted and thus allows for the momentum transfer range to be optimized. The minimal camera sample distance is 20 mm, which results in a numerical aperture $\text{NA}=0.545$ and a maximal momentum transfer (at 800 eV) of $2.3\ \text{nm}^{-1}$, a field of view (FoV) in real space of $2\ \mu\text{m}$ and a corresponding pixel size in real space of 1.4 nm. A maximum distance of 420 mm between sample and CCD yields $\text{NA}=0.031$, a maximal momentum transfer of $0.125\ \text{nm}^{-1}$ and a

corresponding field of view in real space of $16.2\ \mu\text{m}$ with a pixel size of $25\ \text{nm}$ in real space.

In figure 2.3 a schematic of the components needed for FTH is shown. Representative for all beamline components, which are necessary to produce the monochromatic and focused beam an undulator is shown. A pinhole, which serves as coherence aperture is also necessary in order to increase the coherence of the radiation illuminating the sample. For this reason during the measurements the settings for the beamline were always chosen in a way, that the blue edge of the undulator peak was utilized because the radiation has a higher degree of coherence there.

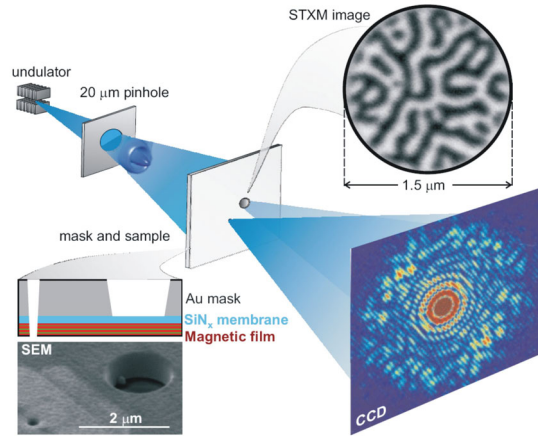


Figure 2.3: Scheme of the setup for X-ray Fourier Transform Holography [34].

The sample itself is a key component of the experimental FTH setup. However, since it is closely linked to the studied system the sample structure is described in chapter 3.2.

2.2.2 Beamline UE49-PGM-1-SPEEM (BESSY)

Beamline UE49-PGM-1-SPEEM is equipped with an elliptically polarizing undulator and a plane grating mirror (PGM) as monochromator. Thereby an energy regime from 150 to 1800 eV is accessible with an energy resolution of $E/\Delta E=10000$ at 700 eV. As this beamline is a microfocus beamline a light spot of $8 \times 34\ \mu\text{m}^2$ (FWHM) on the sample is realized with focussing optics via mirrors. Note, that the grazing incidence of 16° is responsible for the widening in one direction. At this beamline a photon flux of 10^{11} to 10^{13} photons per second per 100 mA ring current are attainable.

At the BESSY II beamline UE-49 a commercial Elmitec PEEM (type PEEM III [43]) is installed, which allows a maximum spatial resolution of 20 nm. It

is equipped with an energy analyser ($dE < 0.5 \text{ eV}$) for the detected electrons (El-emitec SPEPEEM) and two Mott detectors leading to the name S-PEEM (S for spin polarized). However the Mott detectors were not used for the present work.

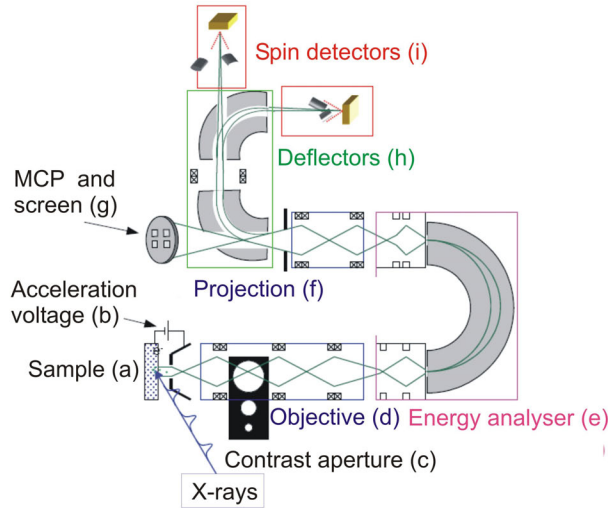


Figure 2.4: Setup of the S-PEEM at BESSY (adapted from [44]).

Electrons are excited by x-rays impinging on the sample (a) on a starting potential of -20 kV and accelerated by a voltage (b). A lens system of objective (d) and projective (f) is responsible for the imaging process. An energy analyzer (e) allows a selection of electrons with a certain energy via an adjustable gap and therefore reduces chromatic aberration. In addition to the lenses, two stigmators and four defectors are installed for aberrations correction. Stigmators are used to correct for astigmatism occurring if the beam is not incident on the lenses parallel to the optical axis. Defectors shift the real image without distorting it. A contrast aperture, which consists of metal stripes with three aperture openings which can be moved in a plane allows to select electron trajectories with a certain angular range to reduce aberration and enhance the achievable spatial resolution. In the imaging mode the electron beam is amplified by a micro-channel plate (MCP) and then converted into visible light by a YAG (Yttrium Aluminium Garnet) fluorescence screen (g), which is then detected by a CCD (charge coupled device) camera. An MCP is a flat area resolving secondary electron multiplier, which consists of one plate with microscopic channels (typically of the order of $10 \mu\text{m}$ apart from each other) and one continuous plate with a high voltage between them. Each electron hitting the wall of a channel then creates a cascade of secondary electrons.

In order to be able to apply a magnetic field during the measurements, a special sample holder was designed for the PEEM and is shown in figure 2.5. As a magnetic field exerts a force on the photoelectrons it is generally not trivial to apply a magnetic field during the measurements because the field distorts the image.

The sample holder with an integrated electro magnet close to the sample was developed at BESSY II after a model sample holder first realized by F. NOLTING at the SLS (Swiss Light Source). It also allows for a sample temperature from 120 K to 1800 K. The sample holder consists of a magnetic yoke, two coils and a covering plate with a hole, which serves as fixation for the sample, but also as a part for the first lens of the photoelectron microscope. Thereby a magnetic field is generated which is locally confined to the sample.

Four electrical contacts are available; the contacts used for the heating filament in the commercial sample holder are used for electric power supply to the electromagnet and were upgraded to offer the possibility to reverse the polarity and of disconnection of the electric circuit. Since both sample holder and power supply are on a potential of 20 kV with respect to ground this was realized by a pneumatic switch.

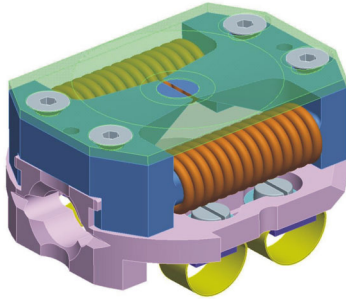


Figure 2.5: Magnetic sample holder for the S-PEEM at BESSY II [45].

A sample holder with a gap of $500 \mu\text{m}$ was used allowing to apply a magnetic field of up to 20 mT without any loss of resolution. However a slight distortion of the image along one axis could be observed for such large fields. For this sample holder a current of 1 mA results in a magnetic field of 0.09 mT.

2.3 Superconducting Quantum Interference Device (SQUID)

SQUID magnetometry is a very sensitive technique to magnetically characterize samples. A SQUID consists of a superconducting loop and a weak link, the so-called JOSEPHSON junction. A JOSEPHSON junction is an insulating layer

interrupting the superconductor. Since it is not superconducting it allows only a tunnel current to pass through. The current I flowing through an ideal junction is then given by the dc-Josephson equation:

$$I = I_0 \cdot \sin\delta \quad (2.1)$$

where $\delta = \Theta_1 - \Theta_2$ is the difference between the two phases Θ_i of the state function $\Psi = \Psi_0 \cdot e^{i\Theta_i}$ at both sides of the junction of the superconductor. The voltage drop across the junction is given by the ac-Josephson equation:

$$V = \frac{\hbar}{2e} \left(\frac{d\delta}{dt} \right) \quad (2.2)$$

In a superconducting loop there can only be a magnetic flux, which is a multiple of the flux quantum Φ_0 : $n \cdot \Phi_0$ with an integer n .

A change in flux through the loop will then result in a current compensating that change leading to a change of the relative phase δ and hence giving rise to voltage oscillations. For a SQUID this oscillating voltage is linearized with a so-called flux-locked-loop for detection of the flux through the loop (which is described in [46] and references therein).

For this work a commercial SQUID magnetometer MPMS (Magnetic Property Measurement Systems) XL from Quantum Design was used [47]. The MPMS system comprises a dewar, probe and SQUID assembly and an electronic control system. The dewar consists of an inner liquid helium reservoir and outer liquid nitrogen jacket to reduce excessive liquid helium boil off. The liquid helium is used both for maintaining the electromagnet in a superconducting state and for cooling the sample space. The probe contains a temperature control system allowing measurements from 1.7K up to 400 K and a superconducting electromagnet, which can supply a magnetic field up to 5 T. The magnetic field is not directly measured, but is determined by the voltage drop over a shunt resistor (and then amplified by a factor of 21 before it is compared with the set voltage of the control board). In order to cover the wide range, two shunt resistors are used, one for fields below 350 mT (hi-res disabled mode) and one for higher fields (hi-res enabled mode). They have to be carefully calibrated with respect to each other.

In order to cover a large range of magnetization values the MPMS SQUID offers different sensitivity ranges (emu-ranges), which can be selected by the device itself with an autoranging option. For that purpose two factors were adjusted, either the gain of the voltmeter card by a given factor (gain) or the time constant of the integrator in the rf amplifier (range) of the rf-SQUID (Model 2000). For each change of the emu-range the 'gain' is altered, whereas the 'range' is only changed every three emu-ranges. An exception is the high sensitivity regime, where the four emu-ranges with the highest sensitivity have the same 'range'. Discrete jumps in recorded hysteresis are visible upon switching the 'range', which can

lead to artificial hysteresis if the sensitivity range is not changed at the same field point by the SQUID. These artefacts must be corrected for as described in [48].

For all measurements the RSO (reciprocating sample option) of the MPMS SQUID was used, which offers a by a factor of ten higher sensitivity than the standard dc-transport. Unlike usual measurements where the sample is moved through the coils in discrete steps the RSO measurements are performed using a servo motor, which oscillates the sample. An encoder records the position of the sample simultaneously with the SQUID signal and the acquired data is then fitted to an ideal dipole moment response to determine the x-position of the sample. The x-position can also serve as a hint for artefacts in the measurements due to improper sample handling, e.g. by a shifted x-position of several millimeters, which can result from magnetic specimen at the edge of a sample as described in [48]. Samples are mounted within a clear plastic straw, which is connected to one end of a sample rod and is inserted into the dewar/probe. The samples, which were usually cut to a size of approximately $5 \times 5 \text{ mm}^2$ were held in place inside the straw without any other means than by clamping them in-between the two walls of the straw, which creates only little indentations in the wall of the straw. For this configuration the background signal from the sample holder is minimal. For other sample holder configurations, e.g., by using other means to mount the sample in the straw like little cotton balls or pieces of other straws lead to a stronger background signal and are therefore not desirable for low-signal samples.

In most cases the magnetic field was applied along the sample plane (along the straw). For measurements in an in-plane and out-of-plane configuration the sample is rotated inside the straw with the help of two wooden sticks, if possible without creation of further indentations for that is the only reliable way of comparing magnetization data for low-signal samples. Possible pitfalls and artefacts, which are characteristic for the measurement of small magnetic signals with the MPMS SQUID need to be taken into account especially for the study of DMS materials [48, 49].

Chapter 3

Sample preparation

In this chapter the preparation and standard characterization of the samples studied for this thesis are described. Two different sample systems were studied: $\text{Zn}_{1-x}\text{Co}_x\text{O}$ (Co:ZnO) films and $\text{Fe}/\text{Fe}_x\text{O}_y$ nanocubes and nanocube ensembles.

3.1 Co:ZnO

Zinc oxide

ZnO is a II-VI semiconductor with a wide direct band gap of $E_g=3.44\text{ eV}$ at 4 K [50]. It grows in the hexagonal wurtzite structure with a $P6_3mc$ symmetry consisting of an equal amount of Zn and O atoms tetrahedrally coordinated. In figure 4.6 such a crystal is shown with the oxygen atoms depicted in green and the zinc atoms depicted in red. The zinc atoms occupy positions with coordinates $\frac{1}{3}, \frac{2}{3}, 0$ and at $\frac{2}{3}, \frac{1}{3}, \frac{1}{2}$ whereas oxygen atoms occupy the positions $\frac{1}{3}, \frac{2}{3}, u$ and $\frac{2}{3}, \frac{1}{3}, u + \frac{1}{2}$. As one can see in figure 4.6 the crystal consists of a hexagonal close packed (hcp) sublattice of oxygen atoms and an hcp sublattice of zinc atoms which are shifted vertically. This shift is described by the u -parameter, which has a value of $u = \frac{3}{8} = 0.375$ (in lattice constants) for ideal tetrahedral coordination. However, for ZnO it has an about 1.8% larger value of $u = 0.3817$. The lattice constants of bulk ZnO are $a = 3.2501 \text{ \AA}$ and $c = 5.2071 \text{ \AA}$ as determined by powder neutron diffraction [51]. The heteroepitaxial growth of ZnO films is mostly done on r-plane (01 $\bar{1}$ 2) or c-plane (0001) Al_2O_3 substrates, exhibiting a large lattice mismatch (c-plane: $a_{\text{Al}_2\text{O}_3} = 4.75 \text{ \AA}$), which leads to strain and lattice defects especially in the bottom layers of the ZnO film.

Co:ZnO Growth by Pulsed Laser Deposition

Thin films of Co:ZnO were grown by pulsed laser deposition (PLD) in the group of S. A. CHAMBERS at the Pacific Northwest National Laboratory in Richland, USA. The substrates are single crystal single-side epi-polished c-plane sapphire

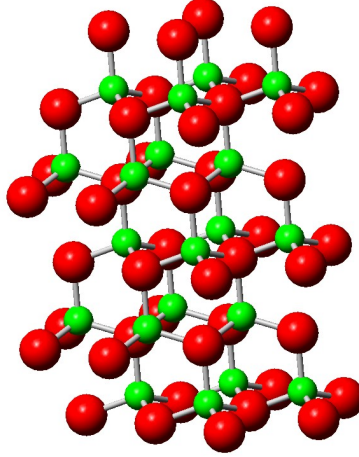


Figure 3.1: Wurtzite ZnO crystal with tetrahedrally coordinated oxygen atoms (small green spheres) and zinc atoms (larger red spheres).

$\text{Al}_2\text{O}_3(0001)$ [52], which are cleaned from residual ferromagnetic contamination by etching (of the backside and the edges) in concentrated HNO_3 and afterwards measured by vibrating sample magnetometry (VSM) to ensure cleanness as described in [4, 53].

The PLD chamber with a base pressure of $<2 \cdot 10^{-8}$ Torr is set up in an off-axis configuration to minimize the deposition of droplets on the substrate. A KrF laser with a wavelength of 248 nm, a power of 2.4 Jcm^{-2} and a pulse repetition rate of 1-20 Hz was used for ablation. With these parameters and an oxygen pressure of 10 mTorr an epitaxial Co:ZnO film was grown at 550°C with a growth rate of 0.25 \AA/sec on the sapphire substrates. The total film thickness was measured to be $105(1) \text{ nm}$ using x-ray reflectivity as can be seen in figure 3.2 on the right and the Co concentration x was determined to be $x=0.108$ using proton induced x-ray emission.

X-ray diffraction (XRD) indicates high structural perfection with a full-width at half maximum (FWHM) of 0.38° in the ω -rocking curve of the (0002) reflection of ZnO which itself has a FWHM of less than 0.15° in the 2θ scan. In figure 3.2 the 2θ -scan and the ω -rocking curve are shown. The FWHM of the 2θ diffraction peak is a measure for the distribution of lattice spacing in the crystal and the FWHM of the ω -rocking peak for the tilt between the crystallographic orientation of the individual crystallites.

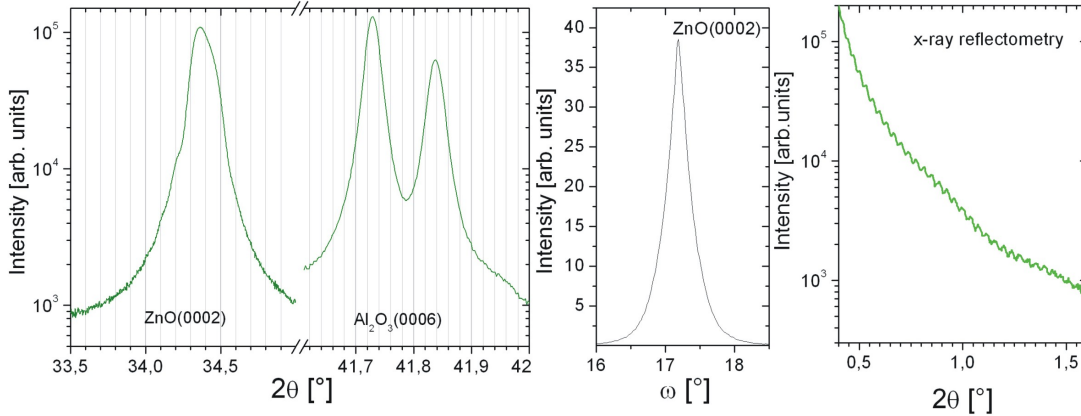


Figure 3.2: XRD scans for the PLD grown Co:ZnO film: ZnO(0002) and Al₂O₃(0006) peaks of the 2θ scan (left), ZnO(0002) peak for the ω - rocking curve (center) and the fringes in the 2θ reflectometry scan (right).

Sputtered Co:ZnO

Apart from the films of Co-doped ZnO grown by PLD, sputtered films were studied as well. These were grown in Duisburg in the preparation chamber of the MAGLOMAT (Magneto LOGic MATerials) group. The experimental setup of this chamber is described in detail in [54]. The nominally 10% Co:ZnO epitaxial films were grown on epi-ready c-plane sapphire substrates [52] using reactive dc-magnetron sputtering from metal targets. The ultrahigh vacuum deposition system has a base pressure of 5×10^{-10} mbar. Optimal growth conditions were obtained at substrate temperatures (T_{prep}) of about 350°C and 450°C and gas pressure during deposition of 4×10^{-3} mbar. The Ar to O₂ ratio, which was adjusted with two separate mass flow controllers was varied between 10 : 5 and 10 : 0.3. For the highest quality sample the preparation temperature of the substrate was $T_{prep} = 350^\circ\text{C}$ and the Ar to O₂ ratio was 10:1. The global structure was studied with XRD. For the sputtered sample with the highest structural quality a FWHM of 0.75° of the ZnO(0002) reflection in the ω - rocking and less than 0.15° in the 2θ scan indicate the good long range crystallographic order similar to the PLD grown Co:ZnO samples.

ZnO Growth by Molecular Beam Epitaxy

High quality undoped ZnO samples were grown by plasma-assisted molecular beam epitaxy (PAMBE) at the Walter Schottky Institute (WSI) in Munich, Germany.

Here the lattice mismatch between ZnO and sapphire substrate [52] is accommodated by an optimized buffer layer of ZnMgO to accomplish two-dimensional

growth. In contrast to the sputtered and the PLD grown samples, the strain and lattice mismatch is then relieved within the 10-20 nm thick buffer layer allowing clean growth of the ZnO film on top. During preparation the MBE system was operated at temperatures between 560°C / 370°C and 575°C / 440°C for hotlip and crucible, respectively. The elevated temperature of the hotlip hindered a blocking of the crucible aperture. The use of in-situ reflection high energy electron diffraction (RHEED) to optimize the growth parameters allows the deposition of films with excellent structural properties as confirmed by high resolution x-ray diffraction (HRXRD) with a FWHM of 0.0069° for the ZnO(002) peak and 0.52° for the ZnO(101) peak for the ω -rocking curves and a FWHM of 0.03° for the 2θ scan of the ZnO(002) peak. The thickness of the film is 308 nm as determined by XRD.

3.2 Fe/Fe_xO_y Nanocubes

Synthesis

Nanoparticles can be fabricated using various methods, i.e. wet-chemical synthesis or condensation from the gas phase, but for our experiments solely colloidal nanoparticles were used. The Fe/Fe_xO_y core/shell nanoparticles were fabricated by wet-chemistry by A. SHAVEL *et al.* [55] in Vigo, Spain in the group of Prof. L. M. LIZ-MARZÁN.

The synthesis was carried out by decomposition of a metal precursor (iron oleate complex) at high temperatures. The iron oleate complex was prepared by the group itself beforehand. For the preparation of the Fe/Fe_xO_y nanocrystals this iron precursor (iron oleate complex (NaOL₃)), sodium oleate (TCI 95%) and oleic acid were dissolved in squalene. The reaction mixture was degassed under vacuum for 1-2 hours at 175°C. Afterwards the mixture was heated to the boiling point (of about 310-329°C) and kept at that temperature for two hours. Afterwards it was cooled to room temperature and washed several times by first precipitating with acetone and then redispersing the particles in chloroform. This fabrication technique yields cubic iron nanoparticles, which are covered with an FeO_x shell of about 2-3nm and have a side length of about 18nm. Two different particles suspensions were synthesized in this way. In the last precipitation cycle the nanoparticles were redispersed in the liquid in which they were afterwards kept, that is a composition of 50% squalene and 50% tetracosan for the suspension (V103) utilized to prepare the samples studied at BESSY and a composition of 25% squalene and 75% of a paraffine oil for the suspension (V105) for the preparation of samples studied at the SSRL. In figure 3.3 a transmission electron microscopy (TEM) image of the Fe/Fe_xO_y nanocubes is shown. For some of the nanoparticles the core shell structure of the Fe core and the Fe-oxide shell is visible in the TEM contrast. A description of the preparation procedure and a

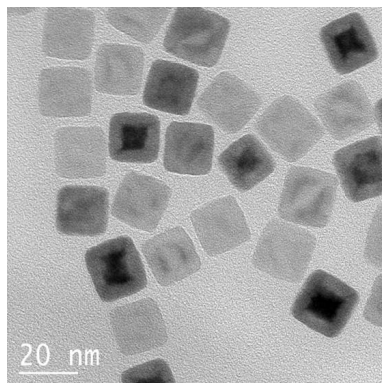


Figure 3.3: TEM image of Fe/Fe_xO_y core/shell nanocubes with typical side length of 18 nm[56].

magnetic and structural characterization of similar Fe/Fe_xO_y nanocubes can be found in [55].

In general there are four types of iron oxides: FeO (wustite), Fe₃O₄ (magnetite), which has an inverse spinel structure and is ferrimagnetic at room temperatures and Fe₂O₃, which exists in two different phases. The γ -Fe₂O₃ (maghemite) also has an inverse spinel structure, however with additional vacancies in octahedron sites, whereas the α -Fe₂O₃ exists in the corundum crystal structure and exhibits weak ferromagnetism with a very low saturation magnetization (0.3 Am²/kg) at room temperature and behaves antiferromagnetically below 263 K ([15] and references therein). As is known from literature the oxide shell of iron nanoparticles is of the spinel type, that is either Fe₃O₄, γ -Fe₂O₃ or a combination of both with thickness, structure and composition strongly dependent on the oxide formation conditions [55, 57].

Sample Preparation

For further investigation, these nanoparticles are deposited on various substrates, e.g. a carbon covered copper grid for TEM studies or naturally oxidized Si and SiN_x substrates for the synchrotron studies. The deposition of the nanoparticles can be done by simply putting a drop of particle suspension on the substrate and then letting the solvent evaporate.

As a result of the chemical synthesis each individual nanoparticle is surrounded by a shell of organic ligands, which prevent the particles from directly touching each other. When the drop of the suspension is put on a substrate and the solvent slowly evaporates the nanoparticles tend to self-organize, which is strongly dependent on the substrate and the dilution of the suspension. The desired coverage of the substrate with about one monolayer or less of nanoparticles was achieved by diluting the suspension with hexane before the deposition

to yield the desired concentration. In order to increase the quality of the self-organization it is also possible to add octane to the suspension to slow down the evaporation progress or to add oleyamin to enhance the separation of the particles. For the V103 particle suspension used to prepare the samples studied at BESSY another option to enhance self-organization was used, that is adding of THF(tetrahydrofuran).

To try to improve the self-organization of nanoparticles from suspension on the substrate spin coating was also employed. For that the substrate is fixed on a plate, which can be rotated with different frequencies. For this preparation method a less diluted particle suspension was used. However in our case no improvement concerning the selforganisation of the particles could be observed. After preparation images of various spots on the samples were taken using a scanning electron microscope (SEM), e.g. figure 3.4 to check for the resulting particle distributions.

Plasma Cleaning: Removal of Organic Ligands and Reduction of the Oxide Shell

For some of the samples the Fe-oxide shell and the organic ligands (oleic acid and oleylamine) are undesirable. This was the case, e.g. for the magnetic x-ray photoemission electron microscopy (XPEEM) measurements at BESSY since XPEEM is not bulk sensitive and therefore probes only the Fe-oxide shell of the nanocubes. Hence, a strong magnetic signal is not expected from non-reduced particles because a strong magnetic signal is only anticipated from the ferromagnetic Fe core. In order to remove the organic ligands from the wet-chemical synthesis and the Fe-oxide shell of the nanoparticles the samples were cleaned using a plasma treatment as described for Co/CoO nanoparticles in [58] and for FePt nanoparticles in [59]. For the removal of the organic ligands an O₂-plasma was utilized. After the ignition of the O₂ plasma (at 0.5 mbar) the pressure of the oxygen was reduced to about 0.05 mbar and kept constant for about 20 min with a power of 30 W. After this treatment the organic ligands are expected to be removed. Subsequently the Fe-oxide of the nanoparticle shell was reduced to Fe by H₂-plasma. After ignition of the H₂-plasma (at a pressure of about 0.7 mbar) the H₂-pressure was reduced to 0.07-0.075 mbar. The H₂-plasma treatment was continued for about 2.5 h.

Since it was not possible to carry out the plasma cleaning in situ at the XPEEM at BESSY, the nanoparticles needed to be protected from reoxidation. For that purpose a thin film of Al was utilized as capping because it has no absorption edges in the vicinity of the Fe edges (especially before the Fe edge, which would lead to a strong absorption of the x-rays by the Al). For that the sample was transferred to the MAGLOMAT preparation chamber under argon gas atmosphere to hinder complete reoxidation. After that another H₂-plasma treatment with a pressure of 0.002 mbar and 40 mA with an ECR (electron cyclotron

resonance) plasma source for about 1.5 h was performed in order to ensure that the Fe-oxide, which was eventually formed during sample transfer, is reduced. The reduced nanoparticles were then capped with an Al film (about 6 nm thick), which was deposited using magnetron sputtering. The 6 nm Al film prevents the Fe from reoxidation, which was checked by taking a spectrum at the Fe L_{2/3}-edges with XPEEM. In the chamber at BESSY the thickness of the Al film was reduced by sputtering. For that two sputtering cycles were performed: First it was sputtered for 20 min with $p_{Ar}=2.5\times 10^{-5}$ mbar, $I_s=10\ \mu\text{A}$ and $E_{kin}=1000$ eV. Only a very small increase of Fe signal was detected. Afterwards it was sputtered for 15 min with $p_{Ar}=1.1\times 10^{-5}$ mbar, $I_s=10\ \mu\text{A}$ and $E_{kin}=1540$ eV. When checked with XPEEM the detected Fe signal was doubled. No difference could be observed for thicker films and no sign of Fe-oxide was visible at the Fe L_{2/3}-edges for the nanoparticles even after exposure to air for several weeks.

BESSY Samples: Single Particle Study

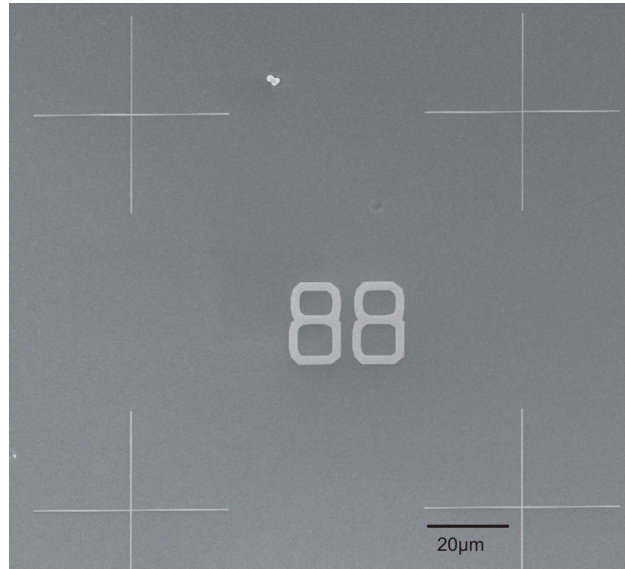


Figure 3.4: SEM image of a section of a nanoparticle sample showing one field with the crosses and the number 88 written with gold by e-beam lithography. (Note that with this magnification the particles are not visible)

For the samples, which were studied with XPEEM at BESSY, a grid of gold crosses and numbers (from number 1 to 100), that were written using e-beam lithography were used as markers in order to be able to relocate spots on the sample later on, to identify specific configurations of nanoparticles. As a substrate naturally oxidized 10 mm × 10 mm × 500 μm Si wafers were used. Such a gold marker on a substrate with nanoparticle deposition on top is shown in figure 3.4.

One can see the number 88 in a box of four crosses. The gold structures on the substrate were necessary for another reason apart from finding nanoparticle assemblies again. Since the absorption of gold is almost constant in the energy range around the resonance of the Fe $L_{2/3}$ -edges, the markers are visible for the whole energy range of the spectrum in XPEEM. Therefore the markers allow to align a series of images and correct for the drift in between. They also serve as a reference for the quality of the image, as the quality of a single image can be estimated by analyzing the sharpness of the edges of the gold markers.

Stanford Samples: Particle Ensembles

The samples studied with FOURIER transform holography (FTH) at the SSRL were different from the ones studied at BESSY with the XPEEM since in FTH the object of interest is inseparably linked to the sample mask with aperture and the reference hole. In figure 3.5 the cross section of such a sample is schematically depicted. In the lower part of figure 3.5 a cross section of the sample is shown consisting of a SiN_x membrane, which is about 150nm thick sitting on a frame of about 200 μm thick Si. On the side from which the window has been etched into the Si the Si_3N_4 membrane is coated with an about 800 nm thick film of gold. In the upper part of figure 3.5 the sample structure in the membrane is enlarged, which is composed of the silicon nitride membrane coated with the thin gold film. A 600 nm diameter aperture is milled into the gold film with focused ion beam (FIB). On the other side of the membrane the object of interest is located, that is in our case the iron nanocubes. Further to the right one can see the reference hole with a diameter of about 50 nm, which is milled through both the gold film and the membrane with the FIB. A detailed description of the sample fabrication can be found in [35].

As described in chapter 1.2.2 the size and the quality of the reference hole determines the quality of the encoded phase information in the hologram and therefore it determines the resolution. Also the quality of the aperture is crucial for the quality of the image, which is retrieved from the hologram speckle pattern. Therefore a sharp aperture with steep (ideally rectangular) edges is almost as important as the quality of the reference hole.

In figure 3.6 Fe/ Fe_xO_y nanocubes (similar to the ones depicted in figure 3.3) deposited on a SiN_x membrane are depicted before the aperture and the reference hole were milled. As one can see the coverage of iron nanocubes is nicely two-dimensional slightly less than one monolayer with an assembly of the particles in agglomerates with spaces in-between. This was desired for the imaging samples because it allows the identification of different nanoparticle configurations on the sample and therefore a comparison with SEM images. By such a comparison of the acquired image with an SEM image one can estimate the achieved resolution, by indentifying single particles or particle configurations and checking if they are individually resolved.

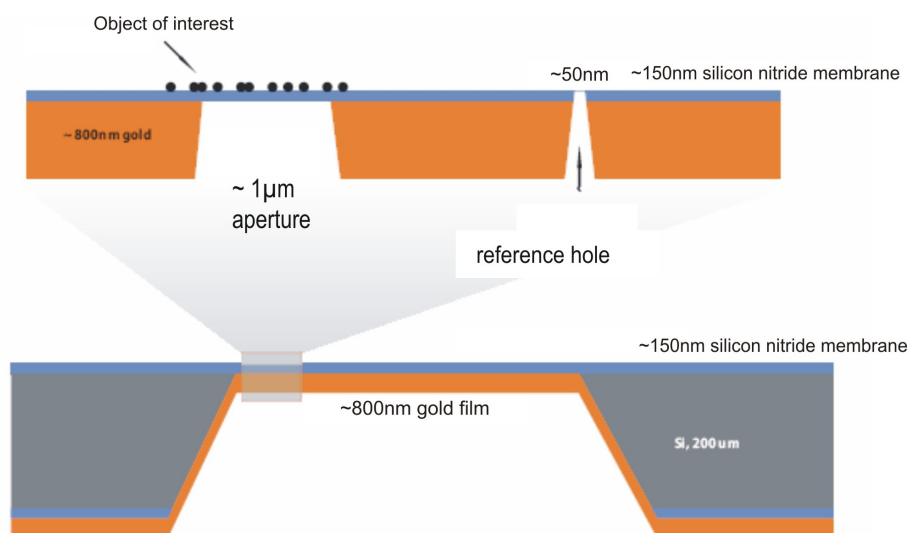


Figure 3.5: Cross section of a sample with a circular object and reference hole for imaging nanoparticles using FTH [60].

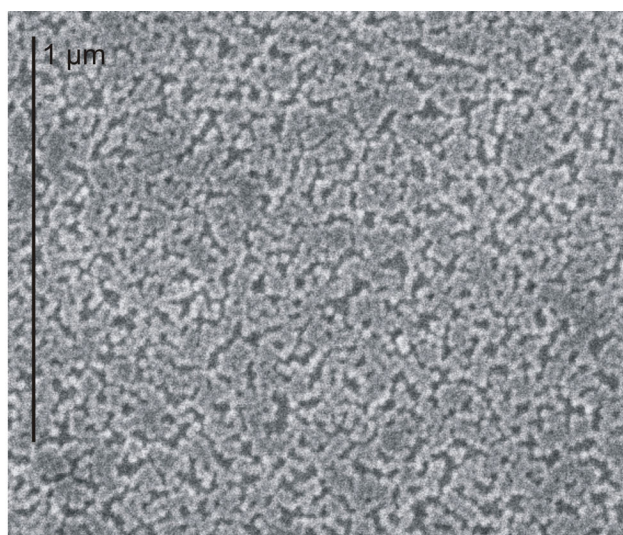


Figure 3.6: Representative SEM image of nanoparticles on the SiN_x membrane.

Chapter 4

Spectroscopy on Dilute Magnetic Semiconductors

Dilute magnetic semiconductors (DMS) are of great interest, because they promise to combine transport properties of semiconductors with long-range magnetic order which allows to utilize the spin in addition to the charge to carry information in spintronic applications like the spin transistor proposed by DATTA and DAS [2]. However, practical device technology requires the presence of long-range magnetic order well above room temperature.

Triggered by the prediction of room temperature ferromagnetism in p-type 5% Mn doped ZnO by DIETL *et al.* [61] transition metal doped ZnO has been widely studied. A promising candidate is $\text{Zn}_{1-x}\text{Co}_x\text{O}$ (Co:ZnO) and is therefore subject to investigation here. Up to now ferromagnetism [3, 62] as well as the absence of the same [4, 63] have been reported at room temperature. Recent *ab initio* calculations based on density functional theory by NAYAK *et al.* [64] also dealing with Co:ZnO concluded, that no room temperature ferromagnetic order can be expected at dopant concentrations below 20%.

In order to distinguish between intrinsic Co:ZnO and phase separated metallic Co clusters which may be responsible for the observed magnetic order, a careful structural characterization is necessary as has been shown by x-ray diffraction analysis [65] and depth-profiling photoelectron spectroscopy [4]. Another possibility for meaningful analysis of the structural properties is by measuring the x-ray linear dichroism (XLD) in combination with the respective model structure simulations. For example, for other systems like Mn:GaN [66] and Gd:GaN [67] measurements of the XLD have ruled out phase separation and antisite disorder, and x-ray magnetic circular dichroism (XMCD) could not confirm the existence of ferromagnetism at elevated temperatures.

In the following the technique of XLD is applied to Co:ZnO and combined with magnetic characterization with XMCD and SQUID measurements to identify the possible existence of long-range ferromagnetic order or to rule it out.

4.1 X-ray Linear Dichroism – Experiment versus Simulation

In this thesis the structure of Co:ZnO was studied by x-ray linear dichroism (XLD), which measures the anisotropy of final states between the a- and the c-plane of the wurtzite crystal, which is caused by the ligand field of neighboring atoms. Therefore the next neighbor interactions are decisive for the dichroism effect and hence the local crystallographic structure is probed.

In order to evaluate the XLD spectra concerning the crystal quality it was very important to define the maximum XLD signal for the 'perfect' crystal to be able to exclude the formation of secondary phases and metallic Co clusters to the largest extent possible and hence utilize the 'perfect' crystal as a reference.

In figure 4.1 one can see XLD spectra taken at the Zn K-edge for three different samples, which all demonstrate good crystallographic properties, but were grown with different preparation techniques as described in chapter 3.1. As one can see the absorption edges are similar and also the XLD spectra display a shape typical for the wurtzite lattice.

However taking a closer look, one can distinguish deviations between the spectra, especially for the spectra of the ZnO film, which was grown by MBE. For this sample the main maximum of the absorption edge (9675 eV) is reduced, while the rest of the features are equally pronounced as in the spectra of the other samples. Also, in the respective XLD spectrum this reduction in peak amplitude is visible for the main maximum at the same energy. The main difference between the samples is the film thickness (apart from the preparation method and the Co doping, which should rather decrease the crystallographic order in the ZnO crystal). This sample has a film thickness of about 300 nm whereas the other two samples are much thinner (only about 100 nm). This implies that the reason for the reduced XLD signal is not a less good structural quality, but the onset of the so-called self-absorption, which can be observed for thicker samples, especially, when measuring at grazing incidence [68, 69]: For a thin sample the detected signal is proportional to the absorption coefficient. However, deep inside a thicker sample the photons have already been attenuated during their way through the sample. Therefore the detected signal is a measure for the absorption and the transmission of the sample at the same time causing a damping of the spectral features. For grazing incidence the path through the sample is additionally prolonged, therefore the effect of self-absorption is significantly increased. Since our measurements were performed at a grazing incidence of 10° self-absorption is likely to be the cause of the reduced signal at the main edge (9675 eV) for the thicker (300 nm) ZnO film.

Thus, in order to determine the structural quality with help of the maximum XLD signal one needs to carefully take into account the different experimental conditions. This is also the case for the degree of linear polarization, which is

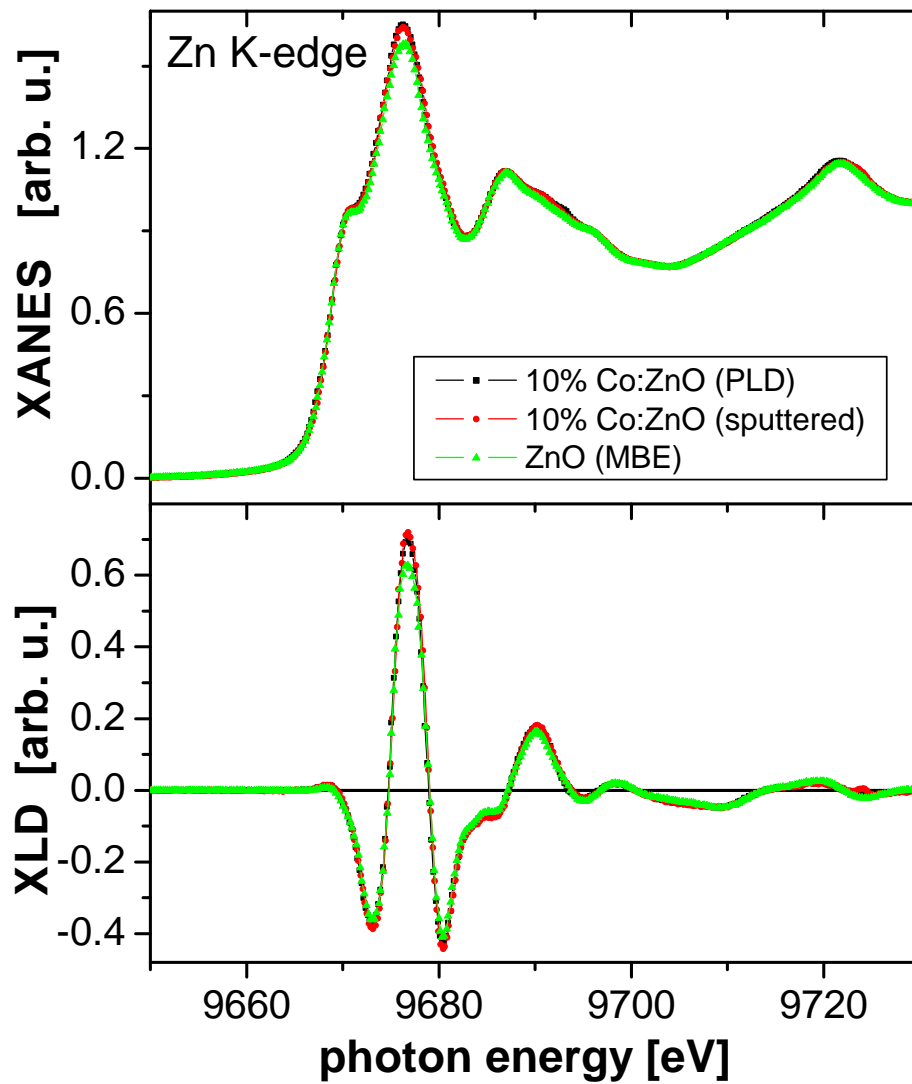


Figure 4.1: XANES and XLD spectra (at $T = 300\text{ K}$) for three samples prepared by different preparation methods and with different film thicknesses: A 100 nm thick PLD grown Co:ZnO (black square), a 100 nm thick sputtered Co:ZnO film (red circle) and a 300 nm thick ZnO grown with MBE (green triangle).

highly dependent on the alignment of the beamline and especially the alignment of the quarter wave plate (QWP). However since all samples have been investigated at the same beamline, namely beamline ID12 at the ESRF, the conditions can be assumed to be identical (with a discrepancy $<1\%$) for all experiments.

In order to evaluate the XLD spectra not only the comparison between individual experimentally obtained spectra is possible, but also the comparison between experimental and simulated spectra offers a deeper insight. Therefore in the next section the simulation of such spectra is described.

4.1.1 Simulation with FDMNES code

For simulation of the XANES and XLD spectra the FDMNES (Finite-Difference Method Near-Edge Spectra) code developed by Y. JOLY [70] was employed, which is a one-electron multiple scattering (Green) formalism. For the use of the FDMNES code two options are available, that is a calculation based on the finite-difference method (FDM) to solve the Schrödinger equation, which allows a completely free potential shape but requires large computational power and another method based on the so-called muffin-tin approximation for the potential, which reduces the computational workload so that the calculations can be easily performed on ordinary office computers.

For our simulations the calculation were exclusively performed using the muffin-tin approximation. In this approximation the potential is spherically averaged in the atomic and outersphere regions and volume averaged in the inter-atomic region resulting in a shape of the potential resembling a muffin-tin and therefore leading to the name. In order to use the FDMNES code to simulate XANES and XLD spectra it is necessary to provide a number of parameters for the crystal lattice and the different kinds of atoms on the various lattice sites. Some of the parameters are discussed in the following.

The lattice parameters for the ZnO lattice were taken from bulk ZnO in literature determined by powder neutron diffraction (at 295 K) [51]. The lattice constants are $a = 3.2501(1) \text{ \AA}$ and $c = 5.2071(1) \text{ \AA}$. For the simulation of ZnO a small cell containing four atoms (two oxygen (O) and two zinc (Zn) atoms) was sufficient. However, in order to simulate a reasonable Co concentration for the Co doped ZnO this unit cell was enlarged to a $\text{Zn}_{23}\text{Co}_{24}\text{O}$ supercell, copying two by two by three ($2 \times 2 \times 3$) times this unit cell.

Zn K-edge

In figure 4.2 experimental and simulated XANES for the electric field vector $E||c$ and $E \perp c$ and the corresponding XLD spectra of a crystal of Co doped ZnO at the Zn K-edge are shown for comparison. The experimental spectrum that is shown for comparison in the following figures of this section is measured using the PLD grown sample already shown in figure 4.1 with a maximum signal of $(70 \pm 1\%)$

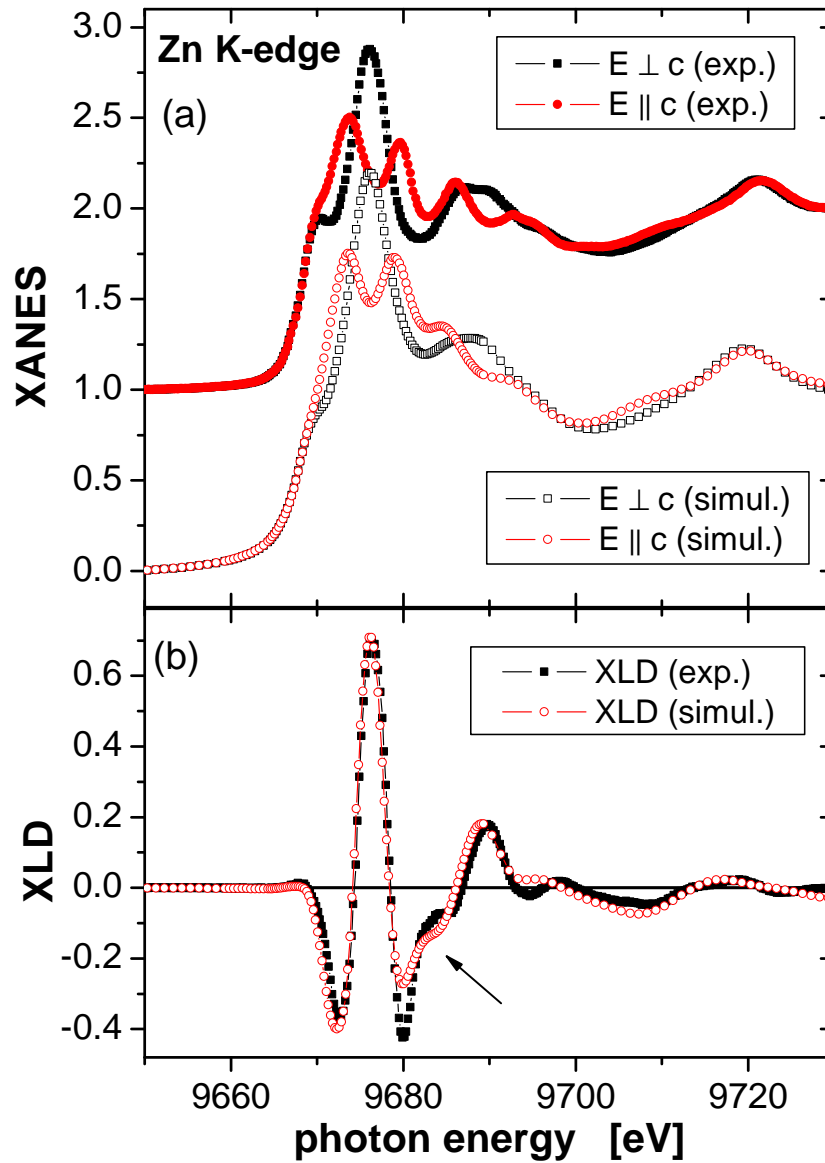


Figure 4.2: Experimental and simulated XANES and XLD spectra at the Zn K-edge (Note that the experimental XANES spectra were shifted vertically by 1).

of the edge jump, indicating that the sample has a good crystallographic quality and that the ZnO wurtzite lattice remains undisturbed by the dopant.

Apart from an overall good agreement between the experiment and the simulation one can see clear deviations in the energy interval slightly above the energy for the maximum XLD signal. These deviations around 9680 eV are generally explained to be caused by the approximation of a muffin-tin potential for the simulation, because this is the energy, where the kinetic energy of the photoelectron is close to the energy assumed for the constant interstitial potential. The approximation also results in a strong dependence of the outcome of the calculation on the size of the interstitial region, but the size is determined by the FDMNES code itself and therefore allows no adjustments by the user of this code.

The simulation of the spectra is done in two consecutive steps, which can be combined in one input file, but also individually. In the first step the spectra are simulated with δ -function like energy levels (with only a little broadening due to the approximations during the calculation). In the second step these spectra are convoluted by a lorentzian with a certain width for the core hole energy level and an additional energy dependent broadening, and moreover the occupied states below the FERMI energy are eliminated.

The FDMNES code calculates the final states for the absorption within a sphere, the radius of which can be specified in the input file in Å. For the calculation only the atoms inside this sphere around the absorbing atom are considered. In order to find out which cluster size is necessary to be able to calculate accurate spectra, simulations with different cluster radii were performed. Some of the simulations are shown in figure 4.3 for the Zn K-edge. Similar simulations were also performed for the Co K-edge and are shown in the appendix in figure C.1.

As one can see from the simulations with different cluster radii in figure 4.3 the agreement between the simulations and the experiment is rather poor below a radius of 8 Å and also the agreement between the simulations for different cluster radii themselves is poor. The difference between the simulations done with a cluster radius of $r = 8.5$ Å and $r = 9$ Å is negligible. This indicates that the spectra obtained with the simulation are converging for a cluster with radii around 8 Å. This indicates therefore that the number of atoms within the sphere of calculation is sufficient for those radii. Consequently in all further simulations a cluster radius of $r = 8.5$ Å was used. In literature, however, where XLD is used for structural characterization one can find simulations done with a cluster radius of only 6 Å [71]. Even though the first minimum is in quite good agreement with the other simulations and the experiment, the main maximum is significantly reduced; it is apparent that a simulation performed with a radius of only 6 Å can only give a very limited accuracy for the judgement of structural quality. It might appear surprising that atoms, which are further away from the absorbing atom than the nearest neighbors have such an influence on the near edge spectra. However, since a multiple scattering formalism is used, also the next nearest

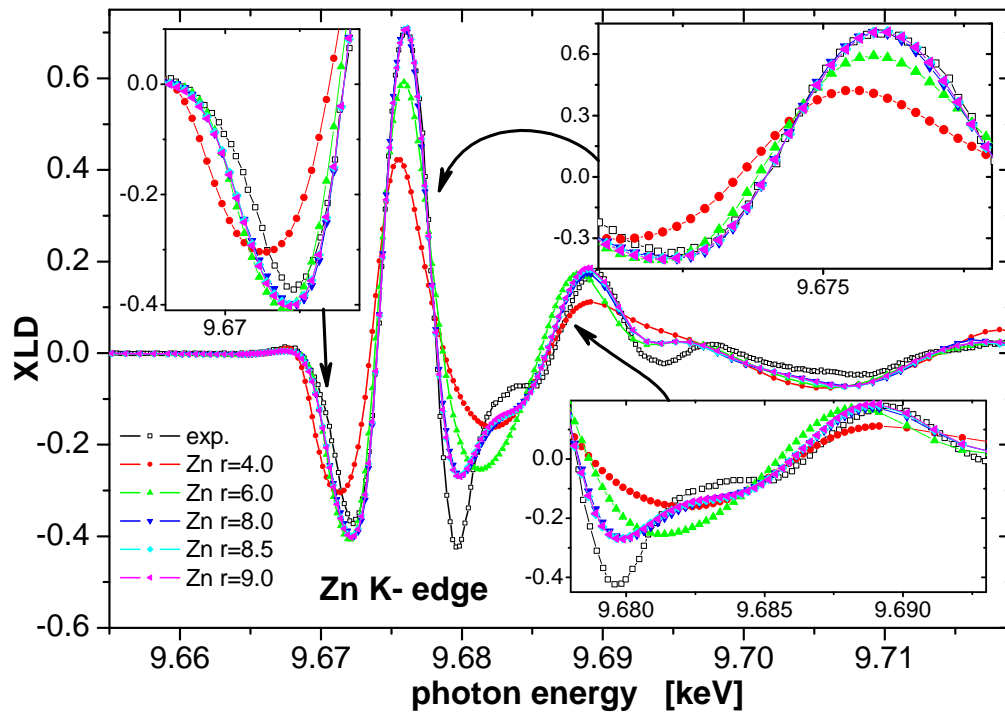


Figure 4.3: XLD spectra at the Zn K-edge simulated with different cluster radii for the simulation (solid symbols) and an experimental spectrum (open symbol) for comparison.

neighbors contribute significantly to the reconstruction of the crystal field for a precise calculation of the scattering paths.

The correct convolution of the spectra is very important, because it has a great influence on the shape of the spectra. In addition to the initial core hole level width Γ_H at E_F an additional energy dependent broadening is introduced. For the FDMNES code an arctangent-formula for the energy dependent broadening was used:

$$\Gamma = \Gamma_H + \Gamma_m \left(\frac{1}{2} + \frac{1}{\pi} \arctan \left(\frac{\pi}{3} \frac{\Gamma_m}{E_{Larg}} \left(e - \frac{1}{e^2} \right) \right) \right) \quad (4.1)$$

with $e = \frac{E-E_F}{E_{cent}}$, where Γ_m is the maximum width of the final states at high energies, and E_{cent} and E_{Larg} are the center and the width of the arctangent function. Such a function can be found in the appendix in figure C.2. The default value for the simulations is given as (30, 30, 15) with (E_{cent} , E_{Large} , Γ_m in eV).

In figure 4.4 a representative selection of those convolutions for the XLD spectra at the Zn K-edge is depicted. An experimental spectrum is shown in black symbols as a reference for comparison. The FERMI level shift E_F and the core level width Γ_H are kept the same. Their influence is illustrated in figure 4.5. As one can see in the part of the spectrum below the edge, the agreement with the experimental data is quite good. At the main maximum, however, the different energy-dependent broadening has an influence on the amplitude.

In figure 4.4 (red symbols) one can see a convolution with a rather small additional broadening, which is also following a slow rising arctangent-like energy-dependent broadening. It is obvious that the XLD amplitude of the main peak is overestimated, whereas the next maximum fits quite well. In contrast, a steeper slope of the arctangent was used for the simulation depicted in green symbols. One notices that both the main peak and the following one are strongly reduced. The best agreement could be achieved with an maximum energy dependent broadening of 9 eV and a medium slope for the arctangent function. Therefore for all future simulations the energy dependent broadening of $E_{cent} = 35$ eV, $E_{Larg} = 35$ eV and $\Gamma_m = 9$ eV was used.

Initially literature value for the width of the core hole level $\Gamma_H = 3.34$ eV (FDMNES: $\Gamma_H = 2 \cdot (FWHM)$ of the natural atomic line widths as determined semi-empirically from fluorescence) was taken [72]. The FERMI level determined by the FDMNES code can be additionally shifted by a value E_F which allows to include levels, which are just below the calculated FERMI level, but due to a natural broadening have an influence on the experimental spectra. In order to reconstruct such features right below the absorption edge, at the so-called pre-edge a negative shift value E_F can be introduced. In figure 4.5 one can see a simulation without any shift of the FERMI level with the literature core hole width $\Gamma_H = 3.34$ eV (light blue diamond). Especially at lower energies the agreement

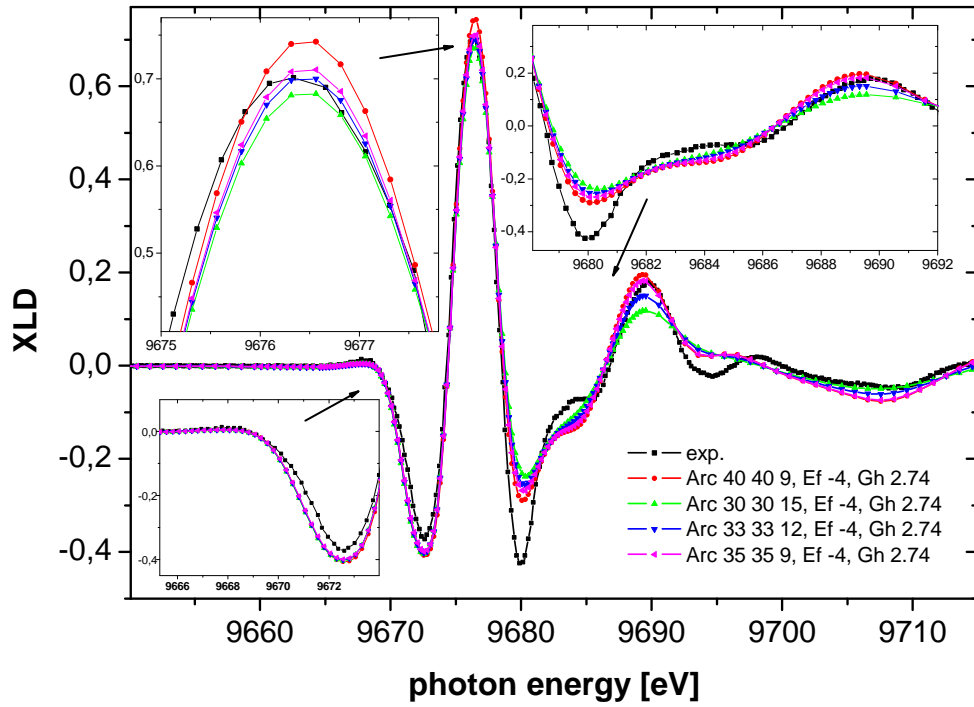


Figure 4.4: Simulated XLD spectra at the Zn K-edge convoluted with different parameters for the energy dependent level-broadening with arc E_{cent} E_{Large} Γ_m in eV, a shift of the FERMIL level $E_F = -4$ eV and the core level width $\Gamma_H = 2.74$ eV.

with the experimental data is not good, because the first little bump below the edge is not reproduced at all.

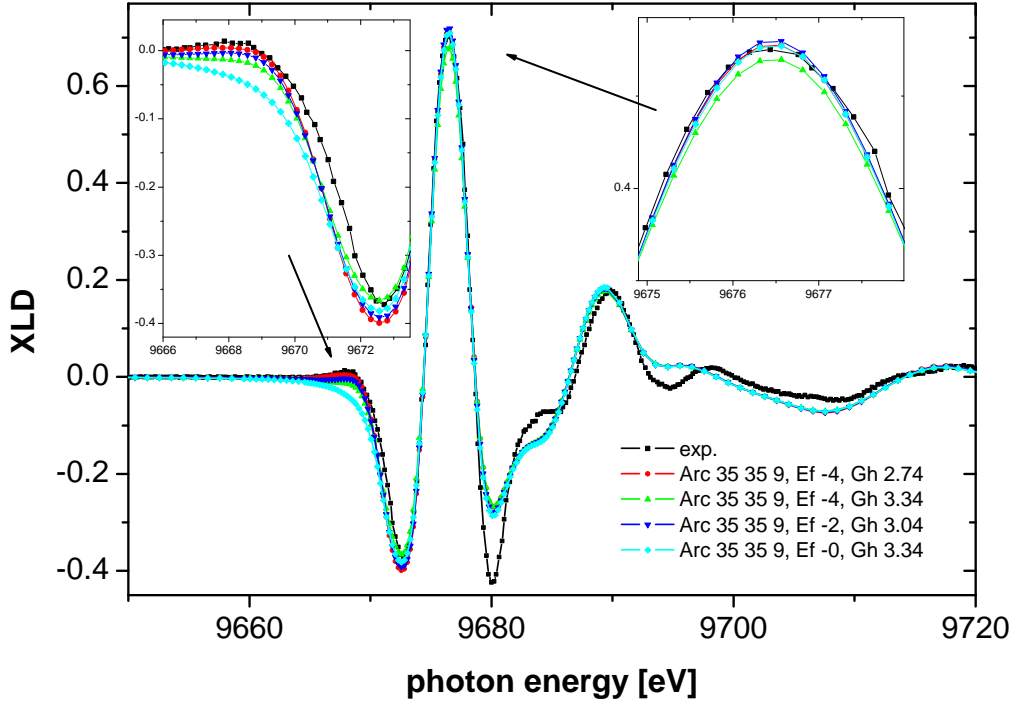


Figure 4.5: Simulated XLD spectra at the Zn K-edge convoluted with the same parameters for the energy dependent broadening of the core hole level, but with shifted FERMI level E_F and core hole width Γ_H in eV.

In order to achieve better agreement in the energy region right below the edge of the spectrum, the FERMI level was shifted in steps up to $E_F = -4$ eV. In figure 4.5 (green triangle) a simulation with shifted FERMI level, but without adjusted core hole level width Γ_H is shown. It is apparent that the reproduction of the pre-edge is much better, but on the other hand all features are too much reduced. Therefore the initial core level width Γ_H was adjusted in that sense, that the level width at the FERMI level originally determined by the FDMNES code is approximately equal to the value found in literature. This adjustment is necessary because otherwise the broadening would be too strong over the whole spectrum and therefore lead to a reduction of the features as can be seen in 4.5. The new core level width obtained for our simulations was then $\Gamma_H = 2.74$ eV, which gives

rise to spectra with features of adequate amplitude, without suppressing the first features due to the shifted FERMI level.

Having adjusted the convolution parameters for the simulation itself in order to obtain the best agreement with the experiment one can also question, whether the parameters used for the ZnO lattice are correct. One of those lattice parameters is the u-parameter, which describes the shift between the oxygen and the zinc sublattice along the c-axis. For illustration a schematic of ZnO is depicted in figure 4.6. The value for the u-parameter found in literature is $u = 0.3817$ [51], which was rounded for our simulations to $u = 0.382$. The u-parameter for an ideal wurtzite lattice is $u = \frac{3}{8}$ or given by $\frac{uc}{a} = \left(\frac{3}{8}\right)^{1/2}$.

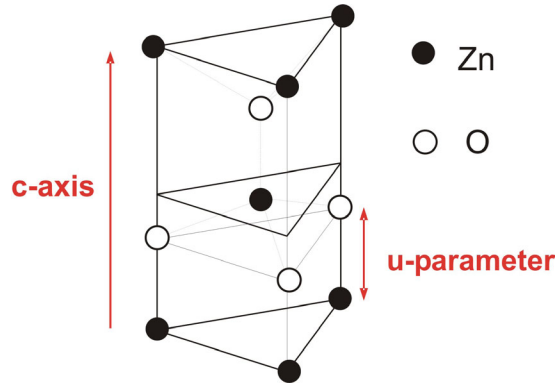


Figure 4.6: Schematic of ZnO with red arrows indicating the direction of the c-axis and the u-parameter.

In order to study the effect of a varied u-parameter on the XLD spectra, simulations were done with different u-parameters. In figure 4.7 simulations for different u-parameters are depicted. A systematic change in the spectra with slightly smaller or larger u-parameters is observable with smaller values for the XLD signal before the edge and larger values above the edge for larger u-parameters and vice versa. Hence, no improvement between simulation and experiment is achieved for an u-parameter which differs from the value $u = 0.382$ found in literature, and since the change in the spectra is systematic no further improvement is expected for a shift in u-parameter of more than 1%. Only when the u-parameter was reduced by about 0.25%, resulting in a change in the last digit of the u-parameter, a slightly better agreement with experiment was obtained. This indicates the limit of accuracy.

The spectrum in pink symbols shows strong deviations from the other spectra and one might wonder why this spectra is shown. Such simulations done with the FDMNES code with a u-parameter $u = 0.345$ are found for ZnO in literature by KUZMIN *et al.* [73]. The corresponding ZnO crystal structure with $u = 0.345$ is a phase existing under high pressure of about 9 hPa and therefore different

from the structure of the studied ZnO (or Co:ZnO) films. In the XANES spectra presented in literature the changes due to the altered u -parameter are not as obvious, but in the XLD spectra they are very pronounced. This indicates the sensitivity of the XLD to small changes of the lattice parameters and different crystallographic phases.

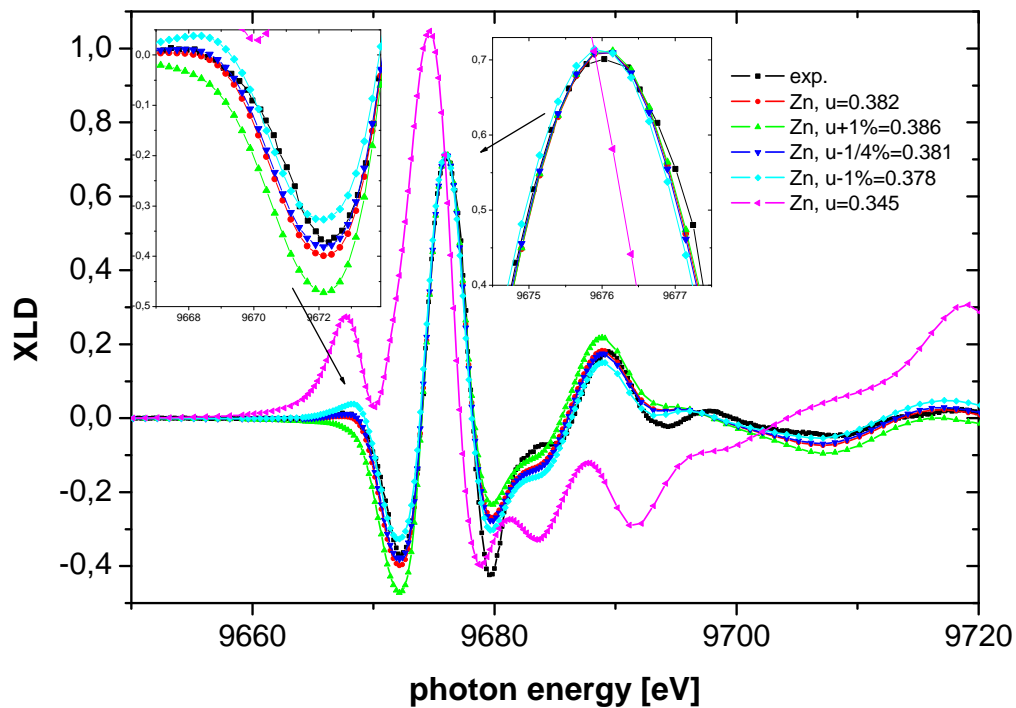


Figure 4.7: Simulated XLD spectra at the Zn K-edge for ZnO crystals with different u -parameters.

Co K-edge

Like for the Zn K-edge the XANES and XLD spectra were also simulated for the dopant atom cobalt at the Co K-edge. In figure 4.8 such a simulation of the XANES and XLD spectra with the corresponding experimental data for the PLD grown sample are depicted. The disagreement around 7730 eV again originates from the muffin-tin approximation. The maximum XLD signal is $(39 \pm 1\%)$ with respect to the edge jump.

The little bump indicated with an arrow in the experimental data for the XANES spectra in figure 4.8 is generally attributed to Co^{2+} ions and to a strong $3d4p$ hybridization with both dipolar and quadrupolar contributions. These transitions were not reproduced in the simulated spectra since the energy position is well below the determined FERMI level from the FDMNES code. With a relative shift of the FERMI energy of $E_F = -7$ eV it seems that this pre-edge feature can be obtained in the simulation, however further investigation is required.

The parameters for the simulations of the spectra at the Co K-edge were adopted from the simulations for the Zn K-edge. The only modification done for the convolution of the spectra was an adjustment of the core hole level width Γ_H , which is given in literature to be $\Gamma_H=2.66$ eV for cobalt [72]. As for the core hole level width for Zn an equivalent adjustment concerning the energy dependent broadening of the final levels and the shifted FERMI level E_F was done. This adjustment resulted in a core level width of $\Gamma_H=2.16$ eV for the simulations. All other simulation parameters were not changed in order to get a consistent set of simulation data for Co:ZnO.

As one can see in figure 4.8 the agreement between the simulated spectrum and the experimental one is not as good for the Co K-edge as it was for the Zn K-edge. Apparently, the energy-dependent broadening for Co should be larger compared to the Zn to reduce the peaks of the XLD at higher energies. Since there is no obvious physical reason to alter the convolution parameters the explanation might also be, that the Co atoms in ZnO do not ideally occupy the Zn lattice positions or form pairs or clusters of Co atoms on Zn lattice sites.

In order to find out, if the agreement between the experimental data and the simulation is improved for different configurations of Co atoms in the ZnO host crystal simulations were performed with the position of the Co atoms shifted along the c-axis. A schematic of the Co:ZnO can be seen in figure 4.9. A series of simulations was also performed with a shift of the dopant atom perpendicular to the c-axis. However, as no further improvement between simulation and experiment was achieved the results are not discussed here. In figure 4.10 only the spectra for the Co shifted 1% up or downwards in the ZnO lattice along the c-axis are shown, however in the upper diagramm the amplitudes of the different peaks in the XLD spectra are plotted over the shift of the Co atom along the c-axis for simulations with a shift of the Co atom of up to $\pm 5\%$. It is shown in the upper graph of figure 4.10 that even for a shift of $\pm 5\%$ the changes in the spectra

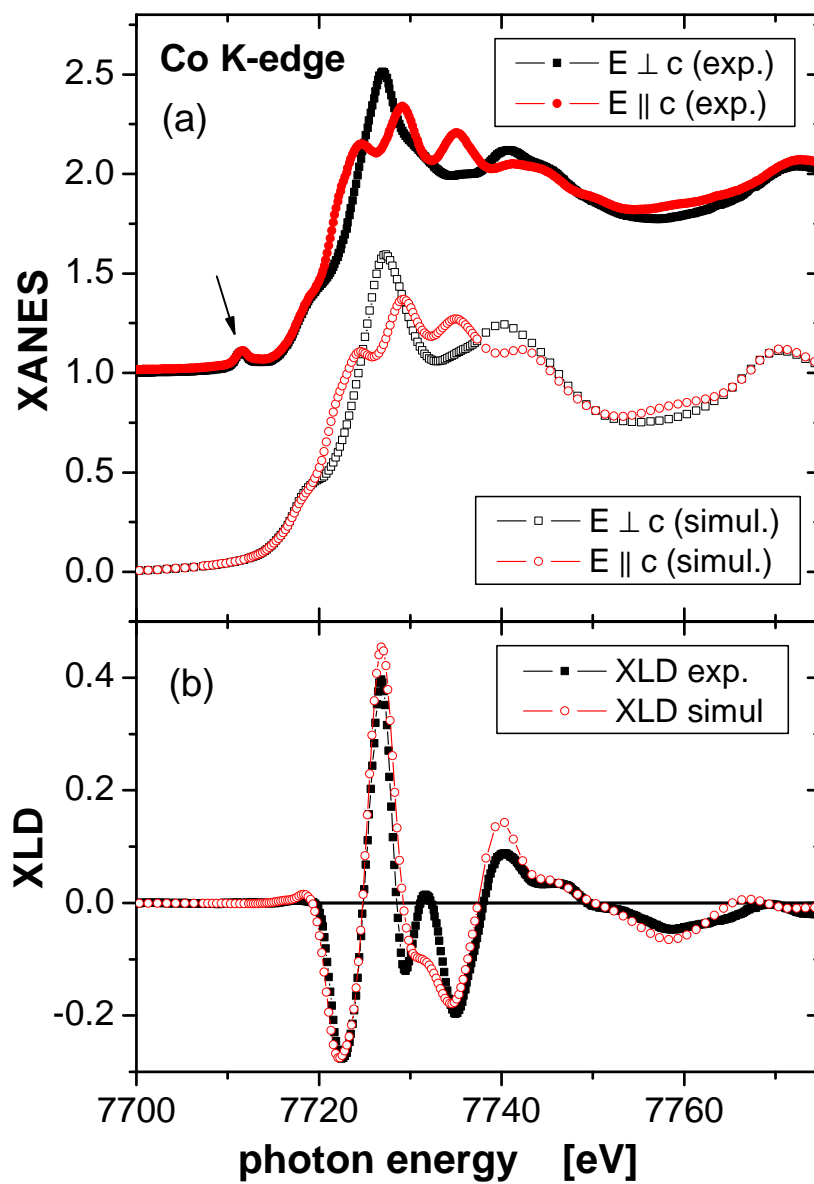


Figure 4.8: Experimental and simulated XANES and XLD spectra for Co:ZnO at the Co K-edge (Note that the experimental XANES spectra are vertically shifted for better visibility).

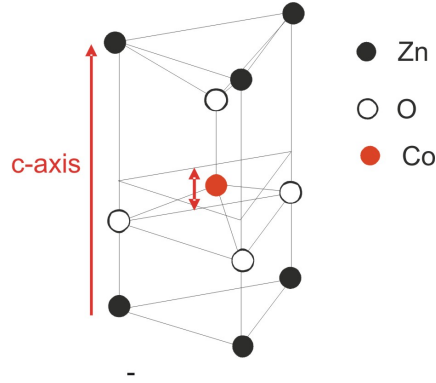


Figure 4.9: Schematic of Co:ZnO with red arrows indicating the direction of the c-axis and the shift of the Co atom along the c-axis.

are systematic and therefore also a larger shift is not likely to improve the agreement with the experimental spectrum further. The horizontal lines represent the peak amplitudes of the experimental spectrum (in the same color coding as for the peak amplitudes for the simulated spectra). From the spectra simulated for the shifted Co dopant position in the ZnO matrix it can easily be seen in figure 4.10, that the agreement is not improved for shifted Co atoms. Therefore it can be assumed that the Co atoms occupy the by less than 1% disturbed Zn lattice places.

In order to study the influence of non-isolated Co in ZnO on the XLD spectra, simulations were performed with different configurations of Co in the ZnO lattice. In figure 4.11 simulated XLD spectra for Co-O-Co pairs (with Co on Zn lattice sites) in different orientations in the wurtzite crystal are shown. A schematic representation of the different pair configurations is depicted in figure 4.11 top. Only very small changes in the simulated XLD spectra for the different pair configurations are visible compared to the simulations done with an isolated substitutional Co. Only for pair three the simulated XLD spectrum is slightly different at higher photon energies. An explanation could be that pair three forms a chain of Co-O-Co through the whole crystal. In order to study the effect of the periodicity of the Co in ZnO introduced by the size of the cell used for simulation, a supercell of three by three by three ($3 \times 3 \times 3$) times the unit cell was also used for simulations for comparison (not shown). However, no significant changes were observable. *Therefore the XLD spectrum does not allow to conclude, whether Co atoms are likely to have a Co nearest (cation) neighbor or if they are isolated in the crystal.*

XLD spectra from simulations carried out with Co on O lattice sites (antisites) are depicted in figure 4.12. Clear changes with respect to the XLD spectrum for substitutional Co on Zn lattice sites are visible with a completely different XLD signature for Co on antisites. Almost an anti-correlated spectral shape is found

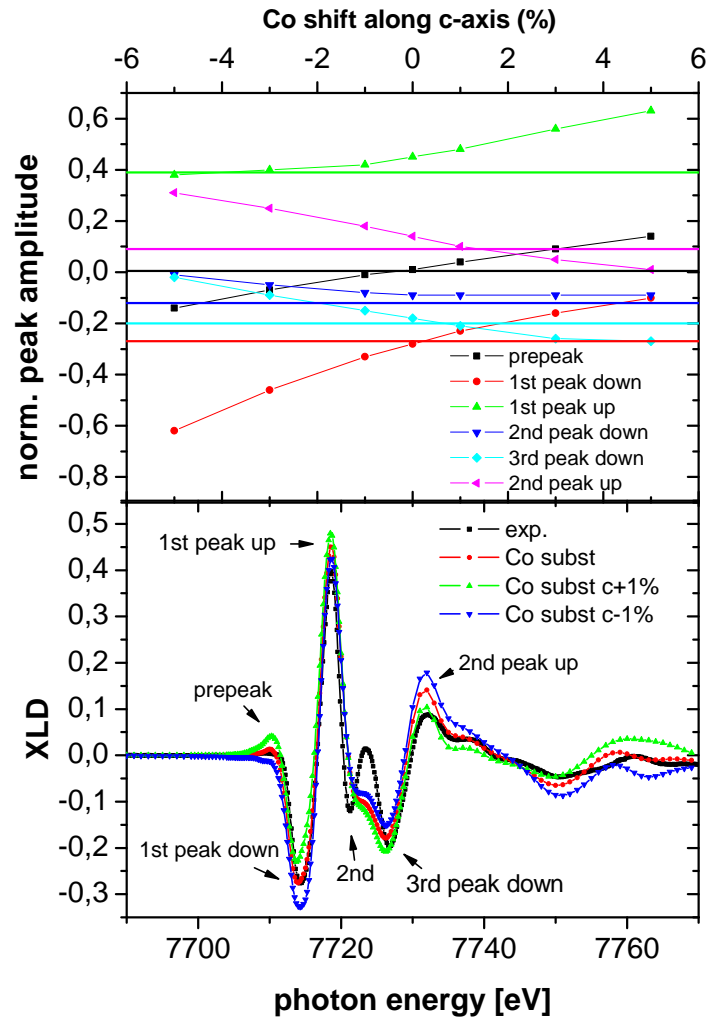


Figure 4.10: Bottom: Simulated XLD spectra for Co:ZnO with different positions of the Co dopant atom along the c-axis in the ZnO crystal.

Top: Peak intensity of the various peaks in the XLD spectra plotted over the shift of the Co atom along the c-axis. The horizontal lines represent the experimental values for the peak amplitude (with the same color coding).

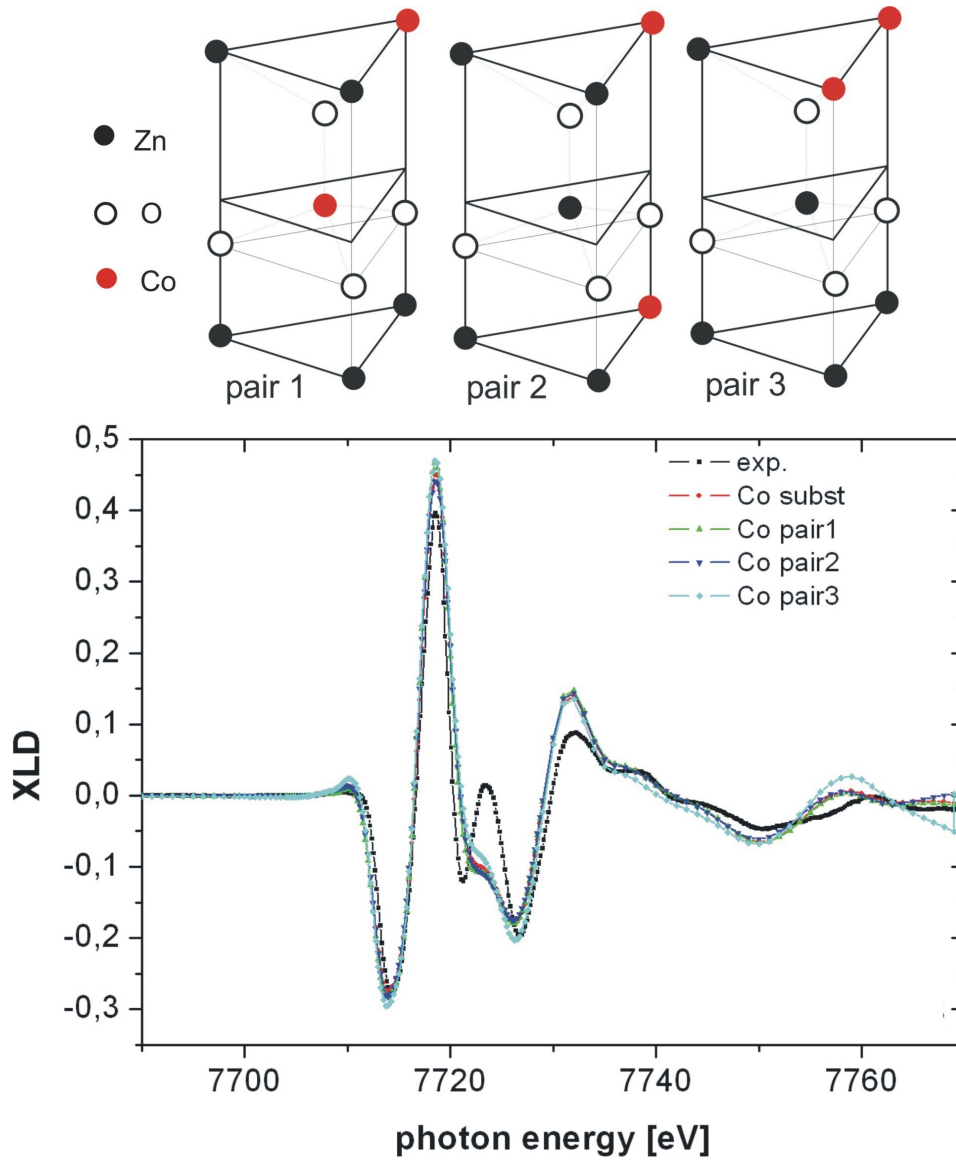


Figure 4.11: Simulated XLD spectra at the Co K-edge for a Co:ZnO crystal with different configurations for the Co on Zn lattice sites. Top: Schematic of Co-O-Co pairs in different configurations.

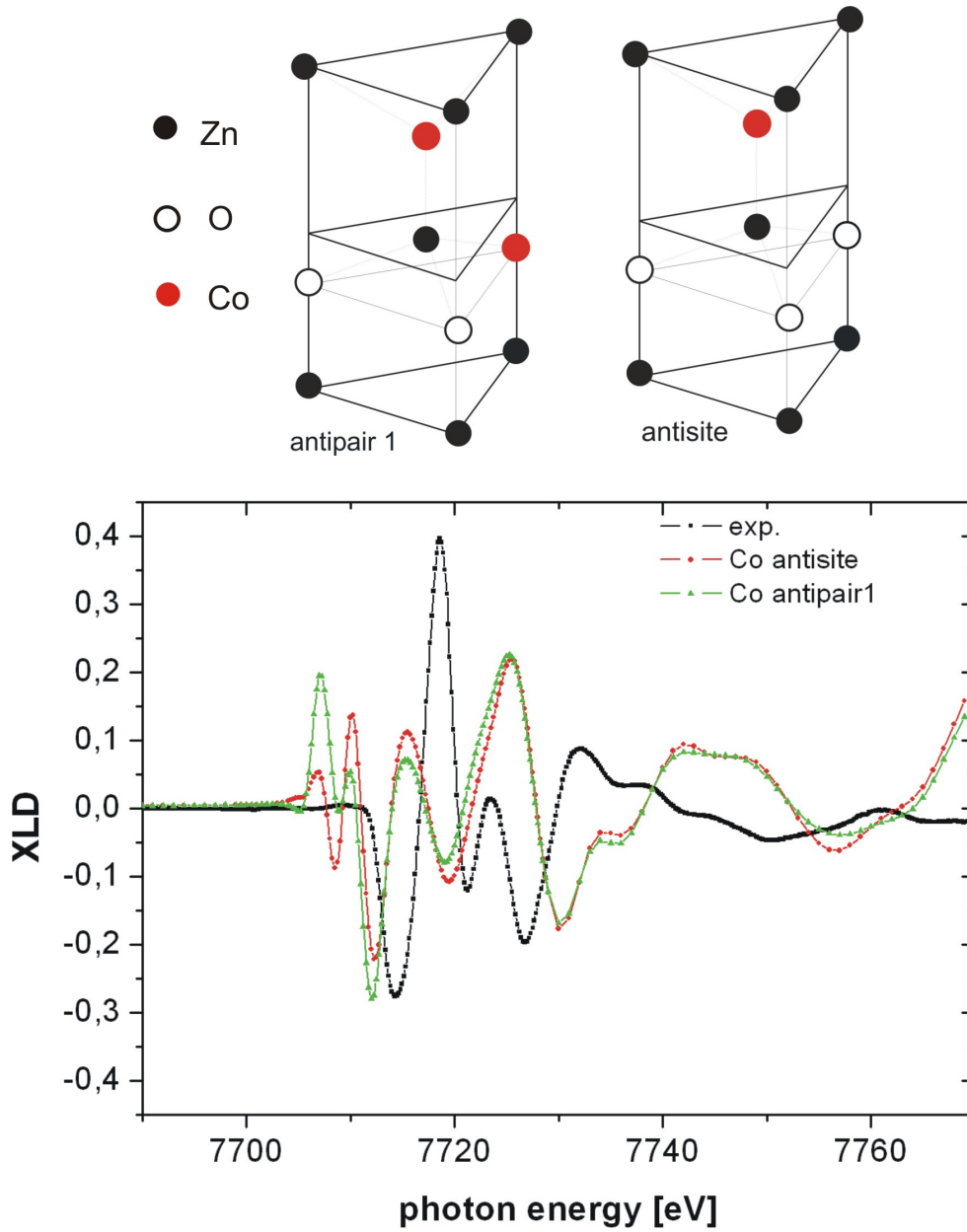


Figure 4.12: Simulated XLD spectra at the Co K-edge for a Co:ZnO crystal with different configurations for the Co on O lattice sites (antisites) with one isolated Co antisite and a Co-Zn-Co antipair. Top: Schematic of the Co positions for the pair and antipair.

for both isolated Co and paired Co on O lattice places with a significant increase in XLD signal at and below the Co edge. This finding corroborates the fact, that for the samples with good structural properties the Co in the ZnO lattice most likely occupies Zn lattice sites, and antisite disorder is unlikely for it would result in a completely different XLD signature.

In addition to simulations with Co on either Zn or O lattice sites, also clusters of Co were studied with direct Co-Co neighbors. A schematic of the different configurations of neighboring Co in ZnO is shown on the top in figure 4.13. Simulated XLD spectra at the Co K-edge for the different cluster configuration are shown in figure 4.13. As one can see, the XLD signatures for the different clusters are very different from the spectra for substitutional Co and also each individual cluster configuration results in an individual XLD signature. The most significant change for the spectra is the XLD signal at and below the Co edge which is visible for most of the cluster configurations and might indicate the more metallic nature for Co clusters in the ZnO lattice.

In addition to the XLD spectra for Co configurations in ZnO shown here, more simulations have been performed for other configurations (not shown), however with similar results, that is an individual XLD signature for each individual cluster configuration. Such an individual XLD signature would only be detectable in a real experiment, if only one of these cluster types is dominating in a sample. Furthermore the formation of Co clusters is likely not to take place by filling substitutional lattice sites of the ZnO crystal, but by formation of secondary phases, which again can have a different crystallographic structure and different orientations with respect to the c-axis of the ZnO wurtzite lattice.

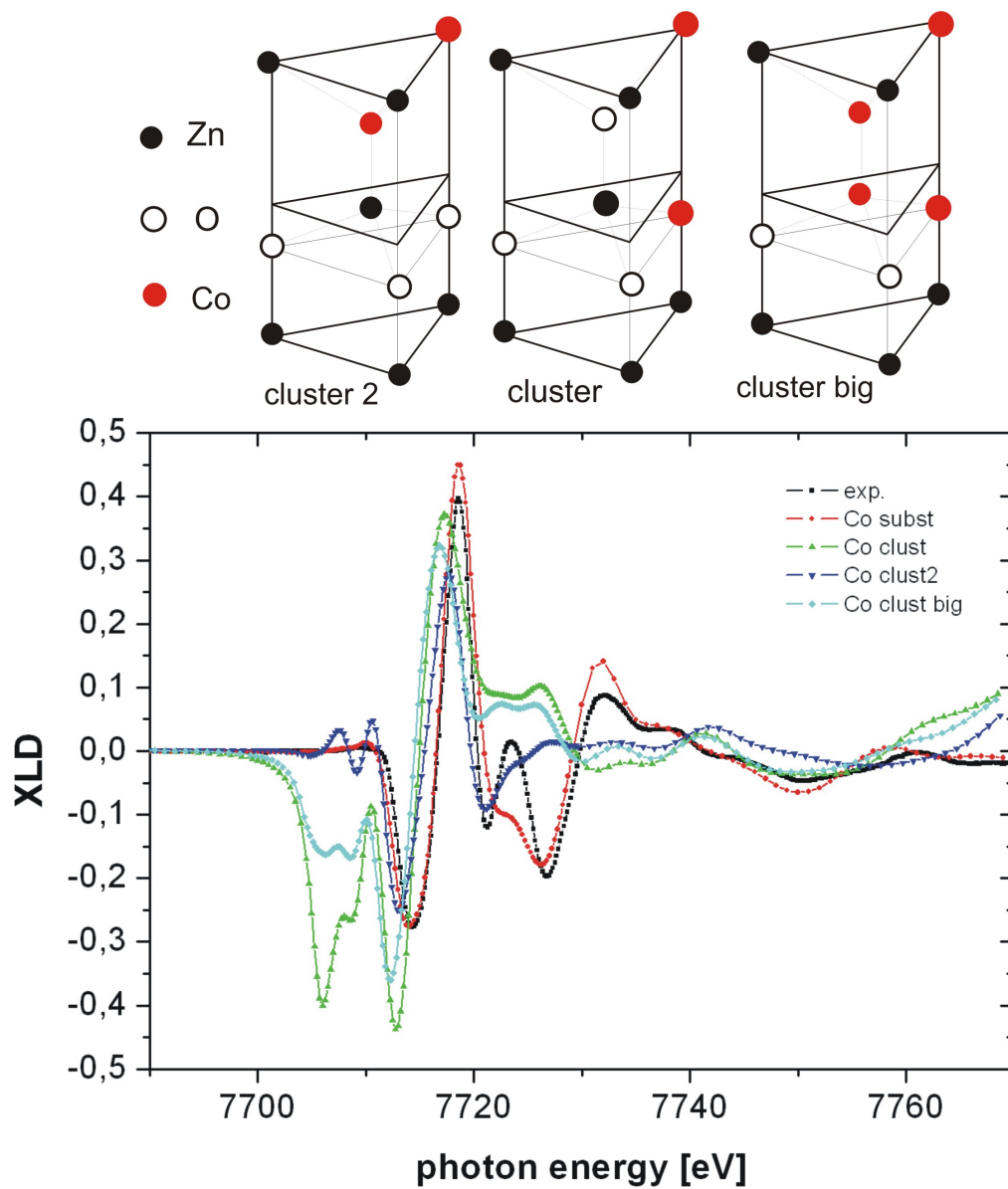


Figure 4.13: Simulated XLD spectra at the Co K-edge for different Co clusters. On top the different cluster configurations are depicted.

4.1.2 Experimental Evidence for Clustering

In the XLD simulations for the Co K-edge one can observe changes in the spectral shape of the XLD spectra for pairs (figure 4.11) or clusters (figure 4.13) of Co, which occupy Zn lattice places. In reality, however, this is not necessarily the case. Co clusters in ZnO might have a different structure and therefore have a different XLD signature or no XLD signature at all. Eventhough the signatures of Co clusters in ZnO are visible in the simulated XLD spectra, in the experimental data they are only visible due to an overall reduction of the peak intensities, no additional features were observed. In figure 4.14 experimental XANES and XLD spectra are shown. The XANES and XLD spectra of a sample with excellent structural properties (black squares), where Co is substitutional on Zn lattice places, is compared with the spectra of a sample in which clusters of cobalt atoms are observed (red triangles) (e.g. indicated by superparamagnetic blocking behavior in figure 4.19). The reduction of the XLD signal over the whole energy range is obvious for the clustered sample (red triangles in 4.14). However, no additional features or dramatic changes in the relative peak intensities are observed.

The reduction of the XLD signal might have several causes. In the case of Co atoms on random interstitial sites in the ZnO lattice the XLD signatures of all Co atoms would average out and hence give no rise to an XLD signal. Also Co atoms in a cubic environment do not contribute to the XLD signal. Even for Co in a hexagonal structure no XLD signal arises if the c-axis is randomly oriented.

In the XANES spectra one significant difference can be seen (see inset in figure 4.14). A pre-edge peak can be seen for the sample with substitutional cobalt, which is characteristic for the Co substituted into ZnO as Co^{2+} ions on Zn lattice sites [74]. This pre-edge feature is generally attributed to the $1s \rightarrow 3d4p$ transition of Co^{2+} . In the XANES spectrum of the clustered sample this feature is less pronounced indicating the presence of metallic cobalt in the sample, as metallic Co has a distinct broader K-edge absorption feature as for example shown in [75].

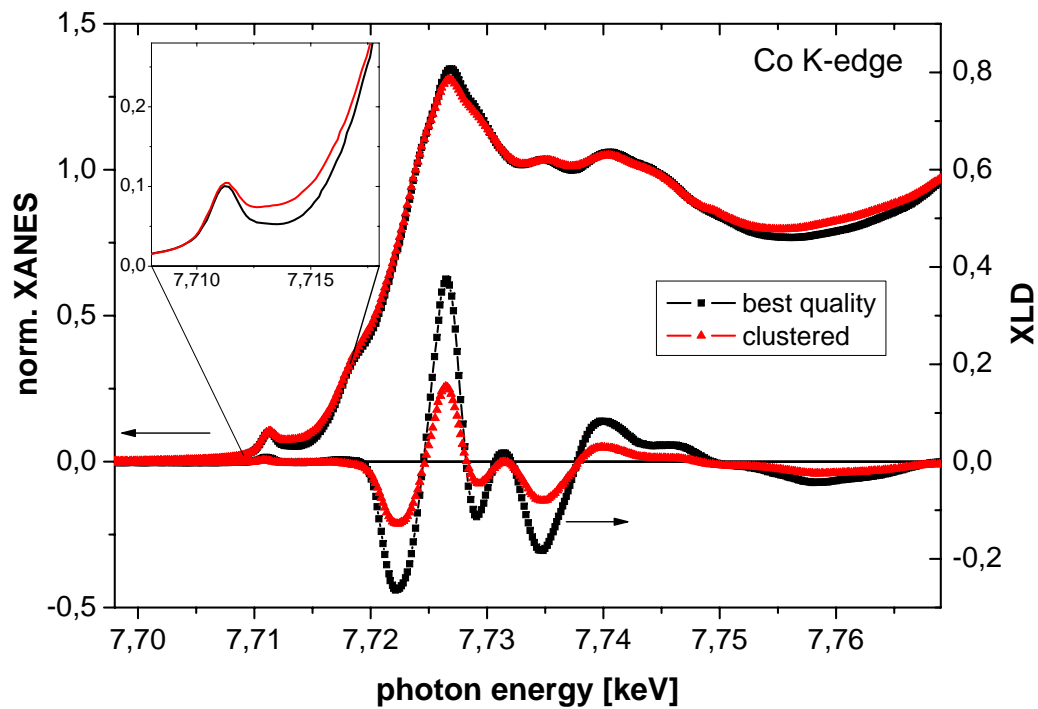


Figure 4.14: Experimental XANES and XLD spectra recorded at the Co K-edge (at $T = 300\text{ K}$) for a sample with Co clusters (red triangles) and one sample with good structural properties (no detectable clustering) (black squares). Inset: Magnification of the pre-edge region of the XANES spectra, where a peak known from Co^{2+} can be seen for the "best quality" sample. For the other film this feature is less pronounced indicating metallic clusters.

4.2 Magnetic Properties of Co:ZnO

In addition to the crystalline structure of Co doped ZnO samples also the magnetic properties were investigated using both integral SQUID magnetometry and elementspecific XMCD.

Elementspecific XMCD

The XMCD of the PLD grown sample with excellent structural quality (see above figure 4.2 and 4.8) was measured at beamline ID12 at the ESRF in Grenoble.

The knowledge about the structural properties of the samples is vital in order to distinguish between origins of ferromagnetic signatures found in DMS materials, which are intrinsic and the ones stemming from secondary phases and metallic clusters. As the elementspecific analysis with XLD has shown that the PLD grown sample of Co doped ZnO has excellent structural properties with more than 95% of the Co atoms occupying Zn lattice places the magnetic behavior can be assumed to stem from the intrinsic Co:ZnO.

In figure 4.15 the XANES (black) and XMCD (red) spectra recorded at the Co K-edge are shown. For the XMCD spectra in figure 4.15 a magnetic field of ± 6 T was applied by a superconducting magnet. The sample temperature was kept at $T=6.7$ K during the measurements. In order to minimize artefacts not only the field was reversed, but also the helicity of the x-rays. The pre-edge feature is again clearly visible, which is typical for Co^{2+} . XMCD at the K-edge, which is a measure for the orbital fraction of the moment per Co atom is detected at the pre-edge feature as well as at the main peak. The maximum XMCD value of 0.3% is obtained at the pre-edge. This is the largest value found for 10% Co:ZnO so far [76] and therefore, since the XMCD is a measure for the average magnetic moment of Co, indicates a very good structure of the sample in agreement with XLD. The magnetic moment for cobalt is larger in reduced dimensions, e.g. for Co^{2+} impurities the experimental magnetic moment is typically $\langle \mu_z \rangle = 4.1\mu_B$ (corresponding to an experimental effective magneton number of $p = 4.8\mu_B$) whereas for metallic Co (hexagonal bulk) it is $\langle \mu_z \rangle = 1.72\mu_B$ [8]. Hence the cobalt is likely to be present as Co^{2+} ions in the ZnO matrix and not as metallic cobalt clusters. Note, that from Hund's rules for Co^{2+} ($3d^7$) with equation 1.10 one would yield an effective magnon number $p = 6.63\mu_B$ ($S = 3/2$ and $L = 3$), however for the Co^{2+} impurities the orbital moment is partly quenched due to the symmetry of the surrounding atoms.

For the $M(H)$ curves depicted in figure 4.16, which are the XMCD signal measured at the photon energy of the Co K-pre-edge for a sample temperature $T=6.7$ K and $T=40.5$ K, no remanence or opening of a hysteresis are visible within the noise level. This indicates purely paramagnetic behavior. The field dependence of the main and the pre-edge XMCD peaks is the same, however with opposite sign.

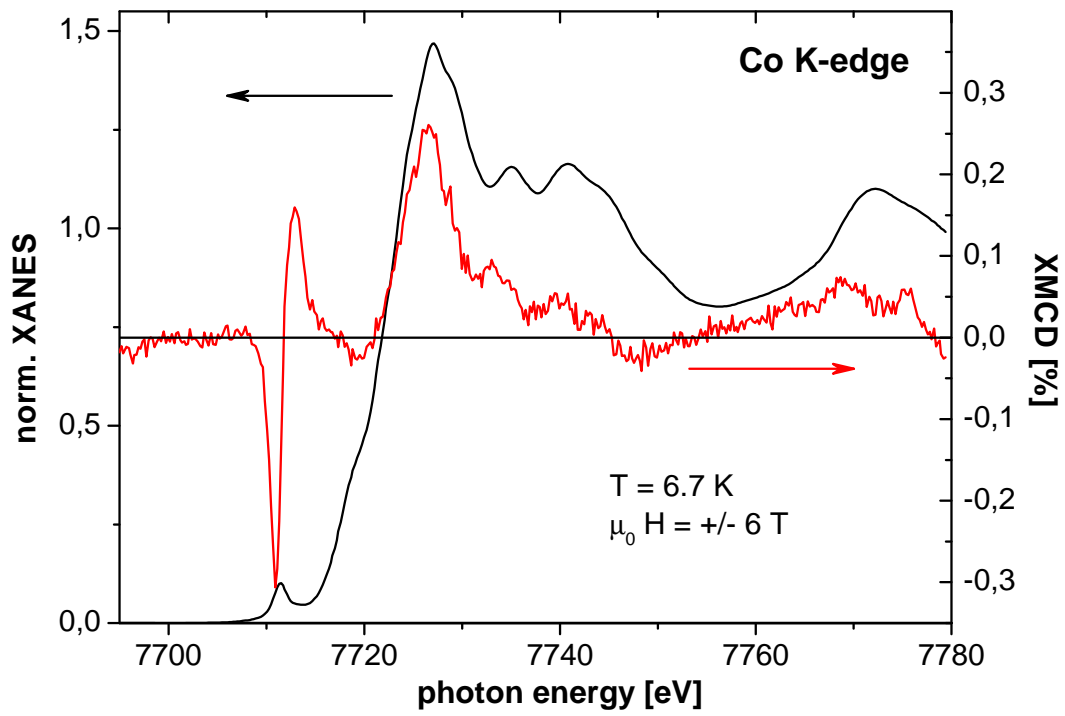


Figure 4.15: XANES and XMCD spectra recorded at the Co K-edge for an high quality PLD grown Co:ZnO sample.

In order to yield a more quantitative understanding of the field dependence $M(H)$ Brillouin functions as described in equations 1.5 and 1.6 were fitted using $S=3/2$ and $L=3$ as well as $S=3/2$ and $L=1.07$ yielding a magnetic moment of Co^{2+} of $4.1\mu_B$ per Co^{2+} ion and the same value of $L/S=0.7$ as in reference [71]. The only adjustment to the calculation was to normalize the value at saturation. The slightly better agreement between the fit with $L=1.07$ and the experimental data is not significant; however, it indicates that the Co atoms have a magnetic moment of $(4 \pm 1)\mu_B$.

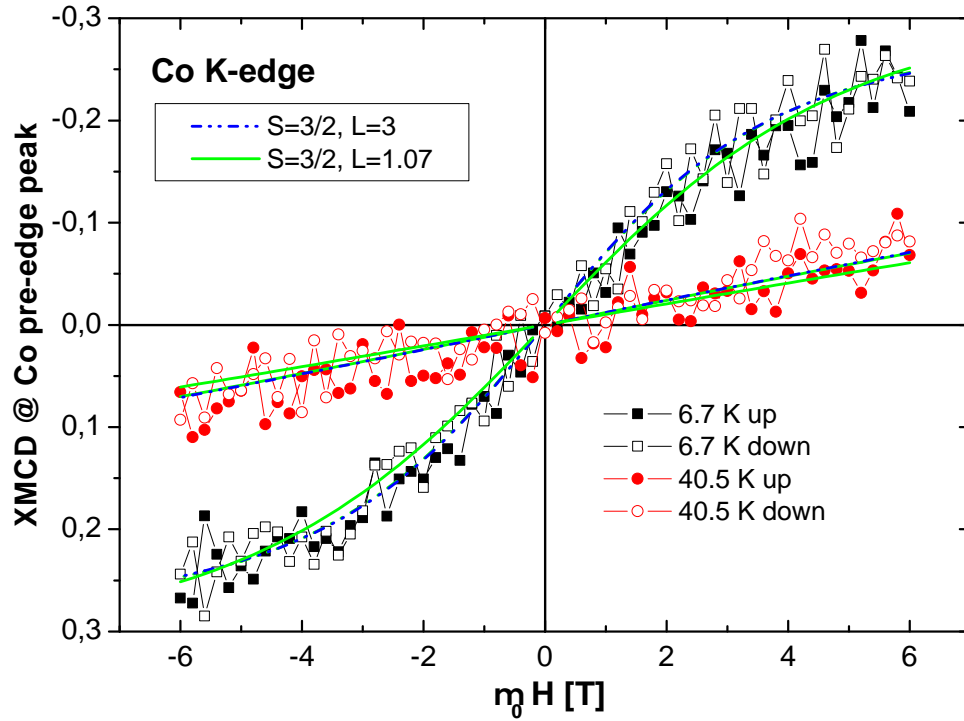


Figure 4.16: Two $M(H)$ curves recorded at the photon energy of the Co pre-edge XMCD feature at 6.7 K (squares) and at 40.5 K (circles) together with fitted Brillouin functions.

Integral SQUID

Figure 4.17 shows SQUID measurements for the same PLD grown sample as was used in figure 4.16 for a sample temperature of $T=300\text{ K}$ and $T=5\text{ K}$. No opening of a magnetic hysteresis was detected at 300 K contrary to a previous study on

sputtered Co:ZnO [71]. The diamagnetic background of $2.189 \cdot 10^{-10} \text{ Am}^2/\text{mT}$ was derived from the high-field magnetization data at 300 K and subtracted from both data sets. At 5 K a clear paramagnetic signal can be seen after the same diamagnetic background is subtracted. In the inset of figure 4.17 the temperature dependence $M(T)$ of the magnetization is shown for the zero field cooled (ZFC), that is no magnetic field is applied during the cool down of the sample, and the field cooled (FC) case, that is the sample is cooled in a magnetic field of 5 T. The magnetization of the samples is measured while warming up in a magnetic field of 10 mT. No separation of the FC and ZFC curves is visible corroborating purely paramagnetic behavior.

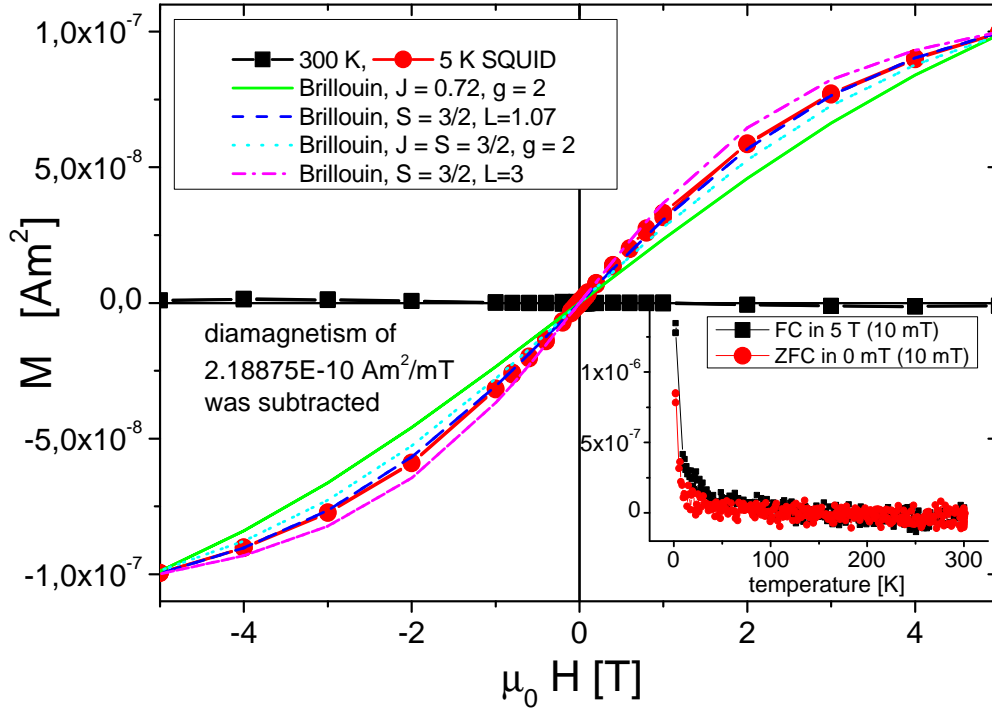


Figure 4.17: SQUID $M(H)$ curves of Co:ZnO at 5 K and 300 K including fits using Brillouin functions for $L = 3$ (pink dashed line), $J = 0.72$ (green line), $L = 1.07$ (blue dashed line) and $J = S = 3/2$. Inset: Field cooled versus zero field cooled curves at 10 mT corroborating paramagnetic behavior.

As with the XMCD hysteresis, the SQUID data can be fitted well with the Brillouin function for $L = 1.07$, whereas the fit for $L = 3$ is not as good. For fit with the Brillouin function with only spin and $L = 0$ ($S = J = 3/2, g = 2$) the

curvature of the field dependence of the magnetization is not sufficient to fit the experimental data.

From various fits of the SQUID loop it can be concluded that the signal is caused by Co atoms with a moment $S=3/2$ and $L \approx 1$, which compares well with the representative value for isolated Co^{2+} [8].

Abundance of Dopant Configurations

So far the magnetic moment of the Co ions has been derived from the curvature of the $M(H)$ loop. By taking into account the sample volume and dopant concentration, the expected overall magnetization for a magnetic moment of $\langle \mu_z \rangle = (4.1 \pm 0.1)\mu_B$ per Co can be calculated. This calculation yields a saturation magnetization of $(4.6 \pm 0.4) \cdot 10^{-7} \text{Am}^2$ which results in $(3.6 \pm 0.3) \cdot 10^{-7} \text{Am}^2$ after correcting the SQUID measurement conditions (5 K and 5 T).

In contrast, the SQUID measurements reveal only $1 \cdot 10^{-7} \text{Am}^2$ which is only $(28 \pm 3)\%$ the magnetization expected from the full moment, i.e., only $\langle \mu_z \rangle = 1.2\mu_B$ per Co effectively which would result in a linear $M(H)$ curve at 5 K (see green line in figure 4.17) in disagreement with both XMCD and SQUID results shown in figure 4.16 and figure 4.17.

To explain this discrepancy, the abundance of Co dopants on Zn substitutional sites in various clustered configurations was considered using BEHRINGER's equations for the hcp lattice [77]. The wurtzite lattice consists of two hexagonal close packed lattices of cations and anions, which are shifted by u with respect to each other. Since Co occupies Zn (cation) lattice sites and not the O (anion) sites BEHRINGER's equations for the hexagonal lattice are applicable.

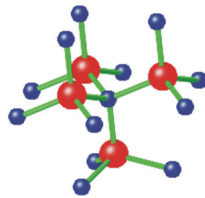


Figure 4.18: Illustration of a small wurtzite cluster: Cation lattice site in the center and the $m=12$ nearest neighbor cation sites.

For example in a wurtzite lattice, which is depicted in figure 4.18, the central atom is taken to be a cobalt atom without loss of generality. Then this cobalt atom has $m = 12$ nearest cation neighbor lattice sites (equivalent to the hcp lattice in [77]) in the wurtzite crystal. With a fractional concentration of Co atoms x and the number n of Co atoms in this nearest cation neighbor shell and assuming a random distribution of Co atoms in the lattice, the probability P is given by the binominal distribution:

$$P(X, N) = \frac{m!}{n!(m-n)!} x^n (1-x)^{m-n} \tag{4.2}$$

For a single Co atom no other Co atom is allowed to be in the nearest cation-neighbor shell and all 12 nearest cation atoms must be Zn atoms, therefore $n = 0$. The probability for each of these lattice sites to be occupied by a Zn atom is given by equation 4.2 with $m = 12$ and $n = 0$ leading to $(1-x)^{12}$.

In BEHRIGER's equations [77] the numbers of single atoms of one kind (Co in our case) S (single) and Co-O-Co pairs D (dimer) etc. in a hexagonal lattice are given by:

$$S = N \cdot x \cdot (1-x)^{12} \tag{4.3}$$

$$D = 12 \cdot N \cdot x^2 \cdot (1-x)^{18} \tag{4.4}$$

where N is the number of lattice sites. If the foregoing equations are divided by $N \cdot x$ one receives the probability that a given atom is in a single, double configuration. For a Co mole fraction of $x = 0.1$, and assuming a random dopant distribution, the probabilities that a given Co dopant will have $n = 0, 1, 2$ other Co ions as nearest cation neighbors (i.e., isolated Co, Co-O-Co pairs, and triples) are given in the first two columns of Table 4.1. With some approximations the abundance of Co quadruples ($n = 3$) could also be estimated. Table 4.1 also shows four models assuming different effective magnetic moments per Co atom for the various configurations to calculate the effective fraction of the full moments.

Table 4.1: Apparent reduction of the full magnetic moment per dopant for the wurtzite structure.

No. of cation neighbors	abundance	case A μ_B/Co	case B μ_B/Co	case C μ_B/Co	case D μ_B/Co
n=0 (single)	28.2%	4.1	4.1	4.1	4.1
n=1 (pair)	18.0%	0	0	0	0
n=2 (triple)	11.6%	1.4	1.4	0	0
n=3 (quadruple)	≈8%	2.1	0	2.1	0
fraction of full moment		36.1%	32.1%	32.2%	28.2%

Here only collinear configurations of the moments are considered. Furthermore Co in Co-O-Co is considered to couple antiferromagnetically as discussed recently in [78]. A parallel alignment of the moments of pairs would yield $28.2 + 18.0 = 46.2\%$ of the expected magnetization, which is inconsistent with the SQUID data.

All antiparallel triple configurations have an effective net magnetic moment of $1.4\mu_B$ per dopant atom (one up and two down, represented by case A and B in table 4.1).

For quadruples also the partially compensated case with three up and one down was considered leading to $2.1\mu_B$ effectively per Co atom. However, since the pairs are supposed to be compensating each other this should also hold for the quadruples, indicating an unlikelyness of case A and case B.

Obviously, the reduction of the magnetization by 28% as measured by SQUID can be readily explained by antiferromagnetic alignment for Co-O-Co pairs and negligible contributions of Co in triples to the magnetic moment (i.e., case D in Table 4.1).

Within the accuracy of the measurement only case B cannot be fully excluded. This indicates, that either triples form less frequently as expected from a purely statistical model, or that noncollinear configurations with an effective moment of about $1\mu_B$ have to be taken into account in order to be consistent with the reduced effective moment.

Cluster

In order to study the role of cobalt clusters in Co doped ZnO, which is also discussed in literature [79] the growth parameters (Ar:O ratio) for the magnetron sputtered Co:ZnO films were varied from Ar:O=10:1 to Ar:O=10:0.5 with structural properties varying from excellent crystallographic structure to clustered Co in ZnO. The film with the best structural properties and the clustered film were studied with XLD and are shown in figure 4.14 with the clustered film yielding a significantly reduced XLD signal. Note, that for the structural and magnetic properties of the sputtered Co:ZnO sample with excellent structural properties similar results were obtained as for the PLD grown sample with both XLD (see figure 4.1), SQUID and XMCD (not shown).

In figure 4.19 the FC and ZFC curves for the differently grown samples from substitutional cobalt to cobalt clusters can be seen displaying a magnetic behavior from an ideal paramagnet to a superparamagnetic ensemble. For the film grown with an Ar-to-O₂ ratio of 10 to 1.0 no separation of the FC and ZFC curves is visible in agreement with the results for the PLD grown sample (figure 4.17). With a reduced O₂ ratio a separation between the curves is visible. For the sample grown with Ar:O₂=10:0.6 a blocking behavior at low temperature can be observed indicating small metallic clusters. The structural characterization showed a significantly reduced XLD signal for this sample (figure 4.14). For a further reduced O₂ partial pressure the separation of FC and ZFC curves becomes even more pronounced and the blocking temperature is shifted to higher temperatures. Only for Ar:O₂=10:0.5 the Co clusters could be detected with XRD which again highlights at the high sensitivity of XLD to detect secondary phases.

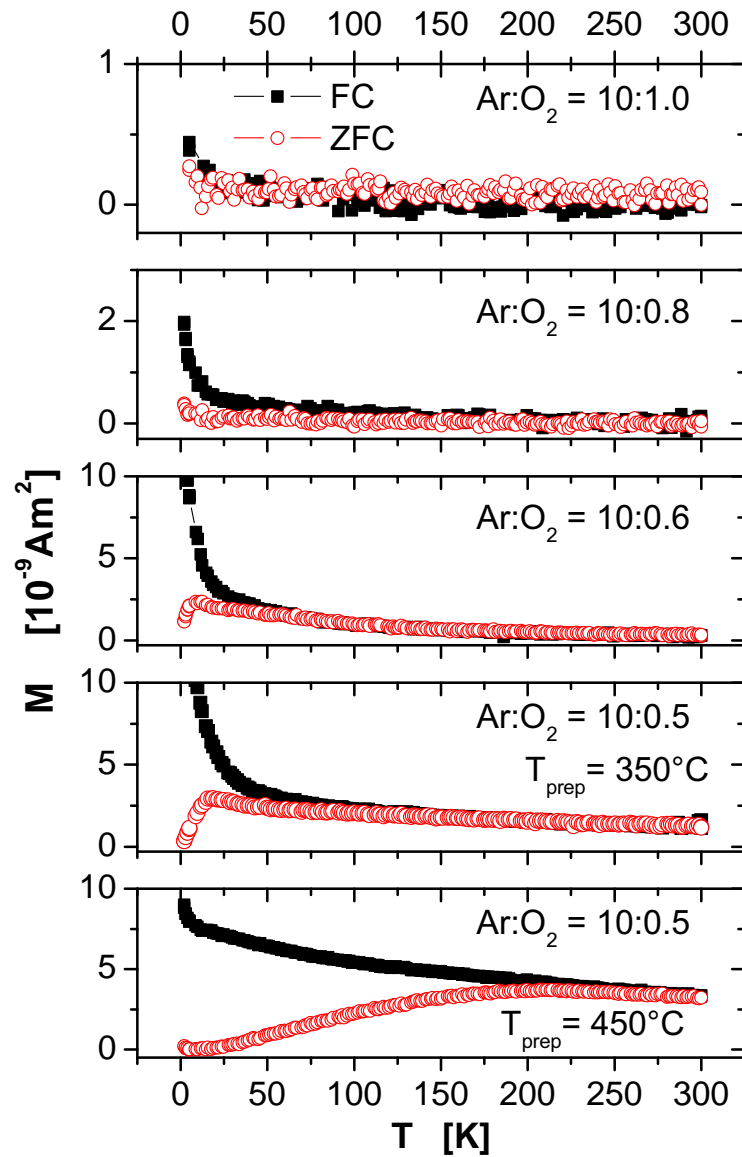


Figure 4.19: FC and ZFC curves for sputtered Co:ZnO films with different growth parameters: From the best quality sample (top) to a clustered film (bottom) the onset of superparamagnetic behavior is visible.

In conclusion, XLD and XRD have been used to show, that the Co doped ZnO studied here had excellent structural properties with the Co dopant on substitutional Zn lattice sites and a ZnO matrix, which is undisturbed by the incorporated Co dopant atoms. In addition both elementspecific XMCD and integral SQUID have been utilized to demonstrate, that these Co dopants in compositionally well-defined $\text{Co}_{0.1}\text{Zn}_{0.9}\text{O}$ behave purely paramagnetically with an effective moment $\langle \mu_z \rangle = 4.1\mu_B$ for the isolated Co atoms (corresponding to an effective magneton number of $4.8\mu_B$) which is well established. A considerably reduced effective moment and thus magnetization was observed due to the formation of Co-O-Co pair configurations coupling antiferromagnetically and are in turn a natural consequence of a stochastic dopant distribution.

Hence, no experimental evidence for intrinsic ferromagnetic interactions neither for isolated nor for paired Co dopants was found in high-quality Co doped ZnO. However, superparamagnetic behavior is found for Co doped ZnO films with structural quality leading to the formation of Co clusters.

Chapter 5

Imaging of Nanocubes

Nanoparticles are of great interest due to their numerous possible applications, where they function as, e.g. ideal nanoscale bit structures of future ultrahigh-capacity storage media [6]. In order to utilize those nanoparticles their physical properties have to be well-known. Therefore both structural and magnetic properties have been subject to intensive studies. However, in contrast to the structure of the nanoparticles, which can be investigated up to atomic resolution, e.g. using HR-TEM [80], magnetic measurements of single particles remain challenging. Well established techniques for magnetic characterization like FMR (ferromagnetic resonance), SQUID and XMCD all yield an integrated signal for the particle ensemble. Yet the magnetic properties of individual particles may be quite different due to their individual size or shape and their relative orientation towards each other and an applied magnetic field and therefore the influence of differently oriented magnetocrystalline anisotropy axes, different sizes and different shape anisotropies due to various configurations of interacting particles cannot be deduced from these ensemble averaged results in a straightforward manner. Efforts to overcome these limitations have been made with, e.g. MFM (magnetic force microscopy) [81] or embedding single particles in the superconducting loop of a custom-made microscopic SQUID [82]. A very recent approach is the use of x-ray spectro-microscopy in order to study both electronic and magnetic properties of the particles with spatial resolution, e.g. by x-ray photoemission electron microscopy (XPEEM) [83].

For this work synchrotron radiation was used to study Fe/Fe_xO_y nanoparticles. The utilization of x-rays for imaging also allows elementspecific studies of the properties of the individual particles or small configurations of particles as energy- and polarization-dependent absorption of the x-rays is employed as a contrast mechanism. Two different techniques were used, namely XPEEM for quasi-static measurements and lensless imaging (FOURIERtransform holography) which promises also time dependent studies in the future.

5.1 Magnetic Imaging of Nanocubes with XPEEM

In order to study single nanoparticles with x-rays the XPEEM at BESSY was utilized. In order to be able to apply a magnetic field during the measurements a special sample holder (see chapter 2.2.2) was used, which enables to generate an inplane magnetic field locally confined so that the imaging process is not disturbed by deflection of the electrons. Magnetic imaging with XPEEM is possible due to the XMCD effect. The difference between images taken at negative helicity and positive helicity of the x-ray beam yields an XPEEM XMCD image in which black and white contrast indicate the magnetization direction parallel or antiparallel with respect to the photon angular momentum direction of the incoming x-rays. Gray contrast indicates that either the magnetization direction is perpendicular to the photon angular momentum or that it is fluctuating with a fluctuation time smaller than the time constant of the measurement.

In order to illustrate the quality of the images, which were obtained with the XPEEM at BESSY three images of a sample are shown for comparison in figure 5.1. On the left of the figure (A) an SEM image is shown, where three separated nanoparticles are marked by a circle. For better visibility the encircled region is enlarged in the inset of all three images. The broad structures at the bottom left and the top right are parts of the lithographically written gold markers (see figure 3.4). The markers can be used to identify the same particles in the XPEEM and the corresponding SEM image.

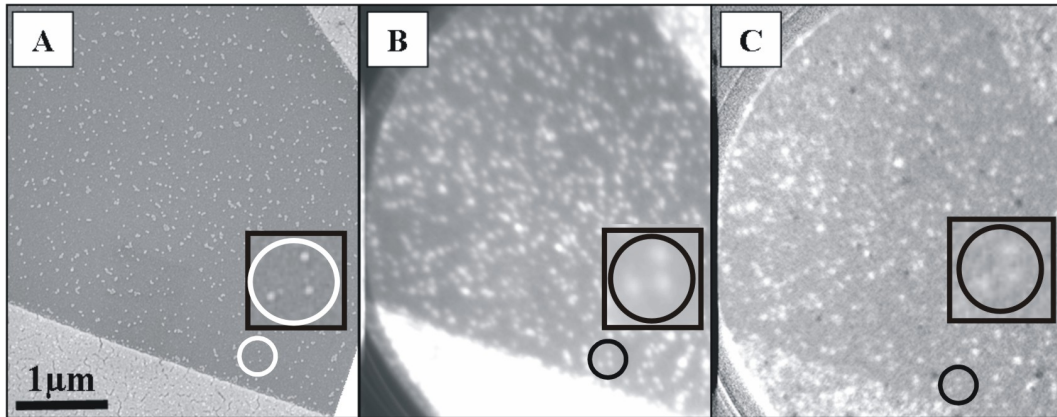


Figure 5.1: Left (A): SEM image showing a sample of iron nanoparticles within a marker. Three individual particles are marked by a circle.

Center (B): XPEEM image of the same region of the sample as shown in (A) with the same three nanoparticles encircled to show, that they are individually resolved.

Right (C): XPEEM image with the XMCD effect used as contrast mechanism.

In the center of figure 5.1 (B) an XPEEM image at the Fe L_3 -edge of the same sample region as in (A) is shown. During the measurement a magnetic

field of 9 mT was applied along the x-ray beam and parallel to the sample which was at room temperature. For this image the images acquired for right and left circular polarization of the x-rays were added up. Three individual nanoparticles are visible in the circle and as one can see they are all individually resolved.

In figure 5.1 (C) the same sample region as in (A) and (B) is shown again, however in this image the XPEEM sum images acquired for left and right polarized x-rays were not added up but subtracted from each other and therefore the contrast mechanism is the XMCD effect. This effect yields only a fraction of the signal as for the sum, however also in this image the three individual particles can be resolved.

Instabilities and drifts during the image acquisition demanded short image acquisition times, however in order to obtain enough statistics many images were taken and then corrected for drifts in between. In order to achieve such an image quality, as seen in figure 5.1, several hundreds of aligned images are summed up. Furthermore optimal illumination of the sample in the field of view of the XPEEM and optimal alignment of the XPEEM electron optics is important for all images.

5.1.1 Single Nanoparticle Spectroscopy

In order to obtain absorption spectra from XPEEM images, the photon energy is tuned in small intervals around the absorption edge and an image is acquired for each energy-step.

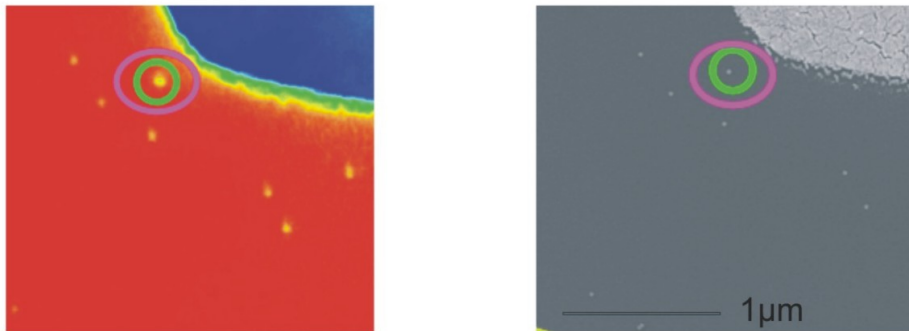


Figure 5.2: Left: Illustration of a series of XPEEM images, which were corrected for drift in between. The green circle denotes the region of interest in which the particle is located. The space between the green and the pink circle is used for normalization. Right: SEM image of the same area on the sample for comparison. The particle is visible in the green circle and the clean substrate next to it in-between the two circles.

For illustration such a stack consisting of 150 images taken in 0.2 eV steps while tuning the photon energy from 700 to 740 eV is shown in figure 5.2 on the

left hand side and the corresponding SEM image of the same sample region is shown on the right hand side. For this measurements a non-reduced nanocube sample was used. The two circles in figure 5.2 mark two regions of interest. In the green circle one can see a light spot in the XPEEM image. A comparison with the SEM image shows that a nanoparticle is located there. From this region of interest the signal for the nanoparticle was acquired. The region between the green and the pink circle was used for normalization. It is clearly visible from the SEM image that no particle is present in that region and therefore the signal is caused by background signals, e.g. from the substrate.

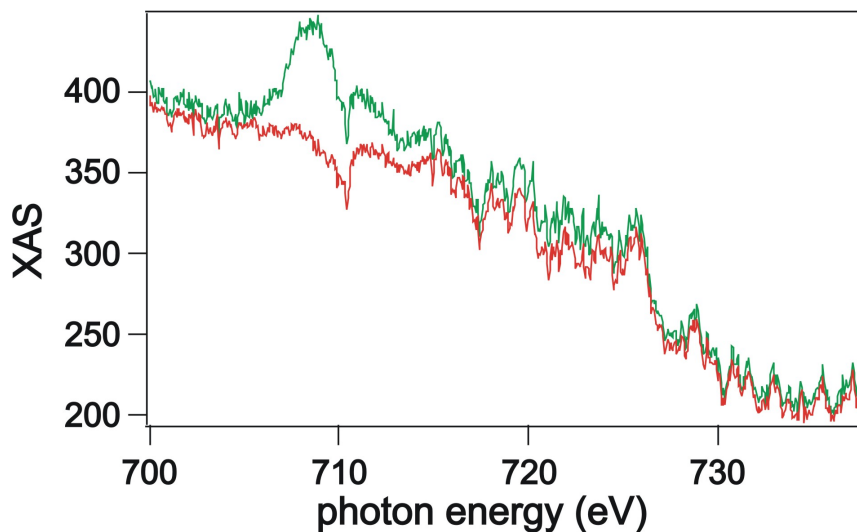


Figure 5.3: Fe $L_{2/3}$ -edge XAS spectrum of two regions of interest: The particle region (green) and the normalization region without any particle (red).

In figure 5.3 the x-ray absorption spectrum of x-rays with linear polarization for the two regions of interest one with a particle (inside the green circle) depicted in green and the other the normalization reference (area in between green and pink circle from figure 5.2) depicted in red is shown for the energy region in the vicinity of the Fe $L_{2/3}$ -edges. To obtain a XANES spectrum the signal is normalized to the area of the individual region of interest. The signal is clearly dominated by the background signal, however the clear difference between the red and the green curve is visible.

In figure 5.4 the XANES spectrum at the Fe $L_{2/3}$ -edge is shown, which is the difference between the green and the red curve in figure 5.3 corresponding to the signal per area from a single nanocube and the reference region with only bare substrate respectively. The L_2 and L_3 -edge of Fe can be recognized easily. The edge jump is very small, which is reasonable for such low amounts of material like a single nanocube. In literature one can find only one other measurement of single nanoparticle spectra. The spectra recorded with XPEEM for single Co

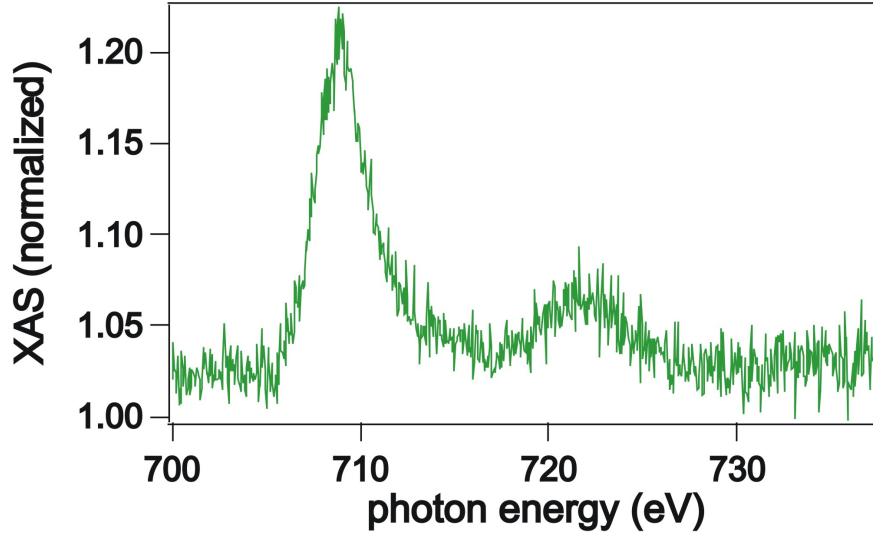


Figure 5.4: Fe $L_{2/3}$ -edge XAS spectrum for a single nanocube with the signal from the region of the nanoparticle normalized to the signal from a sample region without particle.

nanoparticles with an average diameter of 8 nm are comparable to the spectrum here in signal-to-noise ratio [83]. In current experiments the magnetic properties of single nanoparticles are studied employing the XMCD effect.

5.1.2 Magnetometry: Integral versus Single Particle

As described before from the XPEEM images, which were acquired for left and right circular polarized x-rays, spectra of individual nanoparticles could be extracted by defining a region of interest from which the signal was taken for the particles and the reference for background subtraction. However apart from spectra also hysteresis loops have been recorded with this method. Therefore XPEEM images for both helicities were acquired at each field point of a $M(H)$ measurement. To yield a hysteresis loop the normalized XMCD signal was read out at the respective region of interest as a function of applied magnetic field. The magnetic sample holder (described in chapter 2.2.2) allowed to apply an inplane magnetic field and allowed to record images in an applied field of up to ± 25 mT. XPEEM imaging with such magnetic fields has not been reported yet and with other techniques like STXM only hysteresis for larger structures (Fe/Gd multilayers deposited on ~ 160 nm nanospheres) have been measured up to now [84]. The first results are shown in the following. In figure 5.5 an SEM image and the corresponding XPEEM image recorded at the L_3 -edge of the same sample region are depicted. In colored circles different nanocube configurations are shown. The sample temperature during the measurement was 110 K (± 10 K).

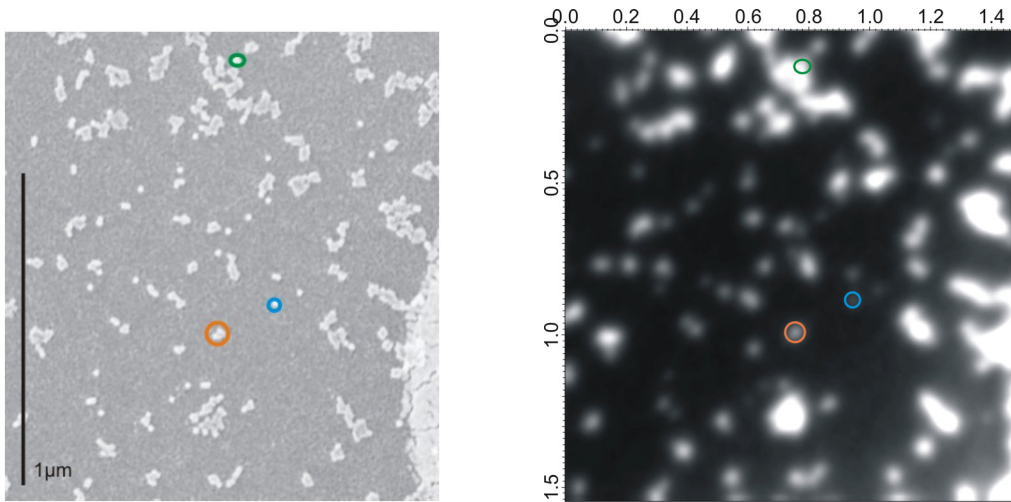


Figure 5.5: Left: SEM image showing a nanoparticle sample with three different nanocube configurations encircled: A single isolated nanocube (blue), a nanocube cluster adjacent to an ensemble of other nanocubes (green) and three agglomerated nanoparticles (orange).

Right: XPEEM image of the same area of the nanoparticle sample.

A single nanocube, which is separated from the other nanocubes by about 100 nm, is located within the blue circle, therefore interactions with other particles are expected to be negligible. For this single nanocube a hysteresis was recorded at the L_3 -edge and is shown in figure 5.6. Note, that the averaged signal obtained from all images was set to one and the XMCD is therefore given in arbitrary units. The experimental setup at the XPEEM does not allow to indicate the absolute magnetic field direction, however the convention ($I^- - I^+$) of XMCD gives a negative signal at the Fe L_3 -edge and therefore the hysteresis appears inverted compared with the hysteresis known from SQUID for Fe. A clear switching behavior can be observed with the switching of the magnetic field.

In figure 5.7 a hysteresis for three adjacent nanocubes is shown (marked in the orange circle in figure 5.5). This particle configuration is denoted in the orange circle in figure 5.5. If one compares the shape of the hysteresis loops for the single particle (figure 5.6) and for the cluster of three adjoining particles (figure 5.7), one notices that the shape of the single particle hysteresis is more rounded indicating a smaller magnetic moment, whereas the hysteresis for the three particles has a more squarish appearance typical for a larger magnetic moment. Therefore one can conclude that the three individual moments of the particles are coupled.

In figure 5.8 the hysteresis loop for a coupled nanoparticle configuration is shown (denoted by the green circle in figure 5.5). In the SEM image in figure 5.5 it can be seen, that the particle configuration appearing as one big cluster is a complex entity of several nanoparticles. Here the hysteresis loop shows a

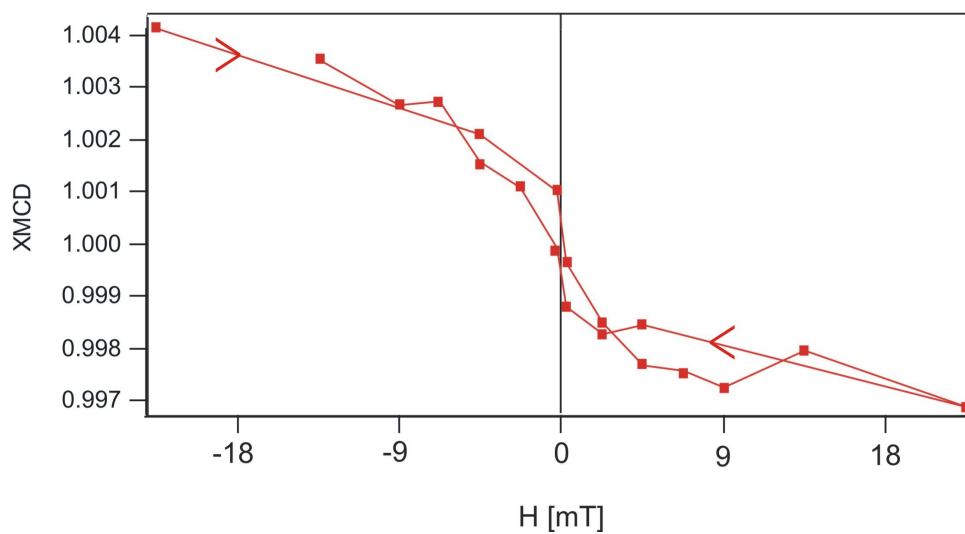


Figure 5.6: XMCD hysteresis recorded at the L_3 -edge of Fe with XPEEM for a single Fe nanocube.

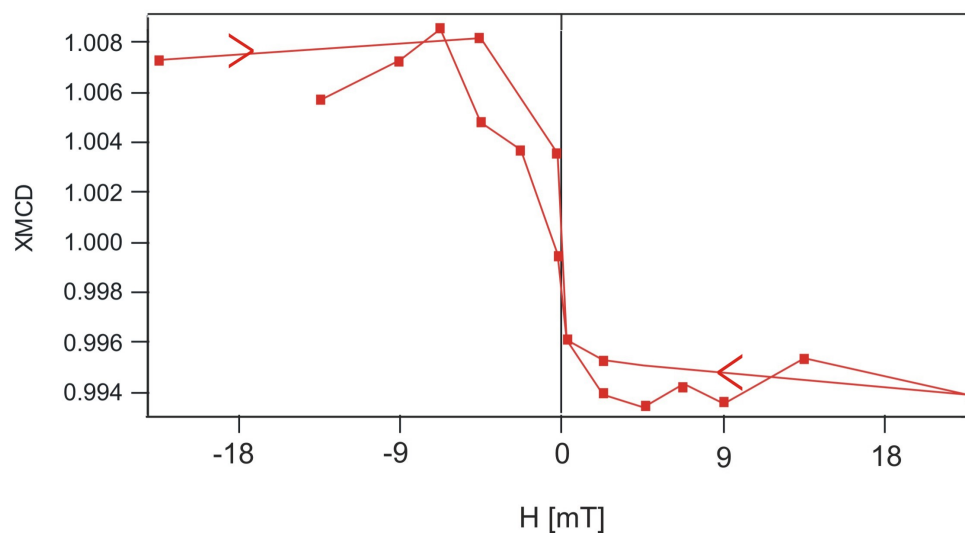


Figure 5.7: XMCD hysteresis recorded at the L_3 -edge of Fe with XPEEM for three adjoining Fe nanocubes.

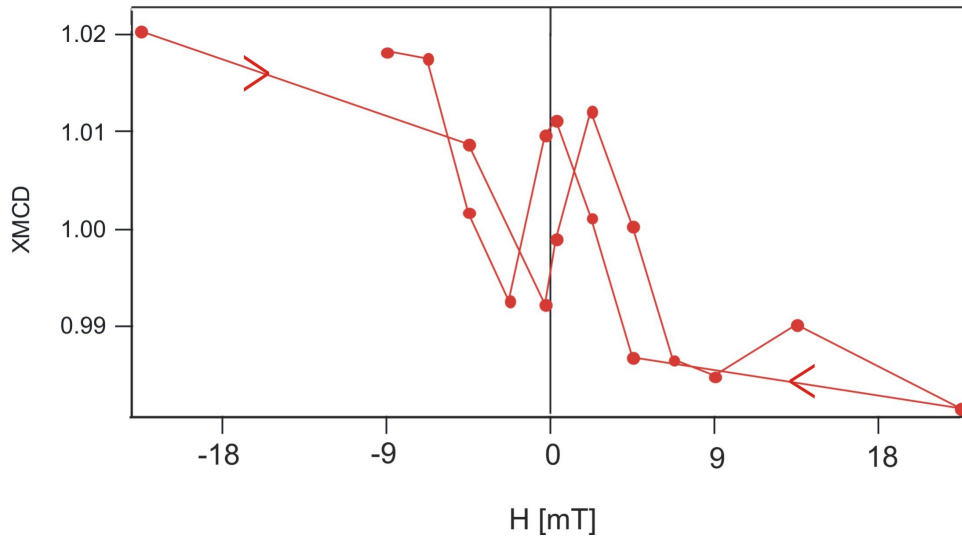


Figure 5.8: Hysteresis recorded at the L_3 -edge of Fe with X-PEEM for a Fe nanocube cluster, which is located in the vicinity of an agglomeration of other nanocubes.

complex switching behavior of the cluster indicating strong dipolar interactions. The contrast of the XMCD switches forth and back. Such a complex switching behavior could be observed at several positions on the sample and since the change in contrast is significant and does not fluctuate during the acquisition of the images noise can be excluded as cause for the complex shape of the hysteresis loop.

Measurements were also done with integral SQUID magnetometry in order to compare with the elementspecific measurements of individual nanoparticles. However since the sample size required for the sample holder in the XPEEM and the SQUID is different, the sample measured with SQUID and the one measured with XPEEM are not identical, e.g. the SQUID sample might have a slightly different coverage with nanoparticles. In figure 5.9 the hysteresis of a reduced and Al capped iron nanocube sample at 5 K and at 300 K is shown. Before the the hysteresis was recorded the sample was cooled in 4 T. In the inset the region of small applied magnetic fields is enlarged. For the hysteresis recorded at 5 K one can see a clear shift of the hysteresis. Such an "exchange bias" is known for the Fe/ Fe_xO_y nanoparticles [55] and has been attributed to the Fe/ Fe_xO_y interface. The particles were reduced by H_2 plasma treatment like the ones studied with XPEEM where no sign of Fe_xO_y was visible. However, the XPEEM detects electrons and is therefore only sensitive to the first few nanometers, but the nanocubes are about 18 nm thick. Hence it cannot be excluded, that Fe_xO_y is present. Due to the cubic shape of the particles it is also likely, that the H_2 -plasma could not reach the Fe_xO_y on the bottom of the nanocube, where it rests on the substrate. The respective SQUID measurements for a sample with non-

reduced particles are depicted in the appendix in figure D.2. In the inset on the right the field dependence of the magnetization measured in a field of 10 mT is shown for the the ZFC case (no field applied during cooling) and for the FC case (4 T applied during cooling). A separation of the two curves is visible up to about 200 K.

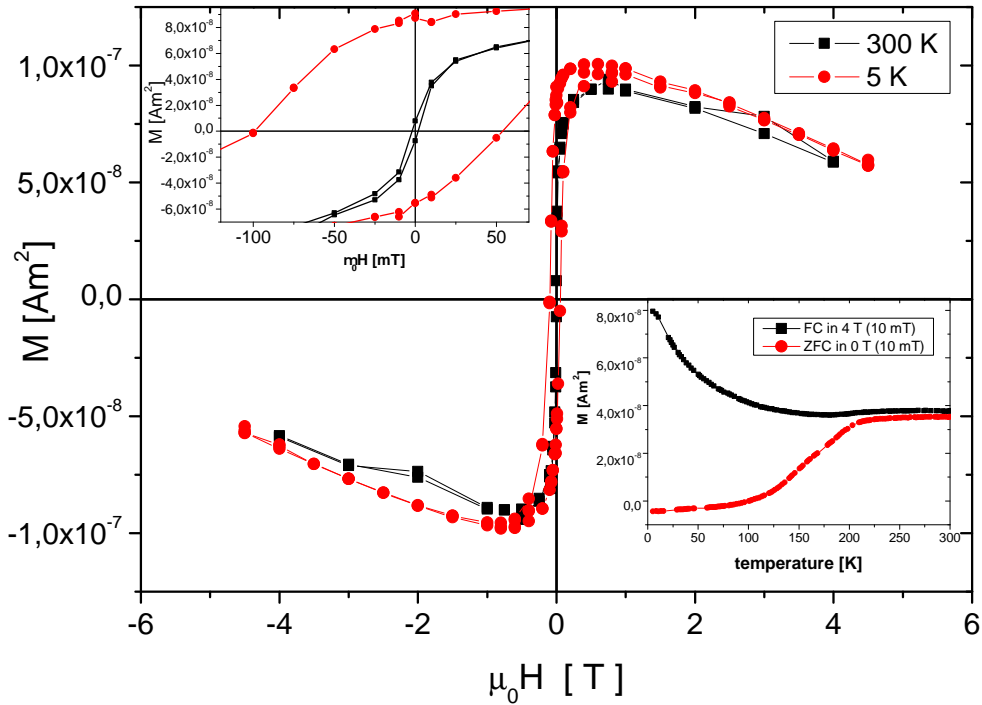


Figure 5.9: SQUID measurements for a reduced and Al capped nanoparticle sample. For the recorded hysteresis a magnetic field was applied during cooling (FC). The measurements were done in an inplane geometry. In the inset FC and ZFC measurements are shown.

In conclusion XPEEM is a promising approach towards the magnetic characterization of individual magnetic nanoparticles. It has been demonstrated by these first results, that both x-ray absorption spectra and hysteresis of individual nanoparticles can be obtained. A combination of these both techniques forms a versatile tool to further study the influence of individual properties of nanoparticles and their environment on the electronic and magnetic properties.

5.2 Imaging Nanocubes with X-ray Speckles

The second method used in order to study the nanocubes with x-rays was to record and analyse the speckle pattern. In our experiments reference holes with a diameter of about 30 nm have been used generating a reference wave to encode the phase information into the scattering pattern. An example of a speckle pattern recorded for a holography sample can be seen in figure 5.10. The dark circle in the center of the speckle pattern is the beamstop, which blocks the central beam, where the intensity distribution resembles an airy-function and is therefore significantly more intense. In this area the CCD camera recording the speckle pattern would saturate even for a short exposure time, while for the rest of the speckle pattern one has not enough statistics. Therefore the central part is generally blocked from the CCD with a beamstop.

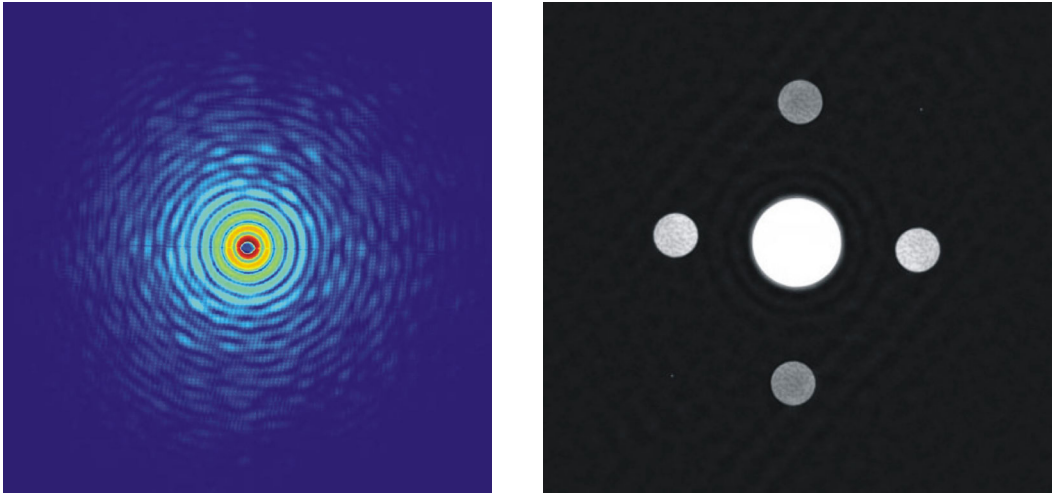


Figure 5.10: Left: Speckle pattern of a nanoparticle holography sample shown in color scale. The dark round spot in the center and the fine horizontal line is the beamstop, which is mounted on a fine wire.

Right: FOURIER transform of a speckle pattern from a nanoparticle holography sample after an iterative computational evaluation in order to reconstruct the area in the speckle pattern hidden by the beamstop.

It has been demonstrated that the lost phase information can also be obtained by computational phase retrieval algorithms constituting a 'computational lens', which was first shown for optical data [85] and then extended to the x-ray regime as demonstrated by a reconstruction by MIAO and co-workers of a two-dimensional nonperiodic x-ray image at $0.075 \mu\text{m}$ resolution from diffraction data and a low-resolution image of the object acquired by another microscopy technique in 1999 [86]. The image of the object is used to substitute the central part of the speckle pattern, which was blocked by the beamstop. This central part of

the speckle pattern can then afterwards, before the computational phase retrieval algorithms are applied, be replaced by the squared magnitude of the FOURIER transform of an image of the object. The image does not necessarily need to have the same resolution. It has been shown, that the central part of the speckle patterns can also be recovered by the use of the iterative algorithms themselves [87]. For the phase retrieval algorithms sufficiently strong constraint conditions are necessary in order to gain an unambiguously reconstructed image. Such a constraint can be the support of the object, that is for example the aperture milled into the gold film.

Differently sized beamstops are utilized and speckle patterns are recorded with the bigger beamstop to acquire better statistics for the high q part of the speckle pattern and then with a small beamstop, which blocks only the very center of the central beam for better low q data measured with shorter exposure times to prevent saturation of pixels in the CCD. These different patterns can be scaled afterwards and stiched together.

Depending on the intensity it is sometimes also possible to measure without any beamstop. The shortest possible exposure time is $t = 0.05s$ which is given by the speed of the shutter in front of the CCD during read out.

In this study no prior knowledge about the sample was assumed. The low q information was retrieved by iterative computational algorithms as has been done with the computational lens approach. Before the general computational data processing, cosmic rays, which were detected by the CCD, were removed by comparison of the intensity of each pixel for one frame of images with the intensity of another frame and then, if the difference is larger than a threshold value, the pixel with higher intensity is substituted with the one with less intensity. After the cosmic ray removal the frames were added up before further processing. For that an airy-function is fitted into the center of the speckle pattern, where the information is missing. Afterwards the speckle pattern is FOURIER transformed. In this FOURIER transform of the speckle pattern deviations from the ideal autocorrelation are detectable especially in the area in between the self-correlation and the cross-correlations, which should be black because no signal is expected there. A black mask is then superimposed, which substitutes this intermediate area in the FOURIER transform. In the following an inverse FOURIER transform is performed and the central part of the original speckle pattern is substituted by the corresponding area in this newly acquired speckle pattern. This procedure is repeated several times until the noise in the intermediate region of the autocorrelation is sufficiently reduced.

In figure 5.10 on the right side the FOURIER transform of a speckle pattern from a nanoparticle holography sample, that is the squared magnitude of the complex autocorrelation, is shown, which was already processed in order to reconstruct the information missing in the center of the speckle pattern due to the beamstop. For this reconstruction from the FOURIER transform hologram a nanoparticle sample with a similar sample structure as in figure 3.5 was used

except for one difference: Instead of just one reference hole two identical reference holes were drilled into the gold film and membrane. In the reconstructed image one can see a bright large circle in the center, which is the self-correlation of the object and the reference holes. As one can see, there are four images of the object surrounding the self-correlation, these are the cross-correlations from the object and each reference. For each reference hole two redundant images of the object appear. One image is the cross-correlation of the reference with the object and the other is the the complex conjugate, which is located radially opposite from the origin. This multiple reference FOURIER transform holography was demonstrated for soft x-rays by B. SCHLOTTER *et al.* [88].

The use of multiple references is advantageous because it allows to acquire multiple effectively identical subimages at a time, which can be aligned and averaged to generate an enhanced composite image. Since each subimage has exactly the same rotational orientation, the alignment is Cartesian, which is accomplished easily with a two-dimensional cross-correlation.

The averaging of sub-images naturally improves the image quality and the signal-to-noise ratio (SNR) is improved with the number of references N with the square root of N : $SNR_N = \sqrt{N}(SNR)_1$. This leads to an improved image and allows a shorter exposure time of the sample to the x-ray beam, which reduces possible radiation damage and also increases the image quality for future experiments with single shot imaging as planned for x-ray lasers. However, the use of multiple references is limited. The reference holes should be arranged in a way to avoid overlap between images in the autocorrelation, which can be achieved if no reference is located within the boundaries of the object and the object can be translated about the sample mask and overlaps with only one reference hole at a time [89]. This limits the number of references because they are all arranged on a circle around the center (with the object being in the center) with a radius limited in order for the cross-correlations not to overlap with the self-correlation in the center. Furthermore the reference holes have to be nearly identical and symmetric for identical subimages, however the drilling of these small structures was one of the major challenges in this experiment, because the FIB must be focused in the plane of the membrane for such small structures, and during focussing material already is removed, thinning down the gold film on the membrane. This leads to the fact that the x-ray beam is not fully attenuated by the remaining gold film resulting in artefacts in the speckle pattern, which limit the quality of the acquired data for example by limiting the exposure time for the CCD. Therefore, no sample structure with more than five reference holes was fabricated during this experiment.

In figure 5.11 a section of the sample with iron nanocubes is shown for which the FOURIER transform of the speckle pattern is depicted in figure 5.10. On the left side an SEM image of the nanoparticle configuration on the sample is shown. A black mask is superimposed on the SEM image to illustrate the position of the aperture milled into the gold film on the backside by FIB. On the right the same

sample is shown, however this image is the composite image acquired using FTH with the two reference holes as discussed earlier.

It is obvious, that the resolution of the image reconstructed from FTH is not equal to the resolution achieved with SEM. The individual nanocubes are not resolved in the right image whereas they can clearly be distinguished in the SEM image on the left side. However it is possible to recognize the different nanoparticle configurations.

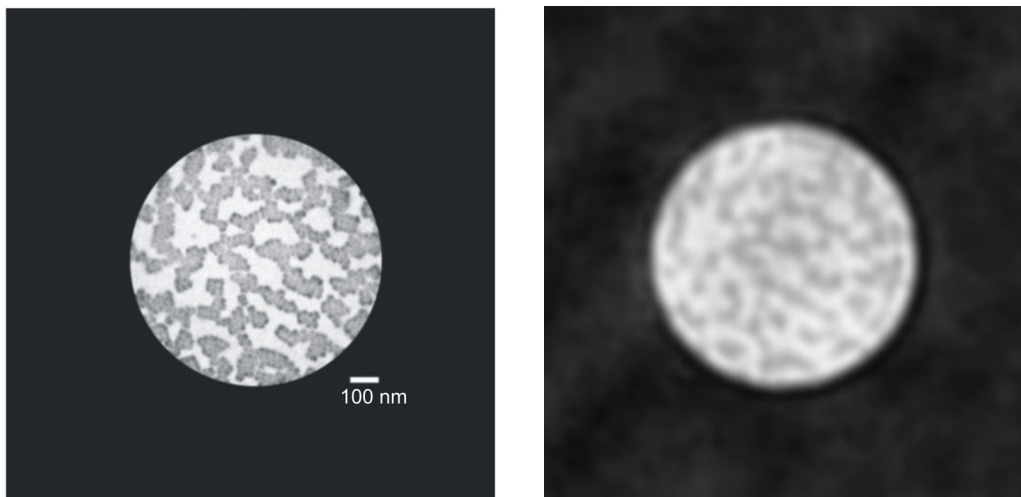


Figure 5.11: Left: SEM image showing a nanoparticle sample in the vicinity of the aperture (object). Right: Image of the same area of the nanoparticle sample reconstructed from FTH.

The computational processing of the speckle pattern data is not optimized yet and further improvements of the processing procedure are currently addressed. Therefore the reconstructed image is only a first evaluation of the data. Another point is the quality of the samples used for imaging the nanocubes with FTH. The smallest reference holes had a diameter of about 30 nm and were not perfectly symmetric.

Another remaining challenge is the imaging of the nanocubes using magnetic contrast. For that an electro-magnet was installed, which supplied a magnetic field up to 0.11 T along the beam direction. In order to yield magnetic contrast also cooling of the sample was necessary. However for cooling a cryostat had to be installed, which allowed helium cooling of the sample down to about 13 K and up to now vibrations of the sample holder resulted in shifts of the speckle pattern. Since the XMCD effects yields only a fraction of the signal, which is used for non-magnetic imaging, enough statistics for the acquired data is important. For future experiments the vibrations of the cryostat have to be eliminated.

As a conclusion from these first experiments one can deduce that imaging of the nanocubes with speckles is possible and while the experiments are very

challenging it appears possible in the future to detect a time dependent magnetic signal and extend the imaging to x-ray photon correlation spectroscopy (XPCS), which allows to study the dynamic properties [90].

Chapter 6

Conclusion and outlook

In this thesis the magnetic and structural properties of two nanoengineered systems namely the DMS material Co:ZnO and Fe/FeO_x nanoparticles have been studied with elementspecificity using synchrotron radiation.

A goal for this thesis was the careful structural analysis of **Co:ZnO films** in order to distinguish between intrinsic properties and effects arising from phase-separated metallic Co clusters, especially regarding the presence of magnetic order at room temperature. X-ray linear dichroism (XLD) has been utilized to study the local structural quality of Co:ZnO. For a detailed analysis experimental spectra both at the Zn and Co K-edge have been combined with the corresponding simulations. In order to study the magnetic properties of the Co:ZnO films x-ray magnetic circular dichroism (XMCD) and conventional SQUID magnetometry have been used. It was shown, that for Co:ZnO with high structural perfection virtually all Co occupies substitutional Zn lattice sites and the ZnO matrix is broadly undisturbed by the dopant atoms. For such Co:ZnO a purely paramagnetic behavior was observed, with the isolated Co²⁺ exhibiting a BRILLOUIN-like paramagnetism with a moment of $4.1\mu_B$. The reduction of the total magnetization by about 30% could be explained assuming an antiferromagnetic coupling of Co-O-Co pairs which are a natural consequence of the stochastic dopant distribution of ZnO doped with 10% Co.

For Co:ZnO films fabricated with different growth parameters the onset of clustering could be observed by both a reduction of the XLD signal and a change of the spectral shape of the pre-edge region in the x-ray absorption near edge structure (XANES). With evolving clustering of Co a separation of field cooled (FC) and zero-field cooled (ZFC) curves measured by SQUID can be observed displaying a blocking behavior characteristic for a superparamagnetic ensemble. In future experiments the onset of cluster formation should be further investigated. Already the field dependence of the XMCD signal for such a clustered film has also been measured and is depicted in figure 6.1. The shape of the hysteresis is different from hysteresis acquired with SQUID and awaits explanation and further studies are necessary.

Other interesting issues are the effects of different treatments during and after the growth like annealing under different atmospheres.

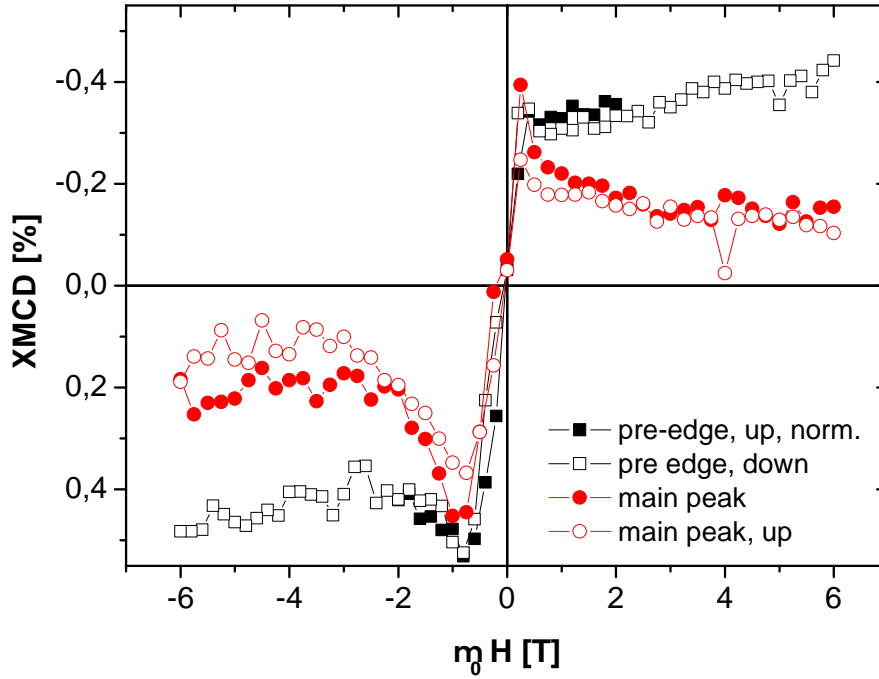


Figure 6.1: Field dependence of the XMCD signal for a Co:ZnO sample with metallic Co clusters.

As a second system **Fe/Fe_xO_y nanocubes** have been investigated using x-ray spectro-microscopy. With the first results achieved with x-ray photoelectron emission microscopy (XPEEM) it has been shown that both x-ray absorption spectra and hysteresis of individual nanoparticles can be obtained. The shape of the recorded XMCD-hysteresis is different for different configurations of nanoparticles. By identification of differently oriented nanocubes by SEM and in the corresponding XPEEM image it is possible to magnetically characterize the individual particles and correlate the magnetic behavior to the properties of the particle, e.g. the orientation with respect to each other or with respect to the applied magnetic field. It has been shown that XPEEM is a successful approach towards the magnetic characterization of individual magnetic nanoparticles and therefore allows to adress numerous arising questions such as the influence of shape or composition of a nanoparticle on the magnetic behavior, which could not directly be answered with integral magnetometry.

For future experiments there will be another sample holder available with a gap of only $50 \mu\text{m}$ (instead of $500\mu\text{m}$) and hence enabling a larger possible magnetic field due to the strong confinement of the magnetic field (because of the smaller gap and the corresponding smaller sample thickness as described in [44]) and the resulting smaller strayfields outside the sample. However, for this $50 \mu\text{m}$ gap sample holder a significantly stronger remanence of the sample holder itself is present, which could not be reduced up to now.

In order to yield a better understanding of the $\text{Fe}/\text{Fe}_x\text{O}_y$ nanocube properties theoretical calculations have been initiated. Furthermore, the measurements performed with XPEEM should be compared with conventional XMCD measurements of the same sample. In combination with a more detailed analysis of different particle configurations the averaged ensemble properties might be ascribed to a combination of the individual arrangements.

With FOURIER transform holography (FTH) a first reconstruction of a sample of $\text{Fe}/\text{Fe}_x\text{O}_y$ nanocubes from the hologram was shown. Up to now the particles could not be individually resolved.

The magnetic imaging of the nanocubes still remains even more challenging for the XMCD effects as a contrast mechanism yields only a fraction of the signal. Furthermore experimental difficulties like stability of the low temperature sample holder and alignment of the magnet in the beamline still have to be overcome before it is possible to detect a time dependent magnetic signal and extend the imaging to x-ray photon correlation spectroscopy (XPCS), which allows to study the dynamic properties [90].

Appendix A

X-Ray Data

A.1 Absorption Edges

Table A.1: Binding energies [91]

	<i>K</i> -edge	<i>L</i> ₁ -edge	<i>L</i> ₂ -edge	<i>L</i> ₃ -edge
core level	1 <i>s</i>	2 <i>s</i>	2 <i>p</i> _{1/2}	2 <i>p</i> _{2/3}
C	284.2	-	-	-
N	409.9	37.3	-	-
O	543.1	41.6	-	-
Al	1559.6	117.8	72.95	72.55
Fe	7112	844.6	719.9	706.8
Co	7709	925.1	793.2	778.1
Zn	9659	1196.2	1044.9	1021.8
Ga	10367	1299.0	1143.2	1116.4
Gd	50239	8376	7930	7243

A.2 Synchrotron Ring Parameters

Table A.2: Ring Parameters

	operation energy [<i>GeV</i>]	maximum current <i>I</i> [<i>mA</i>]	critical energy <i>E_c</i> [<i>keV</i>]
BESSY II [39]	1.7	300	0.57
ESRF [92]	6.0	200	7.13
SSRL [93]	3.0	100(500)	7.6

Appendix B

Quarter Wave Plate

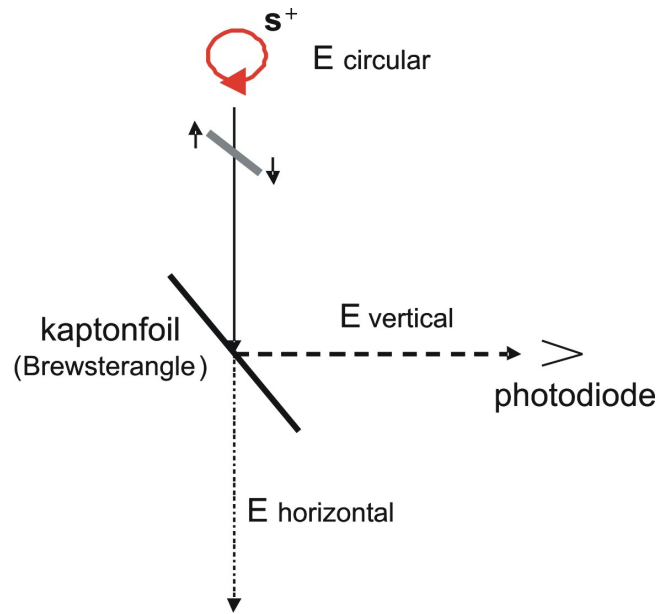


Figure B.1: Schematic of the QWP setup: Circularly polarized light from the synchrotron incides on the QWP, which can be tilted with a piezo. A kaptonfoil under the BREWSTER angle acts as a beamsplitter for electric field vector E horizontal and E vertical. The intensity reflected by the kaptonfoil is detected by a photodiode.

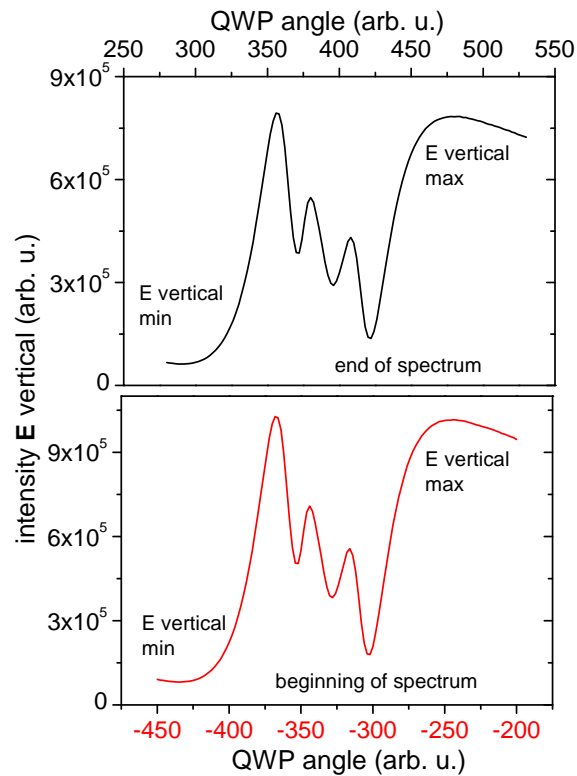


Figure B.2: Intensity detected by the photodiode (figure B.1) in dependence on the tilt of the QWP at two different photon energies (at the end and at the beginning of a spectrum). For linear polarization the QWP can then be flipped between the minimum value for $E_{vertical}$ (maximum $E_{horizontal}$) and maximum $E_{vertical}$ (minimum $E_{horizontal}$). Since the position of the BRAGGpeak is energy dependent, the orientation of the QWP has to be adjusted for each energy step. For that the QWP is scanned at the energy position of beginning of a spectrum and the one of the end. During the spectrum the orientations of the QWP are interpolated.

Appendix C

FDMNES-code

C.1 Input file

```
! Indata file for the fdmnes program
! Calculation of the Zn K edge in wurtzite ZnO.
```

Comment

```
    K edge of Zn
```

Filout

```
    ZnK-r85
```

Range

```
    -20 1 -10. 0.5 -5 0.25 20 1 60.
```

Green

Edge

```
    K
```

Polarise

```
    1.0 0.0 0.0
```

```
    0.0 0.0 1.0
```

Radius

```
    8.5
```

```
!Density
```

```

Atom
  30 2  3 2 10   4 0 2
   8 2  2 0 2   2 1 4
  27 2  4 0 2   3 2 7

spgroup
P63mc

cryst
  3.2495 3.2495 5.2069 90. 90. 120.
1 0.33333333 0.66666667 0.00000000
1 0.66666667 0.33333333 0.50000000
2 0.33333333 0.66666667 0.38200000
2 0.66666667 0.33333333 0.88200000

!absorbeur
!  2

energpho

Arc
  35 35 9

Efermi
  -4

Gamma_hole
  2,74

End

```

In the above input file for the FDMNES code [70] the parameters necessary are listed. With the parameter 'range' the size of the energy steps for different energy intervals, which are specified relative to the edge, e.g. 1 eV steps from 20 eV below the edge to 10 eV below the edge and so on. 'Green' specifies the use of the muffin-tin approximation. K-edge spectra ('Edge K') were simulated for two orthogonal linear polarization directions ('Polarise'). The radius of the cluster for the simulation was $r=8.5 \text{ \AA}$ in chapter 4.1.1. In addition to the simulations with different clusterradii for the Zn K-edge depicted in figure 4.3 respective simulations have been performed for the Co K-edge depicted in figure C.1. With the keyword 'atom' the atoms which are in the crystal, that is in our case Zn, O and Co, are described with the atomic number Z , the number of valence

orbitals, the quantum numbers n and l and the occupation. The space group of the crystal can be given with the keyword 'spgroup'. The positions of the atoms in the crystal are given with the lattice vectors a , b and c and the angles between them α , β and γ ('cryst'). The absorbing atoms can be chosen with the keyword 'absorbeur'.

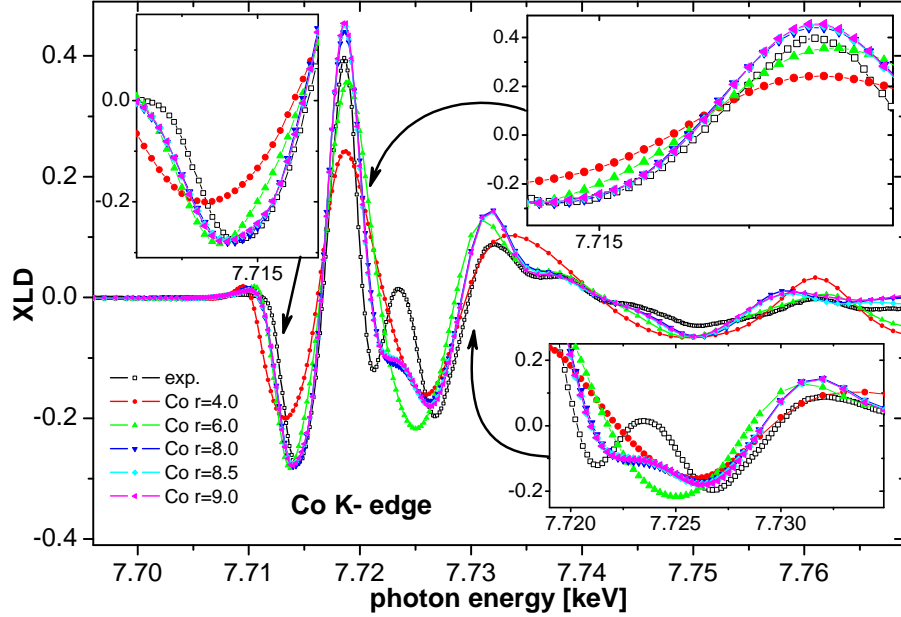


Figure C.1: XLD spectra at the Co K-edge simulated with different cluster radii for the simulation and an experimental spectrum for comparison.

With the last parameters in the input file ('Arc', 'Efermi' and 'Gamma_hole') the convolution of the spectra is specified.

C.2 Convolution

With the parameter 'Arc' and arctangent-like energy-dependent broadening of the energy levels is introduced as described in chapter 4.1.1. The shape of the arctangent is depicted in figure C.2. The initial corehole level width is given by 'Gamma_hole'. As described in chapter 4.1.1 it is generally necessary to shift the energy of the occupied levels which are cut off for the simulated spectra in order to reproduce all features in the spectra at the pre-edge. This shift relative to the

FERMI energy determined by the FDMNES code is specified with the keyword 'Efermi'.

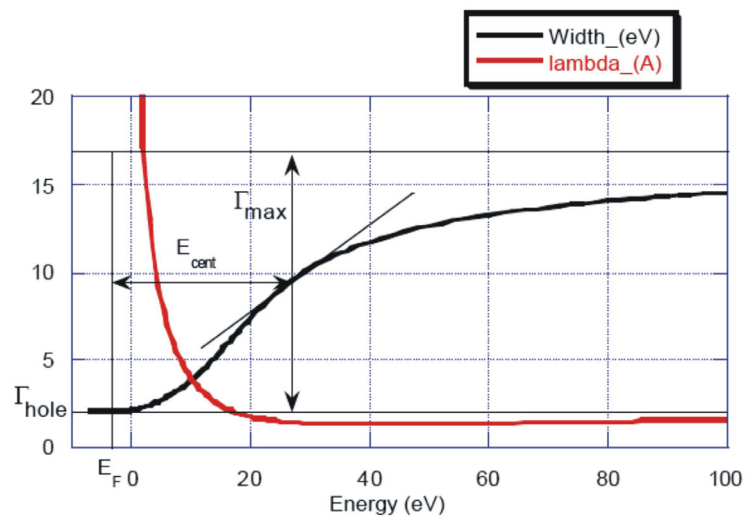


Figure C.2: Arctangent utilized for the energy dependence of the corelevel width.

Appendix D

Additional Data

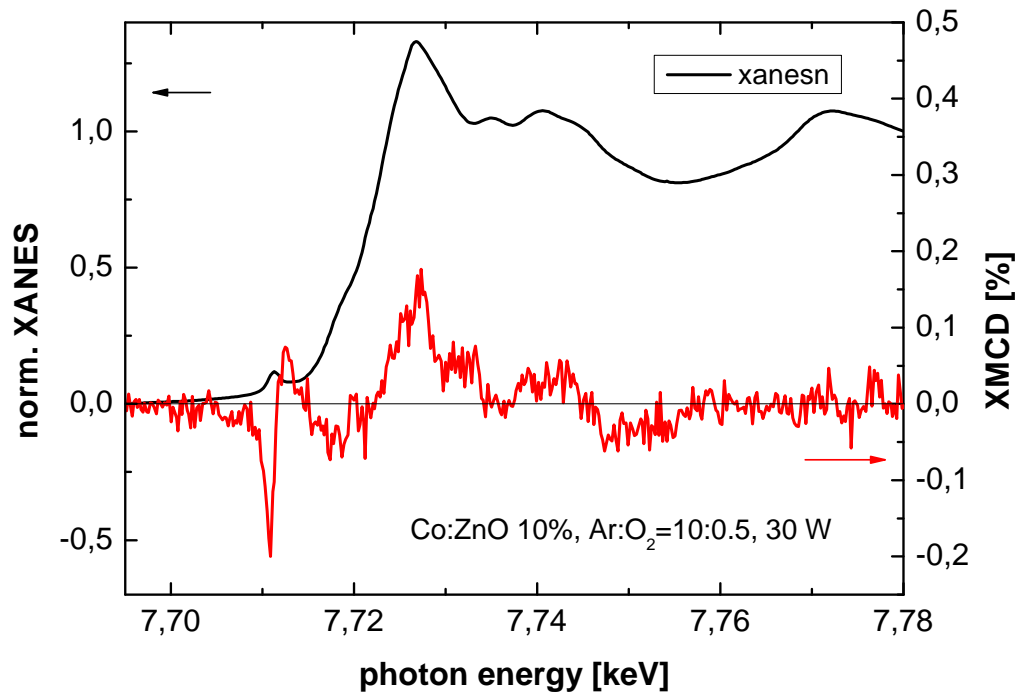


Figure D.1: XANES and XMCD spectrum at the Co K-edge of a sputtered Co:ZnO sample with Co clusters. In comparison with the XANES and XMCD spectra for a Co:ZnO film with excellent structural quality depicted in figure 4.15 the XMCD signal at both pre-edge and main peak is significantly reduced for the clustered film. As described in chapter 4.1.2 the lineshape of the pre-edge region of the XANES is more filled between the pre-edge and the main-edge.

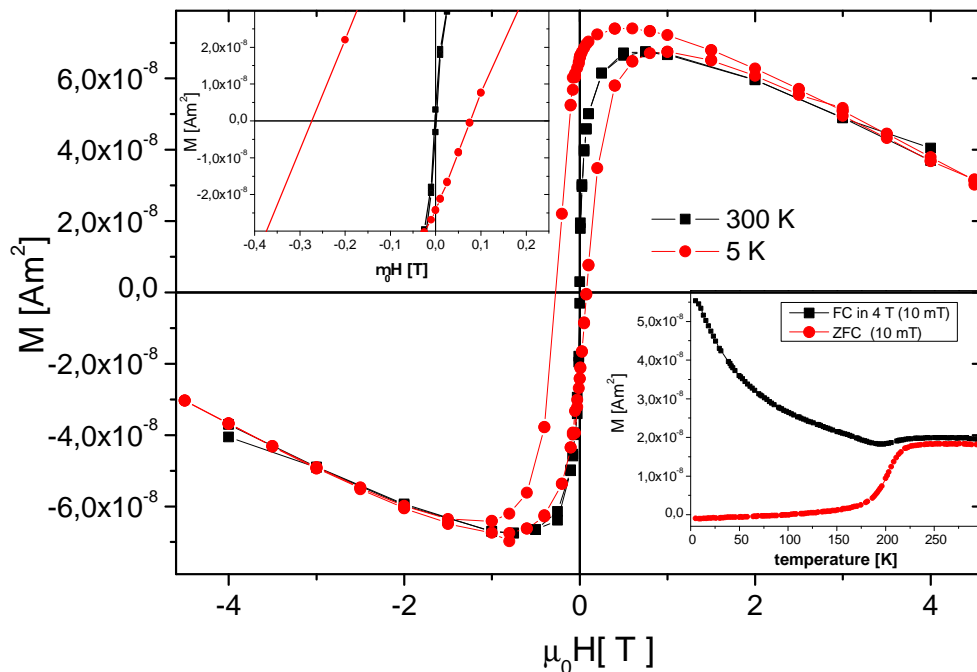


Figure D.2: SQUID measurements for a non-reduced nanoparticle sample. For the recorded hysteresis a magnetic field was applied during cooling (FC). The measurements were done in an inplane geometry. In the inset FC and ZFC measurements are shown. In comparison with the SQUID measurements for a reduced nanoparticle sample shown in figure 5.9 a significantly larger exchange bias is visible in the hysteresis at 5 K for the non-reduced nanoparticles. Also the FC and ZFC are different with a steeper blocking peak in the ZFC shifted towards higher temperatures.

Bibliography

- [1] J. Stöhr and H. C. Siegmann, *Magnetism: From Fundamentals to Nanoscale Dynamics*, Springer Verlag, Berlin (2006)
- [2] S. Datta and B. Das, *Appl. Phys. Lett.* **56**(7), 665 (1990)
- [3] A. J. Behan, A. Mokhtari, H. J. Blythe, D. Score, X.-H. Xu, J. R. Neal, A. M. Fox and G. A. Gehring, *Phys. Rev. Lett.* **100**, 047206 (2008)
- [4] T. C. Kaspar, T. Droubay, S. M. Heald, P. Nachimuthu, C. M. Wang, V. Shutthanandan, C. A. Johnson, D. Gamelin and S. C. Chambers, *New J. Phys.* **10**, 055010 (2008)
- [5] A. Jordan, R. Scholz, K. Maier-Hauff, M. Johannsen, P. Wust, J. Nadobny, H. Schirra, H. Schmidt, S. Deger, S. Loening, W. Lanksch and R. Felix, *J. Magn. Magn. Mater.* **225**, 118 (2001)
- [6] D. Weller and A. Moser, *Magnetics, IEEE Transactions on* **35**(6), 4423 (1999)
- [7] S. Sun, C. B. Murray, D. Weller, L. Folks and A. Moser, *Science* **287**, 1989 (2000)
- [8] C. Kittel, *Introduction to Solid State Physics*, Wiley, New York, international eighth edition (2005)
- [9] D. J. Chadi, R. M. White and W. A. Harrison, *Phys. Rev. Lett.* **35**(20), 1372 (1975)
- [10] P. Koidl, *Phys. Rev. B* **15**(5), 2493 (1977)
- [11] P. Sati, R. Hayn, R. Kuzian, S. Régnier, S. Schäfer, A. Stepanov, C. Morhain, C. Deparis, M. Laügt, M. Goiran and Z. Golacki, *Phys. Rev. Lett.* **96**, 017203 (2006)
- [12] P. Bruno, *Phys. Rev. B* **39**(1), 865 (1989)
- [13] G. van der Laan, *J. Phys.: Condens. Matter* **10**, 3239 (1998)

- [14] F. Wilhelm, P. Pouloupoulos, P. Srivastava, H. Wende, M. Farle, K. Baberschke, M. Angelakeris, N. K. Flevaris, W. Grange, J. P. Kappler, G. Ghiringhelli and N. B. Brookes, *Phys. Rev. B* **61**(13), 8647 (2000)
- [15] C. Antoniak, *Magnetische Eigenschaften des Legierungssystems Fe-Pt*, PhD Thesis, Universität Duisburg-Essen (2007)
- [16] M. Spasova, U. Wiedwald, R. Ramchal, M. Farle, M. Hilgendorff and M. Giesig, *J. Magn. Magn. Mater.* **240**, 40 (2002)
- [17] M. Jamet, W. Wernsdorfer, C. Thirion, D. Mailly, V. Dupuis, P. Mélinon and A. Pérez, *Phys. Rev. Lett.* **86**(20), 4676 (2001)
- [18] L. Néel, *Rev. Mod. Phys.* **25**(1), 293 (1953)
- [19] E. C. Stoner and E. Wohlfarth, *Proceedings of the Royal Society of London. Series A, Mathematical and Physical Sciences* **240**(826), 599 (1948)
- [20] W. F. Brown, *Phys. Rev.* **130**(5), 1677 (1963)
- [21] C. Antoniak, L. Lindner and M. Farle, *Europhys. Lett.* **70**(2), 250 (2005)
- [22] Y. Millev and M. Fähnle, *Phys. Rev. B* **51**, 2937 (1995)
- [23] C. Antoniak and M. Farle, *Mod. Phys. Lett. B* **21**(18), 1111 (2007)
- [24] M. de Broglie, *Comptes Rendus* **157**, 924 (1913)
- [25] H. Wende, *Reports on Progress in Physics* **67**(12), 2105 (2004)
- [26] C. Brouder, *J. Phys.: Condens. Matter* **2** (1990)
- [27] P. A. M. Dirac, *Proceedings of the Royal Society of London. Series A, Mathematical and Physical Sciences* **114**(767), 243 (1927)
- [28] E. Fermi, *Nuclear Physics*, University of Chicago Press, Chicago (1950)
- [29] J. J. Rehr and R. C. Albers, *Rev. Mod. Phys.* **72**(3), 621 (2000)
- [30] J. L. Erskine and E. A. Stern, *Phys. Rev. B* **12**(11), 5016 (1975)
- [31] G. Schütz, W. Wagner, W. Wilhelm, P. Kienle, R. Zeller, R. Frahm and G. Materlik, *Phys. Rev. Lett.* **58**(7), 737 (1987)
- [32] G. Y. Guo, *J. Phys.: Condens. Matter* **8**(49), L747 (1996)
- [33] W. Chao, B. D. Harteneck, J. A. Liddle, E. H. Anderson and D. T. Attwood, *Nature* **435**(30), 1210 (2005)

- [34] S. Eisebitt, J. Lüning, W. F. Schlotter, M. Lörger, O. Hellwig, W. Eberhardt and J. Stöhr, *Nature* **432**, 885 (2004)
- [35] W. F. Schlotter, *Lensless Fourier Transform Holography with Soft X-Rays*, PhD Thesis, Stanford University (2007)
- [36] F. van der Veen and F. Pfeiffer, *J. Phys.: Condens. Matter* **16**, 5003 (2004)
- [37] J. W. Goodman, *Statistical Optics*, Wiley, New York, wiley classics library edition (2000)
- [38] J. D. Jackson, *Classical Electrodynamics*, Wiley, New York, 2nd edition (1975)
- [39] Berliner Elektronenspeicherring - Gesellschaft für Synchrotronstrahlung m.b.H. (2008), <http://www.bessy.de/>
- [40] J. Goulon, A. Rogalev, C. Gaunthier, C. Goulon-Ginet, S. Paste, R. Signorato, C. Neumann, L. Varga and C. Malgrange, *J. Synchrotron Rad.* **5**, 232 (1998)
- [41] A. Rogalev, J. Goulon, C. Goulon-Ginet and C. Malgrange, *Magnetism and Synchrotron Radiation* **565**, 60 (2001)
- [42] Princeton Instruments, *Inc. of Trenton, NJ* (2008), <http://www.princetoninstruments.com/>
- [43] ELMITEC, *Elektronenmikroskopie GmbH, 38678 Clausthal-Zellerfeld, Germany* (2008), www.elmitec.de
- [44] J. Schlichting, *Magnetische Schaltprozesse in Exchange Bias Systemen: eine Photoelektronen-Mikroskopie-Studie*, Diplomarbeit, Freie Universität Berlin (2007)
- [45] F. Kronast, *private communication* (2008)
- [46] A. Ney, *A New Design of an UHV High- T_c -SQUID Magnetometer: Absolute Determination of Magnetic Moments of 3d-Transition Metal Films*, PhD Thesis, Freie Universität Berlin (2001)
- [47] QUANTUM Design, *Inc. 11578 Sorrento Valley Road, San Diego, CA* (2008), www.qdusa.com
- [48] A. Ney, T. Kammermeier, V. Ney, K. Ollefs and S. Ye, *J. Magn. Magn. Mater.* **320**, 3341 (2008)
- [49] R. Salzer, D. Spemann, P. Esquinazi, R. Höhne, A. Setzer, K. Schindler, H. Schmidt and T. Butz, *J. Magn. Magn. Mater.* **317**, 53 (200)

- [50] C. Klingshirn, M. Grundmann, A. Hoffmann, B. Meyer and A. Waag, *Physik Journal* **5**(1), 33 (2006)
- [51] E. H. Kisi and M. M. Elcombe, *Acta Cryst.* **C45**, 1867 (1989)
- [52] CrysTec GmbH, *12555 Berlin, Germany* (2008), www.crystec.de
- [53] T. Kaspar, T. Droubay, V. Shutthanandan, S. M. Heald, C. M. Wang, D. E. McCready, S. Thevuthasan, J. D. Bryan, D. Gamelin, A. J. Kellock, M. F. Toney, X. Hong, C. Ahn and S. A. Chambers, *Phys. Rev. B* **73**, 155327 (2006)
- [54] T. Kammermeier, *Investigation of magnetism in wide band gap dilute magnetic semiconductors based on GaN and ZnO*, PhD Thesis, Universität Duisburg-Essen (2008)
- [55] A. Shavel, B. Rodríguez-González, M. Spasova, M. Farle and L. M. Liz-Marzán, *Adv. Funct. Mater.* **17**, 3870 (2007)
- [56] M. Spasova, *private communication* (2008)
- [57] K. Fauth, E. Goering, G. Schütz and L. Kuhn, *J. Appl. Phys.* **96**(1), 399 (2004)
- [58] U. Wiedwald, K. Fauth, M. Heßler, H.-G. Boyen, F. Weigl, M. Hilgendorff, M. Giersig, G. Schütz, P. Ziemann and M. Farle, *Chem. Phys. Chem.* **6**, 2522 (2005)
- [59] H.-G. Boyen, K. Fauth, B. Stahl, P. Ziemann, G. Kästle, F. Weigl, F. Banhart, M. Hessler, G. Schütz, N. S. Gajbhiye, J. Ellrich, H. Hahn, M. Büttner, M. G. Garnier and P. Oelhafen, *Adv. Mater.* **17**(5), 574 (2005)
- [60] D. Zhu, *private communication* (2008)
- [61] T. Dietl, H. Ohno, F. Matsukura, J. Cibert and D. Ferrand, *Science* **287**(5455), 1019 (2001)
- [62] N. Akdogan, A. Nefedov, K. Westerholt, H. Zabel, H.-W. Becker, C. Somsen, R. Khailullin and J. Tagirov, *J. Phys. D* **41**, 165001 (2008)
- [63] P. Sati, C. Deparis, C. Morhain, S. Schäfer and A. Stepanov, *Phys. Rev. Lett.* **98**, 137204 (2007)
- [64] S. K. Nayak, M. Ogura, A. Hucht, S. Buschmann, H. Akai and P. Entel, *phys. stat. sol.* **205**(8), 1839 (2008)
- [65] M. Venkatesan, P. Stamenov, L. S. Dorneles, R. D. Gunning, B. Bernoux and J. M. D. Coey, *Appl. Phys. Lett.* **90**, 242508 (2008)

- [66] E. Sarigiannidou, F. Wilhelm, E. Monroy, R. M. Galera, E. Bellet-Amalric, A. Rogalev, J. Goulon, J. Cibert and H. Mariette, *Phys. Rev. B* **74**, 041306(R) (2006)
- [67] A. Ney, T. Kammermeier, E. Manuel, V. Ney, S. Dhar, K. H. Ploog, F. Wilhelm and A. Rogalev, *Appl. Phys. Lett.* **90**, 252515 (2007)
- [68] L. Tröger, D. Arvanitis, K. Baberschke, H. Michaelis, U. Grimm and E. Zschech, *Phys. Rev. B* **46**, 3283 (1992)
- [69] P. Pfalzer, J.-P. Urbach, M. Klemm, S. Horn, M. L. denBoer, A. I. Frenkel and J. P. Kirkland, *Phys. Rev. B* **60**(13), 9335 (1999)
- [70] Y. Joly, *Phys. Rev. B* **63**, 125120 (2001)
- [71] A. Barla, E. B. G. Schmerber, A. Dinia, H. Bieber, S. Colis, F. Scheurer, J.-P. Kappler, P. Imperia, F. Nolting, F. Wilhelm, A. Rogalev, D. Müller and J. J. Grob, *Phys. Rev. B* **76**, 125201 (2007)
- [72] M. O. Krause and J. H. Oliver, *J. Phys. Chem. Ref. Data* **8**(2), 329 (1979)
- [73] A. Kuzmin, S. Larcheri and F. Rocca, *Funct. Mater. and Nanotech.* **93**, 012045 (2007)
- [74] A. Ney, K. Ollefs, S. Ye, T. Kammermeier, V. Ney, T. C. Kaspar, S. A. Chambers, F. Wilhelm and A. Rogalev, *Phys. Rev. Lett.* **100**, 157201 (2008)
- [75] K. R. Kittilstved, D. A. Schwartz, A. C. Tuan, S. M. Heald, S. A. Chambers and D. R. Gamelin, *Phys. Rev. Lett.* **97**, 037203 (2006)
- [76] F. Wilhelm, *private communication* (2008)
- [77] R. E. Behringer, *J. Chem. Phys.* **29**(3), 537 (1958)
- [78] T. Dietl, T. Andrearczyk, A. Lipinska, M. Kiecana, M. Tay and Y. Wu, *Phys. Rev. B* **76**, 155312 (2007)
- [79] Q. Liu, C. L. Gan, C. L. Yuan and G. C. Han, *Appl. Phys. Lett.* **92**, 032501 (2008)
- [80] N. Friedenberger, *Layer resolved Lattice Relaxation in Magnetic Fe_xPt_{1-x} Nanoparticles*, Diplomarbeit, Universität Duisburg-Essen (2006)
- [81] V. F. Puentes, P. Gorostiza, D. M. Aruguete, N. G. Bastus and A. P. Alivisatos, *Nature materials* **3**, 263 (2004)
- [82] W. Wernsdorfer, *Adv. Chem. Phys.* **118**, 99 (2001)

- [83] A. Fraile Rodríguez, F. Nolting, J. Bansmann, A. Kleibert and L. J. Heyderman, *J. Magn. Magn. Mater.* **316**, 426 (2007)
- [84] E. Amaladass, B. Ludescher, G. Schütz, T. Tylizczak and T. Eimüller, *Appl. Phys. Lett.* **91**, 172514 (2007)
- [85] J. R. Fienup, *J. Opt. Soc. Am. A* **4**(1), 118 (1987)
- [86] S. Marchesini, H. He, H. N. Chapman, S. P. Hau-Riege, A. Noy, M. R. Howells, U. Weierstall and J. C. H. Spence, *Phys. Rev. B* **68**(14), 140101 (2003)
- [87] J. Miao, P. Charalambous, J. Kirz and D. Sayre, *Nature* **400**, 342 (1999)
- [88] W. Schlotter, R. Rick, K. Chen, A. Scherz, J. Stöhr, J. Lünning, S. Eisebitt, C. Günther, W. Eberhardt, O. Hellwig and I. McNulty, *Appl. Phys. Lett.* **89**, 163112 (2006)
- [89] J. Gaskill and J. Goodman, *Proceedings of the IEEE* **57**(5), 823 (1969)
- [90] M. Sutton and K. Laaziri, *Optics Express* **11**(19), 2268 (2003)
- [91] X-ray data booklet (2001), Lawrence Berkeley National Laboratory
- [92] European Synchrotron Radiation Facility (2008), <http://www.esrf.eu/>
- [93] Stanford Synchrotron Radiation Laboratory (2008), <http://www-ssrl.slac.stanford.edu/>

Curriculum vitae

I. Persönliche Daten

Name: Katharina J. Ollefs

Nationalität: Deutsch

Geburtstag und -ort: 26. Januar 1984, Moers

Permanent Address: Universität Duisburg-Essen
Fachbereich Physik
Lotharstr. 1
D-47048 Duisburg
Tel.: +49-379-2381
Fax.: +49-379-2098
email: katharina.ollefs@uni-due.de

II. Ausbildung

08/1990 bis 06/1994 GGS Waldschule, Moers-Schwafheim

08/1994 bis 06/2000 St. Hildegardis Gymnasium, Duisburg

08/2000 bis 06/2001 Immaculate Heart Central High School,
Watertown NY, USA

08/2001 bis 06/2003 St. Hildegardis Gymnasium, Duisburg
Abschluss: Abitur

seit 10/2003 Studium der Physik an der Universität Duisburg-Essen

10/2005 Diplom-Vorprüfung

03/2008 bis 06/2008 Forschungsaufenthalt am
Stanford Synchrotron Radiation Laboratory CA, USA
DAAD (D0747934)

Publications / Contributions to Conferences

1. A. Ney, K. Ollefs, S. Ye, T. Kammermeier, V. Ney, T. C. Kaspar, S. A. Chambers, F. Wilhelm and A. Rogalev
Absence of Intrinsic Ferromagnetic Interactions of Isolated and Paired Co Dopant Atoms in $Zn_{1-x}Co_xO$ with High Structural Perfection
Phys. Rev. Lett. **100**, 157201 (2008)
 2. A. Ney, T. Kammermeier, V. Ney, S. Ye, K. Ollefs, E. Manuel, S. Dhar, K. H. Ploog, E. Arenholz, F. Wilhelm, and A. Rogalev
Element specific magnetic properties of Gd:GaN: very small polarization of Ga and paramagnetism of Gd
Phys. Rev. B **77**, 233308 (2008)
 3. A. Ney, T. Kammermeier, V. Ney, K. Ollefs and S. Ye
Limitations of measuring small magnetic signals of samples deposited on a diamagnetic substrate
J. Magn. Magn. Mater. **320**, 3341 (2008)
-
1. K. Ollefs, S. Ye, V. Ney, T. Kammermeier, E. Manuel, A. Ney, F. Wilhelm, A. Rogalev, T. Kaspar, and S. Chambers
Element specific investigations of the structural and magnetic properties of Co:ZnO
Edgar Lüscher Seminar (Klosters, 2008)
 2. K. Ollefs, S. Ye, V. Ney, T. Kammermeier, A. Ney, F. Wilhelm, A. Rogalev, T. Kaspar and S. Chambers
Element specific investigations of the structural and magnetic properties of Co-doped ZnO
Frühjahrstagung der Deutschen Physikalischen Gesellschaft (Berlin, 2008)

Acknowledgements / Dank

"Last but not least" möchte ich all denen, die zum Entstehen dieser Arbeit beigetragen haben, meinen Dank aussprechen. Einige von ihnen will ich aber noch einmal explizit erwähnen.

An erster Stelle bedanke ich mich herzlich bei **Prof. Dr. Michael Farle** für die interessante Themenstellung, die Unterstützung und die vielen hilfreichen Anregungen.

Dr. Andreas Ney möchte ich von Herzen dafür danken, dass ich so viel von ihm lernen durfte. Sein Enthusiasmus bei der Erörterung zahlreicher theoretischer und experimenteller Fragestellungen in der Physik, aber auch weit darüber hinaus, haben mich sehr begeistert. Danken möchte ich ihm außerdem für die zahlreichen Hilfestellungen von der Einweisung am SQUID bishin zur interaktiven Tourenplanung für Stanford und Umgebung.

Danken möchte ich auch der gesamten Maglomat-Truppe, dass sich jeder geduldig die Zeit genommen hat, um sein Wissen mit mir zu teilen und für die Hilfe durch das Bedienen der Präparationskammer. Außerdem danke ich **Dr. Verena Ney** für ihre vielfache Unterstützung, nicht nur durch die unendlich vielen kleinen Striche am Rand dieser Arbeit, **Tom Kammermeier** dafür, dass ich von seiner Erfahrung profitieren durfte, nicht nur beim Füllen von Helium, sondern beispielsweise auch bei der Benutzung des Außenschlüssels und **Dr. Shuangli Ye** für ihr freundliches Wesen und ihre Geduld.

Ganz besonders danken möchte ich auch **Nina Friedenberger**, mit der ich im letzten Jahr durch die gemeinsame Bearbeitung des Themas so vieles geteilt habe, von der anfänglichen Verzweiflung über die 50 verschiedenen Spiegel- und Motorbezeichnungen bis zu den platten Füßen in Big Basin. Ihr habe ich zu verdanken, dass ich viele schöne Erinnerungen an Kalifornien mitnehmen konnte.

Christoph Hassel möchte ich danken für die lithographische Herstellung der Goldmarker der Nanopartikelproben für XPEEM und die Unterstützung im Reinraum, wo er neben **Oliver Posth**, **Anja Banholzer** und **Christian Wirtz** bei der Bedienung des SEM behilflich war. **Christian Wirtz** möchte ich darüber hinaus für das Korrekturlesen dieser Arbeit danken.

Anastasia Trounova und **Florian Römer** danke ich für die Hilfe bei der Plasmapehandlung der Nanopartikel.

Allen Mitgliedern der Arbeitsgruppe, auch wenn sie bisher nicht namentlich er-

wähnt sind, danke ich für die angenehme Arbeitsatmosphäre und eine gute Portion Humor.

Ich danke den Wissenschaftlern **Dr. Fabrice Wilhelm**, **Dr. Andrei Rogalev**, **Dr. Florian Kronast** und **Dr. Andreas Scherz**, mit denen ich an den verschiedenen Beamlines zusammengearbeitet habe, für die zahlreichen Hilfestellungen bei den Experimenten.

Prof. Dr. Joachim Stöhr, **Prof. em. Dr. Hans C. Siegmann** und den Mitgliedern ihrer Arbeitsgruppe danke ich für das freundliche Willkommenheißeln und für viele schöne Lunch-Diskussionen.

Großer Dank gebührt **Michael Ostermann**, der in mir die Begeisterung für die Physik geweckt und somit die Grundvoraussetzung für die Entstehung dieser Arbeit geschaffen hat.

Mein ganz besonderer Dank geht an **meine Eltern**, auf deren Unterstützung ich mich immer verlassen konnte.

Erklärung

Hiermit versichere ich, die vorliegende Arbeit selbstständig und unter ausschließlicher Verwendung der angegebenen Literatur und Hilfsmittel erstellt zu haben.

Die Arbeit wurde bisher in gleicher oder ähnlicher Form keiner anderen Prüfungsbehörde vorgelegt und auch nicht veröffentlicht.

Duisburg, November 12, 2008

Katharina J. Ollefs